3-1-2018

Computational Investigation Using Bleed as a Method of Shock Stabilization

Dayle L. Chang

Computational Investigation Using Bleed as a Method of Shock Stabilization

THESIS

Dayle L. Chang, First Lieutenant, USAF

AFIT-ENY-MS-18-M-247

DEPARTMENT OF THE AIR FORCE
AIR UNIVERSITY

AIR FORCE INSTITUTE OF TECHNOLOGY

Wright-Patterson Air Force Base, Ohio

AFIT-ENY-MS-18-M-247

COMPUTATIONAL INVESTIGATION USING BLEED AS A METHOD OF SHOCK STABILIZATION

THESIS

Presented to the Faculty

Department of Aeronautics and Astronautics

Graduate School of Engineering and Management

Air Force Institute of Technology

Air University

Air Education and Training Command

in Partial Fulfillment of the Requirements for the

Degree of Master of Science in Aerospace Engineering

Dayle L. Chang, B.S. Aerospace Engineering

First Lieutenant, USAF

28 March 2018

AFIT-ENY-MS-18-M-247

COMPUTATIONAL INVESTIGATION USING BLEED AS A METHOD OF SHOCK STABILIZATION

THESIS

Dayle L. Chang, B.S. Aerospace Engineering
First Lieutenant, USAF

Committee Membership:

Major Darrell S. Crowe, PhD
Chair

Dr. Scott E. Sherer
Member

Lieutenant Colonel Jacob A. Freeman, PhD
Member

Abstract

The interaction between shocks and the boundary layer in supersonic flow present difficulties in many applications such as inlet, aircraft, missile, and wind tunnel designs. These shock-wave/boundary layer interactions (SWBLI) frequently produce undesirable dynamic loads and separated unsteady flows, adversely impacting the performance and structural integrity of supersonic vehicles. Computational fluid dynamics (CFD) is a successful tool in experimental planning and shows promise as a critical tool in understanding SWBLI. The goal of this research is to demonstrate the effect of bleed holes on shock stability using the OVERFLOW CFD solver to inform the planning of an Air Force Research Laboratory (AFRL) SWBLI wind tunnel experiment. First, a two-dimensional, flat plate, single-hole configuration was developed. Massflow discrepancies of 14.8% were initially observed but reduced to 0% by analyzing the internal flow interaction with the boundary condition. Shock unsteadiness is then characterized using a canonical forward-facing step over a flat plate, which showed peaks at 5.8, 12.1, 31.2, 44.5, and 54.9 hertz. Though the final step of simulating bleed on the baseline forward-facing step was not achieved, promising time and frequency domain analysis techniques were demonstrated.

Acknowledgements

I cannot express enough gratitude for my research advisor and mentor, Major Darrell Crowe, who has helped see this project through to the end with encouragement, guidance, and freedom in the research. I also thank Dr. Scott Sherer, thesis committee member and technical advisor, for his help getting me started with this project and Lieutenant Colonel Jacob Freeman for the learning opportunity he has provided as the third committee member. This work would not have been possible without the sponsorship of Dr. Mike Stanek. I thank Dan Galbraith and David Weston for their time and technical expertise answering my endless OVERFLOW questions. I thank my supervisors over the years: Charlie Tyler, Major Mark Gabbard, Major Christopher Terpening, and Larry Leny. They have given me tremendous support and flexibility during the pursuit of this research. I extend special thanks to Kirk Lawson, Jerry Trummer, and Matt Grismer for their faithful Mac and Linux administrative help. I am grateful to both ASPRQ and the High Performance Computing Center for their endless computing hours, without which this research could not have been possible. Nobody has been more important to me during this research than my wife, to whom this is dedicated.

Dayle L. Chang

Table of Contents

Page

Page

List of Figures

List of Tables

List of Symbols

Symbol		Page
v	y-component of velocity	14
w	z-component of velocity	14
Pr	Prandtl number	15
$\vec{Q}$	vector of conserved variables	16
$\vec{F}_c$	convective flux vector	16
$\vec{F}_d$	diffusive flux vector	16
μ_t	eddy viscosity	26
k_t	turbulent thermal conductivity	26
$\tilde{\nu}$	turbulent kinematic viscosity parameter (S-A)	27
ν_t	kinematic eddy viscosity	27
ν	laminar kinematic viscosity	27
Q	flow coefficient	33
$\dot{m}$	mass flow rate	33
Φ	bleed porosity	33
A	area	33
p_t	total pressure	34
T_t	total temperature	34

List of Abbreviations

Abbreviation		Page
SWBLI	shock-wave/boundary layer interaction	1
NASA	National Aeronautics and Space Administration	4
SBIR	Small Business Innovation Research	4
NHFRP	National Hypersonics Foundational Research Plan	4
AFOSR	Air Force Office of Scientific Research	4
RTO/AVT	Research and Technology Office, Air Vehicle Technology	5
NATO	North Atlantic Treaty Organization	5
AFRL	Air Force Research Laboratory	5
TGF	Trisonic Gasdynamics Facility	5
CFD	computational fluid dynamics	5
PDE	partial differential equations	19
DNS	direct numerical simulation	25
RANS	Reynolds-averaged Navier-Stokes	25
S-A	Spalart-Allmaras	27
LES	large eddy simulation	31
DES	detached eddy simulation	32
DDES	delayed detached eddy simulation	32
CGT	Chimera Grid Tools	36
TCL	Tool Command Language	36
GUI	graphical user interface	36
FOMOCO	Force and Moment Computation	36
OVERFLOW	Overset grid FLOW solver	37

Abbreviation		Page
HLLC	Harten-Lax-van Leer-Contact	59
SSOR	Implicit Symmetric Successive Over-Relaxation	59

COMPUTATIONAL INVESTIGATION USING BLEED AS A METHOD OF SHOCK STABILIZATION

I. Introduction

1.1 Motivation

Shock waves are a natural phenomenon that arise in supersonic operation. When the shock interacts with the boundary layer, the situation becomes complex and is an important design consideration for applications in transonic and supersonic flows. This interaction occurs so pervasively that it has been termed the shock-wave/boundary layer interaction (SWBLI). Successful utilization of aircraft, missiles, inlets, or wind tunnel designs in supersonic flow are contingent on the favorable behavior of the SWBLI in both internal and external flows [15]. Three key issues that arise due to SWBLI are identified by Holden: peak heating, dynamic loads, and effects of separated unsteady flows [16]. These three issues and their effects on practical applications are discussed in greater depth below and together represent the motivation for this research. The chapter concludes by summarizing the objectives of this research.

Peak Heating.

The severe effects of peak heating are well documented in SWBLI, particularly in hypersonic flows. Peak heating rates vary between 10 to 100 times the incoming boundary-layer flow and many times the equivalent stagnation point value [13]. Knight and Degrez note that "heat transfer distribution predictions are generally

poor, except for weak interactions, and significant differences are evident between turbulence models. . . of up to 100% between experiment and numerical results" [17]. These high temperatures cause localized stresses which affect practical designs factors such as geometry, fatigue, material selection, and thermal protection [13].

Dynamic Loads.

In many aeronautical applications, parameters of critical importance are imposed by unsteady conditions that can occur during flight, rather than steady conditions. Although these events are rare or do not contribute much to the local average energy, they can correspond to high local stress, which can affect the entire behavior of the system. In supersonic flows, an important case occurs when unsteadiness involves shock waves producing locally large pressure gradients. The pressure fluctuations impose strong aerodynamic loads which propogate downstream of the shock wave. This occurs in shock-induced separation, where low-frequency unsteadiness is produced [23].

The impact of unsteady aerodynamic loading is seen in the controls response system of aircraft and missile bodies. High-speed, anti-armor, kinetic energy penetrators (Mach 4-8 at sea level) are configurations of interest to the U.S. Army that pose many simulation and experimental challenges due to the SWBLI. Following discharge from the gun, lateral thrusters or control surfaces may be used to guide and control such projectiles. Accurate characterization of the three-dimensional, unsteady, laminar, transitional, and turbulent interactions that sweep rapidly across the body is important in ensuring proper aerodynamic control of aerodynamic bodies and requires accurate modeling of SWBLI [13].

Another example of the negative impact of unsteady aerodynamic loading is plume-induced boundary-layer separation in missile design. The boundary layer sep-

arates off the missile afterbody rather than at the base of the missile, resulting in a strong and adverse pressure gradient generated by the interaction of the expanding plume and surrounding freestream. The premature boundary layer separation generates large, unsteady, and asymmetric loads on the missile body for which the control surfaces and response system must have adequate control authority and response timing to overcome [13]. In the worst case, inadequate control authority or poor control respose may cause the control surfaces themselves to experience premature boundary layer separation, resulting in a partial to total loss of control effectiveness. An understanding of the fundamental flow physics allows for missile designs to successfully demonstrate control authority during flight and achieve maximum performance. Shaw et al. notes this plume-induced separation feature is not unlike the SWBLI behavior on a compression ramp and shares many common features, which can be used to characterize the separation for missile applications [28].

Unsteady Flow.

Mixed compression inlets are designed to produce a shock train structure and terminal shock that allows for the highest total pressure recovery. However, these shocks are sensitive to flow disturbances and flow unsteadiness due to their interaction with the boundary layer. If the effects of unsteady flow are not mitigated, changes to the flow structure can displace the shock wave into a less efficient configuration. If the disturbances are large enough, the terminal shock may move upstream and ultimately out of the inlet, resulting in unstart that produces large transient forces on the airframe and cause engine surge [13].

Bleed holes are used as a method of active flow control to mitigate flow unsteadiness inside the inlet. By adjusting the mass-flow rate reaching the diffuser in response to perturbations in the engine operation or inlet flow, the shock train is stabilized.

The disadvantage of such a method is that energy and thrust is reduced while weight is increased. Factors such as bleed hole location, hole geometry, suction massflow rate, and many others make this an area of ongoing research [13].

Current Views.

SWBLI is recognized as a long-standing research area in the aerospace community, garnering wide attention both nationally and internationally [15]. A 1996 National Aeronautics and Space Administration (NASA) research announcement stated that "improved air-breathing engines will require a clearer understanding of the basic flow physics of propulsion system components." The design of higher performance inlets and nozzles that are "quieter, shorter, lighter" requires "benchmark quality data for flowfields including shocks, boundary layers, boundary layer control, separation, heat transfer, surface cooling and jet mixing." These areas all involve SWBLI in one form or another [13].

The NASA Small Business Innovation Research (SBIR) solicitation in 2015 emphasized the need for basic research to be relevant for practical applications: "One of the greatest issues that NASA faces in transitioning advanced technologies into future aeronautics systems is the gap . . . between the maturity level of technologies developed through fundamental research and the maturity required for technologies to be infused into future air vehicles and operational systems" [21]. Fundamental research faces "inadequacies in our understanding of boundary layer turbulence [that] increase reliance upon a more qualitative, physics-guided approach to discovery" [20].

The National Hypersonics Foundational Research Plan (NHFRP) was developed by the Air Force Office of Scientific Research (AFOSR), NASA, and Sandia National Laboratory. This plan provides a framework of the main areas in hypersonics research of which SWBLI is a key component. The Research and Technology Office, Air Vehicle

Technology (RTO/AVT) has been an integral part of that development under North Atlantic Treaty Organization (NATO) [27].

Flow control for SWBLI remains a key issue for future technology vehicles but is regarded as a complicated and vexing problem. To make the proper trade-offs in design, a deep, physical understanding of the mechanisms of these interactions must be understood with both experimental and computational tools that are both robust and accurate [13].

1.2 Research Objectives

A supersonic wind tunnel model designed for research by the Air Force Research Laboratory (AFRL) (shown in Figure 1) will be used in an upcoming SWBLI experiment. The experiment will be conducted in the Trisonic Gasdynamics Facility (TGF) at Wright-Patterson Air Force Base and will explore various methods of understanding and mitigating SWBLI. The first entry of the AFRL experiment will incorporate bleed holes towards stabilization of an unsteady shock as a first step towards the goal of understanding and mitigating SWBLI.

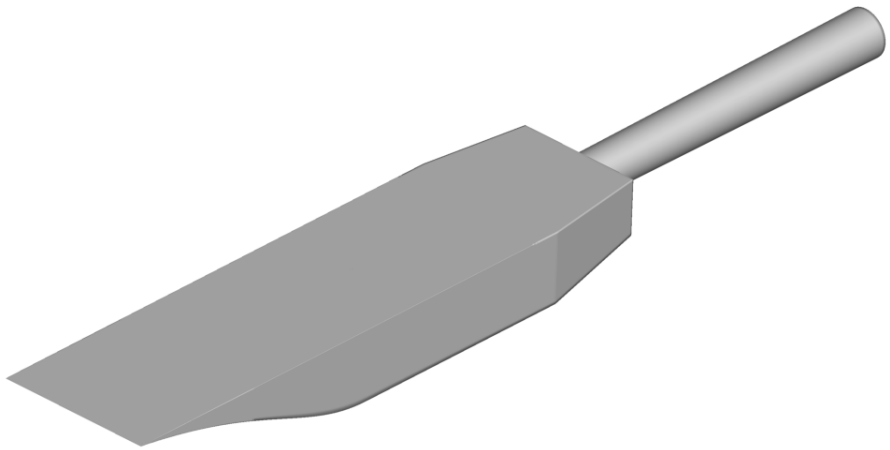

Figure 1. Supersonic tunnel model on a support sting.

The advancement of computational fluid dynamics (CFD) has allowed CFD to be

a successful design tool in experimental planning and shows promise as a critical tool in understanding SWBLI [13, 42]. The current computational research will inform the planning and design of the AFRL experiment to save on tunnel run-time and to bring insight into the flow physics of the experiment. The goal of this research is to use CFD to demonstrate the effect of bleed holes on shock unsteadiness. Since the wind tunnel model currently does not incorporate a shock near the bleed hole in the experiment, the computational effort will use a canonical forward-facing step to generate the unsteady shock and this effort will determine if this configuration is a successful model for mitigating shock unsteadiness. The objectives of this research are listed below:

- Develop grid independent computational domains
- Compare against previous experimental and computational work
- Explore validity of using a two-dimensional bleed model to remove plenum effects
- Characterize shock unsteadiness
- Demonstration of improved shock stability

To accomplish these objectives, this research will focus on characterizing the flow physics of a single bleed hole on a flat plate to ensure the flow is accurately modeled. Computational simulations of the bleed hole will be verified against other computational studies in addition to empirical models based on experimental data. A two-dimensional simulation was used for simplicity so the value of a two-dimensional assumption in modeling flow through a bleed hole, or slot in two dimensions, was examined. To assess an improvement in shock stability, a baseline shock was first characterized using a forward-facing step on a flat plate. Then, the change in shock

strength and unsteadiness could be quantified after incorporating a bleed hole ahead of the forward-facing step. More than demonstrating the quantitative improvements in shock stabilization, this research aims to yield insight and a computational framework into how high-fidelity CFD can assist in identifying areas of unsteadiness due to SWBLI as well as recommendations on how flow control is used to mitigate negative effects.

Chapter I introduces the subject, motivation, and objectives of this research. Chapter II presents further background information on SWBLI and flow control to include relevant research areas. In addition, it will provide fundamental theory for expected flow phenomena. Chapter III explains the computational methodologies used in the computational setup including grid generation, flow solver parameters, turbulence modeling, and the overall experimental approach. Chapter IV presents the results of the grid topology screening, time step and grid refinement study and aerodynamic characterization of the shock unsteadiness at supersonic conditions. The results are analyzed and compared to experimental data and empirical models. A summary of the research and recommendations for future work are given in Chapter V.

II. Background and Theory

2.1 Derivation of the Navier-Stokes Equations

The Navier-Stokes equations describe the motion of viscous fluids and are useful because they describe the physics of scientific and engineering interests. For example, they are used to model the weather, ocean currents, water flow in a pipe, and air flow around a wing. Before deriving the Navier-Stokes equations, assumptions about the flow are made and physical principles are discussed to arrive at the governing equations of fluid dynamics in the following sections.

The first assumption is that the density of the fluid is assumed to be high enough such that the flow is approximated as a continuum. This implies that an infinitesimally small, or differential, element of the fluid still contains a sufficient number of particles for which the mean velocity and mean kinetic energy can be specified. This assumption enables important quantities such as velocity, pressure, temperature, and density to be defined at each point in the fluid. In mathematical terms, the continuum assumption states the mean free path of molecules λ is proportionally much smaller than the characteristic length of interest L as shown below

$$k_n = \frac{\lambda}{L} \ll 1 \tag{1}$$

where k_n is the Knudsen number. The derivation of the Navier-Stokes equations is based on the fact that the dynamic behavior of the fluid is determined by the following conservation laws:

- Conservation of Mass
- Conservation of Momentum
- Conservation of Energy

The conservation of these flow quantities means that its total variation inside an arbitrary volume can be expressed as the net effect of the flux, or the rate a flow quantity crosses a boundary surface, any internal forces and sources, and external forces acting on the volume. The flux is decomposed into two parts: one due to convective transport and the other due to molecular motion present in the fluid at rest, or diffusion [5]. In the following discussion, the finite control volume is defined and a mathematical description of its physical properties for fluid flow is detailed.

Conservation Law within a Control Volume.

A control volume Ω is defined as an arbitrary and finite region of fluid flow fixed in space and bounded by the closed surface $d\Omega$. The surface element dS represents a small and finite portion of the surface $d\Omega$ and $\vec{n}$ is the associated outward pointing unit normal vector. The net change of a fluid property within the control volume is determined by performing a balance between the net flow in and out of the control volume, such as the force or total energy exchange. This is expressed in a mathematical sense: the change of a given property in time is described as the sum of convective fluxes, diffusive fluxes, volume sources, and surface sources in and through a control volume. This conservation law is shown for the general property U in integral form as shown below:

$$\frac{\partial}{\partial t}\int_{\Omega} U\, d\Omega = \oint_{\partial\Omega} \left[\kappa\rho(\boldsymbol{\nabla} U^* \cdot \vec{n}) - U(\vec{v}\cdot\vec{n})\right] dS + \int_{\Omega} S_v\, d\Omega + \oint_{\partial\Omega} \left(\vec{S}_s \cdot \vec{n}\right) dS \qquad (2)$$

where Ω is the control volume, $d\Omega$ is the differential control volume, κ is the thermal diffusivity coefficient, ρ is density, $\vec{v}$ is the velocity vector, $\vec{n}$ is the outward-facing unit normal vector, S_v is the volume source, $\vec{S}_s$ is the surface source vector, and dS is the differential surface element. If U is not a scalar but instead a vector $\vec{U}$, the

conservation law still holds and is further generalized in vector form as

$$\frac{\partial}{\partial t}\int_{\Omega}\vec{U}\,d\Omega = \oint_{\partial\Omega}\left[\left(\overline{\overline{F}}_d - \overline{\overline{F}}_c\right)\cdot\vec{n}\right]dS + \int_{\Omega}\vec{S}_v\,d\Omega + \oint_{d\Omega}\left(\overline{\overline{S}}_s\cdot\vec{n}\right)dS \tag{3}$$

where $\overline{\overline{F}}_d$ is the diffusive flux tensor, $\overline{\overline{F}}_c$ is the convective flux tensor, $\vec{S}_v$ is the volume source vector, and $\overline{\overline{S}}_s$ is the surface source tensor. This formulation of conservation is the basis of the derivation for the conservation laws of mass, momentum, and energy in the continuing discussion.

Conservation of Mass.

The law of conservation of mass states that mass can neither be created nor destroyed. Therefore, the time rate of change of mass within a given control volume is dependent only on the net mass coming in and out of the control volume due to convection. Simply put, convection is the only mechanism by which mass can change within a control volume. The diffusive flux, surface source, and volume source terms all go to zero as a result. This concept is expressed mathematically below:

$$\frac{\partial}{\partial t}\int_{\Omega}\rho\,d\Omega + \oint_{\partial\Omega}\rho(\vec{v}\cdot\vec{n})\,dS = 0 \tag{4}$$

This yields the conservative, integral form of the continuity equation.

Conservation of Momentum.

The law of conservation of momentum states that the time rate of change of momentum is equal to the net force acting on a control volume. The momentum of an infinitesimally small portion of the control volume Ω is $\rho\vec{v}\,d\Omega$, where $\vec{v} = [u, v, w]^T$ in a three component Cartesian coordinate system. The variation in time of momentum

within the control volume is described as

$$\frac{\partial}{\partial t}\int_{\Omega}\rho\vec{v}\,d\Omega \tag{5}$$

The convective flux term is the transfer of momentum across the boundary of the control volume

$$-\oint_{\partial\Omega}\rho\vec{v}(\vec{v}\cdot\vec{n})\,dS \tag{6}$$

The diffusive flux term is zero since there is no diffusion of momentum for a fluid at rest. The volume sources for momentum conservation are called body forces and described as forces which act directly on the mass of the volume such as gravitational, buoyancy, Coriolis, centrifugal, or electromagnetic forces. They are ignored in this derivation by setting the sources equal to zero.

The surface sources for momentum conservation act directly on the surface of the control volume and consist of two components: the pressure distribution imposed by the fluid surrounding the volume, $-p\overline{\overline{I}}$, and the shear and normal stresses resulting from the friction between the fluid and the surface of the volume, $\overline{\overline{\tau}}$, as shown below

$$\overline{\overline{S}}_s = -p\overline{\overline{I}} + \overline{\overline{\tau}} \tag{7}$$

where $\overline{\overline{I}}$ is the unit tensor, p is pressure, and $\overline{\overline{\tau}}$ is the viscous stress tensor. Each of the terms are summed up in the following mathematical expression:

$$\frac{\partial}{\partial t}\int_{\Omega}\rho\vec{v}\,d\Omega + \oint_{\partial\Omega}\rho\vec{v}(\vec{v}\cdot\vec{n})\,dS + \oint_{\partial\Omega}p\vec{n}\,dS - \oint_{\partial\Omega}\left(\overline{\overline{\tau}}\cdot\vec{n}\right)dS = 0 \tag{8}$$

This yields the conservative, integral form of the momentum equation.

Conservation of Energy.

The law of conservation of energy states that the internal energy of the control volume is equal to the rate of work performed on the volume and the net heat supplied to the volume. The conserved quantity is the total energy per unit volume ρE and its variation in time within the volume Ω is expressed as

$$\frac{\partial}{\partial t} \int_{\Omega} \rho E \, d\Omega \tag{9}$$

Just like the previous mass and momentum equations, the convective flux term is specified as

$$- \oint_{\partial\Omega} \rho E (\vec{v} \cdot \vec{n}) \, dS \tag{10}$$

In contrast to the previous mass and momentum equations, the diffusive flux term is present in the energy equation and describes the diffusion of heat due to molecular thermal conduction. The diffusive flux term $\vec{F}_d$ is written in the form of Fourier's law of heat conduction, which characterizes heat diffusion as the heat transfer due to temperature gradients

$$\vec{F}_d = -k \boldsymbol{\nabla} T \tag{11}$$

where k is the thermal conductivity coefficient and T is the absolute static temperature.

The volume source for the energy equation is the volumetric heating due to the absorption or emission of radiation, or due to chemical reactions as well as work done by the body forces. These volume sources are ignored and not considered for this derivation.

The surface source term is the time rate of work done by pressure and the shear

and normal stresses on the fluid element

$$\vec{S}_s = -p\vec{v} + \overline{\overline{\tau}} \cdot \vec{v} \tag{12}$$

where $\overline{\overline{\tau}}$ is the stress tensor

$$\overline{\overline{\tau}} = \begin{bmatrix} \tau_{xx} & \tau_{xy} & \tau_{xz} \\ \tau_{yx} & \tau_{yy} & \tau_{yz} \\ \tau_{zx} & \tau_{zy} & \tau_{zz} \end{bmatrix} \tag{13}$$

The off-diagonal elements of $\overline{\overline{\tau}}$ represent the viscous shear stresses and defined as

$$\begin{aligned} \tau_{xy} = \tau_{yx} &= \mu\left(\frac{\partial u}{\partial y} + \frac{\partial v}{\partial x}\right) \\ \tau_{xz} = \tau_{zx} &= \mu\left(\frac{\partial u}{\partial z} + \frac{\partial w}{\partial x}\right) \\ \tau_{yz} = \tau_{zy} &= \mu\left(\frac{\partial v}{\partial z} + \frac{\partial w}{\partial y}\right) \end{aligned} \tag{14}$$

The diagonal elements represent the viscous normal stresses and defined as

$$\begin{aligned} \tau_{xx} &= \lambda\left(\frac{\partial u}{\partial x} + \frac{\partial v}{\partial y} + \frac{\partial w}{\partial z}\right) + 2\mu\frac{\partial u}{\partial x} \\ \tau_{yy} &= \lambda\left(\frac{\partial u}{\partial x} + \frac{\partial v}{\partial y} + \frac{\partial w}{\partial z}\right) + 2\mu\frac{\partial v}{\partial y} \\ \tau_{zz} &= \lambda\left(\frac{\partial u}{\partial x} + \frac{\partial v}{\partial y} + \frac{\partial w}{\partial z}\right) + 2\mu\frac{\partial w}{\partial z} \end{aligned} \tag{15}$$

where μ represents the dynamic viscosity and λ represents the second viscosity. Stoke's hypothesis eliminates λ by relating the second viscosity and the dynamic viscosity as a bulk viscosity, which represents the property that is responsible for energy dissipation in a fluid of uniform temperature during a change in volume at a finite rate as shown.

$$\lambda + \frac{2}{3}\mu = 0 \tag{16}$$

The diagonal elements are then simplified using Stoke's hypothesis (Equation 16) for the viscous normal stresses (Equation 15) as shown below

$$\begin{aligned}
\tau_{xx} &= 2\mu\left[\frac{\partial u}{\partial x} - \frac{1}{3}\left(\frac{\partial u}{\partial x} + \frac{\partial v}{\partial y} + \frac{\partial w}{\partial z}\right)\right] \\
\tau_{yy} &= 2\mu\left[\frac{\partial u}{\partial x} - \frac{1}{3}\left(\frac{\partial u}{\partial x} + \frac{\partial v}{\partial y} + \frac{\partial w}{\partial z}\right)\right] \\
\tau_{zz} &= 2\mu\left[\frac{\partial u}{\partial x} - \frac{1}{3}\left(\frac{\partial u}{\partial x} + \frac{\partial v}{\partial y} + \frac{\partial w}{\partial z}\right)\right]
\end{aligned} \tag{17}$$

The terms are summed in the following mathematical expression:

$$\begin{aligned}
\frac{\partial}{\partial t}\int_{\Omega} \rho E \, d\Omega + \oint_{\partial\Omega} \rho E(\vec{v}\cdot\vec{n})\, dS = \oint_{\partial\Omega} k(\boldsymbol{\nabla} T\cdot\vec{n})\, dS - \oint_{\partial\Omega} p(\vec{v}\cdot\vec{n})\, dS \\
+ \oint_{\partial\Omega} \left(\overline{\overline{\tau}}\cdot\vec{v}\right)\cdot\vec{n}\, dS
\end{aligned} \tag{18}$$

This yields the conservative, integral form of the energy equation.

Closing the Equations.

The mass, momentum, and energy equations are collectively referred to as the Navier-Stokes equations, representing a system of five equations in three dimensions for the five conserved variables ρ, ρu, ρv, ρw, and ρE. However, the governing equations contain nine unknown flow field variables: ρ, u, v, w, E, p, T, μ, and k. Therefore, four additional equations are needed to close the equations, which is accomplished by formulating thermodynamic relations between the two unknown state variables for pressure, p, and temperature, T. For an ideal perfect gas, the equation of state assumes the form

$$p = \rho R T \tag{19}$$

where R denotes the specific molecular gas constant. This equation can be written as a function of the conserved variables by using the definition of enthalpy

$$H = h + \frac{|\vec{v}|^2}{2} = E + \frac{p}{\rho} \tag{20}$$

which relates the total enthalpy to the total energy. Using the definitions

$$R = c_p - c_v, \qquad \gamma = \frac{c_p}{c_v}, \qquad h = c_p T$$

the enthalpy equation (Equation 20) is substituted into the equation of state (Equation 19) to obtain for the pressure as a function of the conserved variables

$$p = (\gamma - 1)\rho\left[E - \frac{u^2 + v^2 + w^2}{2}\right] \tag{21}$$

Calculating temperature becomes trivial with the aid of Equation 19. Dynamic viscosity μ is strongly dependent on temperature but only weakly dependent on pressure. Sutherland's formula describes this relationship for air (in SI units)

$$\mu = \frac{1.45T^{\frac{3}{2}}}{T + 110} \cdot 10^{-6} \tag{22}$$

where the temperature, T, is in degrees Kelvin (K). The Prandtl number (Pr) is a dimensionless number defined as the ratio of momentum diffusivity to thermal diffusivity

$$Pr = \frac{c_p \mu}{k} \tag{23}$$

The Prandtl number is assumed constant in the flow for air with a value of $P_r = 0.72$. Therefore, the thermal conductivity, k, is determined from temperature. [4, 5, 37–39].

Integral Form of the Navier-Stokes Equations.

For the complete system of the Navier-Stokes equations, Equations 4, 8 and 18 are combined using the general conservation law (Equation 3) into the following vectorized form:

$$\frac{\partial}{\partial t}\int_{\Omega} \vec{Q}\, d\Omega + \oint_{d\Omega} (\vec{F}_c - \vec{F}_v)\, dS = 0 \tag{24}$$

where $\vec{Q}$ is the vector of conserved variables in three dimensions, $\vec{F}_c$ represents the convective fluxes, and $\vec{F}_d$ represents the diffusive fluxes. Note that Equation 24 does not include any source terms. These three vectors for the five total equations are defined as follows

$$\vec{Q} = \begin{bmatrix} \rho \\ \rho u \\ \rho v \\ \rho w \\ \rho E \end{bmatrix} \tag{25}$$

$$\vec{F}_c = \begin{bmatrix} \rho V \\ \rho u V + n_x p \\ \rho v V + n_y p \\ \rho w V + n_z p \\ \rho H V \end{bmatrix} \tag{26}$$

$$\vec{F}_v = \begin{bmatrix} 0 \\ n_x\tau_{xx} + n_y\tau_{xy} + n_z\tau_{xz} \\ n_x\tau_{yx} + n_y\tau_{yy} + n_z\tau_{yz} \\ n_x\tau_{zx} + n_y\tau_{zy} + n_z\tau_{zz} \\ n_x\Theta_x + n_y\Theta_y + n_z\Theta_z \end{bmatrix} \tag{27}$$

where V is the contravariant velocity

$$V \equiv \vec{v} \cdot \vec{n} = n_x u + n_y v + n_z w \tag{28}$$

and where

$$\begin{aligned} \Theta_x &= u\tau_{xx} + v\tau_{xy} + w\tau_{xz} + k\frac{\partial T}{\partial x} \\ \Theta_y &= u\tau_{yx} + v\tau_{yy} + w\tau_{yz} + k\frac{\partial T}{\partial y} \\ \Theta_z &= u\tau_{zx} + v\tau_{zy} + w\tau_{zz} + k\frac{\partial T}{\partial z} \end{aligned} \tag{29}$$

Equations 24 -29 ultimately describe the exchange of mass, momentum, and energy through the boundary $d\Omega$ of a fixed control volume Ω in what is known as the integral form of the Navier-Stokes equations.

Differential Form of the Navier-Stokes Equations.

Though not always the case, the integral form of the Navier-Stokes equations is better understood in the context of the finite volume method. However, the code used in this research (OVERFLOW) uses the finite-difference method and so the differential form of the Navier-Stokes equations is presented for completeness.

Recall the integral form of the Navier-Stokes equations were presented in the discussion from the starting assumption that the control volume was fixed in space, an Eulerian frame of reference. An alternative approach examines the differential element moving with the fluid flow, a Lagrangian frame of reference, rather than a control volume fixed in space. The two frames of reference are related through the Reynolds transport theorem which relates the rate of change of a system property within a fixed region (control volume) to the time derivative of a system property (differential element). Applying the theorem to the integral form of the governing

equations (Equation 24) leads to the differential form as shown below

$$\frac{\partial}{\partial t}\int\limits_{\Omega}\vec{Q}\,d\Omega+\int\limits_{\Omega}\boldsymbol{\nabla}\cdot\left(\vec{F}_c-\vec{F}_v\right)d\Omega=0 \tag{30}$$

The integral drops out for an arbitrary control volume Ω and the equation is written in the differential form as

$$\frac{\partial\vec{Q}}{\partial t}+\boldsymbol{\nabla}\cdot\left(\overline{\overline{F}}_c-\overline{\overline{F}}_v\right)=0 \tag{31}$$

It is typical to combine the convective and viscous fluxes and expand the gradient operator $\boldsymbol{\nabla}$ to arrive at the generalized form

$$\frac{\partial\vec{Q}}{\partial t}+\frac{\partial\vec{E}}{\partial x}+\frac{\partial\vec{F}}{\partial y}+\frac{\partial\vec{G}}{\partial z}=0 \tag{32}$$

where $\vec{E}$, $\vec{F}$, and $\vec{G}$ represent the fluxes in the x-, y-, and z-directions, respectively, as shown below

$$\vec{Q}=\begin{bmatrix}\rho\\ \rho u\\ \rho v\\ \rho w\\ \rho E\end{bmatrix} \tag{33}$$

$$\vec{E}=\begin{bmatrix}\rho u\\ \rho u^2+p-\tau_{xx}\\ \rho uv-\tau_{xy}\\ \rho uw-\tau_{xz}\\ (\rho E+p)u-\Theta_x\end{bmatrix} \tag{34}$$

$$\vec{F} = \begin{bmatrix} \rho v \\ \rho uv - \tau_{xy} \\ \rho v^2 + p - \tau_{yy} \\ \rho vw - \tau_{yz} \\ (\rho E + p)v - \Theta_y \end{bmatrix} \tag{35}$$

$$\vec{G} = \begin{bmatrix} \rho w \\ \rho uw - \tau_{xz} \\ \rho vw - \tau_{yz} \\ \rho w^2 + p - \tau_{zz} \\ (\rho E + p)w - \Theta_z \end{bmatrix} \tag{36}$$

Equations 29 and 32 -36 describe the change in mass, momentum, and energy at an infinitesimally small element of the flow in what is known as the differential form of the Navier-Stokes equations.

2.2 Boundary Conditions

The Navier-Stokes equations are a set of partial differential equations (PDE) for which an analytical solution does not currently exist, but can be solved approximately and iteratively using computers. In computing solutions to PDEs, the appropriate application of boundary conditions is a key ingredient in arriving at a unique and practical solution. The two most common boundary conditions as it pertains to the Navier-Stokes equations are the Dirichlet boundary condition, where the value of the function is specified on the boundary, and the Neumann boundary condition, where the normal derivative of the function is specified on the boundary.

The Dirichlet boundary condition is applied in the supersonic inflow, supersonic outflow, periodic, and specified pressure conditions where the values at the boundary

are prescribed. Both the Dirichlet and Neumann boundary conditions are applied in the no-slip wall condition. The boundary conditions are enforced for higher-order methods by dummy nodes, artificial nodes surrounding the computational domain whose field values are set to expand the stencil. A simple overview of the no-slip wall, supersonic inflow, supersonic outflow, periodic, and specified pressure boundary conditions are presented in the following discussion.

No-Slip Wall.

The interaction between molecules of a viscous fluid and a solid surface create a condition where the fluid velocity is zero relative to the boundary, hence the name "no-slip" wall. The assumption that there is no heat transfer through the wall is additionally employed to determine the other conserved variables at the boundary

$$\vec{Q}_b = \begin{bmatrix} \rho_i \\ 0 \\ 0 \\ 0 \\ (\rho E)_i \end{bmatrix} \tag{37}$$

where the subscript i denotes the value one node interior from the boundary and the subscript b denotes the value at the node on the boundary. For implementations of higher-order methods at the boundary, the dummy node is prescribed values such

that the fluxes, both convective and viscous, are zero through the boundary.

$$\vec{Q}_d = \begin{bmatrix} \rho_i \\ -(\rho u)_i \\ -(\rho v)_i \\ -(\rho w)_i \\ (\rho E)_i \end{bmatrix} \tag{38}$$

where the subscript d denotes the value at the dummy node, or one node exterior from the boundary.

Supersonic Inflow.

Consider a supersonic flow and the type of domain boundary that is present at the inflow. If one examines the direction of signal propagation for this condition, the characteristics carry information from the exterior of the domain toward the interior in all cases. This indicates that all the information at the inflow boundary for a supersonic flow must be specified using the freestream conditions so that information will always be carried toward the boundary from the exterior. Thus the conserved variables at the boundary are

$$\vec{Q}_b = \begin{bmatrix} \rho_\infty \\ (\rho u)_\infty \\ (\rho v)_\infty \\ (\rho w)_\infty \\ (\rho E)_\infty \end{bmatrix} \tag{39}$$

where the subscript ∞ denotes freestream values. The dummy nodes are likewise prescribed the same interior values so that freestream values are propagated into the

domain

$$\vec{Q}_g = \begin{bmatrix} \rho_\infty \\ (\rho u)_\infty \\ (\rho v)_\infty \\ (\rho w)_\infty \\ (\rho E)_\infty \end{bmatrix} \tag{40}$$

Supersonic Outflow.

The numerical implementation of the supersonic outflow boundary condition must prevent any outgoing disturbances from reflecting back into the flow field. At the outflow boundaries, the characteristics all carry the same sign for the supersonic case and the solution must be determined entirely from conditions based on the interior. Thus, the flow properties at the boundary are prescribed values one node interior from the boundary

$$\vec{Q}_b = \begin{bmatrix} \rho_i \\ (\rho u)_i \\ (\rho v)_i \\ (\rho w)_i \\ (\rho E)_i \end{bmatrix} \tag{41}$$

The dummy nodes are likewise prescribed the same interior values so that no information propagates into the domain

$$\vec{Q}_g = \begin{bmatrix} \rho_i \\ (\rho u)_i \\ (\rho v)_i \\ (\rho w)_i \\ (\rho E)_i \end{bmatrix} \tag{42}$$

Specified Pressure Outflow.

The specified pressure outflow boundary condition is useful to simulate discharge of flow into an ambient pressure such as a plenum, ambient air, or a vacuum. The implementation requires density and the three velocity components to be extrapolated from the interior of the physical domain to the boundary. Since the pressure is specified, the fifth conserved variable, energy, is determined from the equation of state (Equation 19) as shown below

$$\vec{Q}_b = \begin{bmatrix} \rho_i + (p_b - p_i)/c_0^2 \\ \rho_u[u_d + n_x(p_i - p_b)/(\rho_0 c_0)] \\ \rho_v[v_d + n_y(p_i - p_b)/(\rho_0 c_0)] \\ \rho_w[w_d + n_z(p_i - p_b)/(\rho_0 c_0)] \\ p_b/(\gamma - 1) + \rho(u^2 + v^2 + w^2)/2 \end{bmatrix} \tag{43}$$

where p_b is the specified pressure at the boundary. Field values for the dummy node is obtained by linear extrapolation from the states i and b.

Periodic.

There are certain practical applications where the flow field is periodic with respect to one or multiple coordinate directions. In such a case, it is sufficient to simulate the flow within one of the repeating regions. The correct interaction with the remaining physical domain is enforced with a periodic boundary condition. The boundary condition is typically applied to two identical planes that are not collocated

in space and is denoted below with the superscripts 1 and 2

$$\vec{Q}_b^1 = \begin{bmatrix} \rho_i^2 \\ (\rho u)_i^2 \\ (\rho v)_i^2 \\ (\rho w)_i^2 \\ (\rho E)_i^2 \end{bmatrix} \qquad \vec{Q}_b^2 = \begin{bmatrix} \rho_i^1 \\ (\rho u)_i^1 \\ (\rho v)_i^1 \\ (\rho w)_i^1 \\ (\rho E)_i^1 \end{bmatrix} \tag{44}$$

The dummy nodes follow the same principle and are prescribed values one node further into the domain, denoted by the subscript $i+1$ as shown

$$\vec{Q}_d^1 = \begin{bmatrix} \rho_{i+1}^2 \\ (\rho u)_{i+1}^2 \\ (\rho v)_{i+1}^2 \\ (\rho w)_{i+1}^2 \\ (\rho E)_{i+1}^2 \end{bmatrix} \qquad \vec{Q}_d^2 = \begin{bmatrix} \rho_{i+1}^1 \\ (\rho u)_{i+1}^1 \\ (\rho v)_{i+1}^1 \\ (\rho w)_{i+1}^1 \\ (\rho E)_{i+1}^1 \end{bmatrix} \tag{45}$$

2.3 Turbulence Modeling

The Navier-Stokes equations as described thus far hold only for laminar flow. However, it is known from simple observation of fluid flow that small disturbances in laminar flow can cause the flow to transition to turbulence. The onset of this chaotic and random state of motion found in turbulent flows depends on the ratio of inertial to viscous forces, or Reynolds number. At low Reynolds numbers, viscous forces dominate, the naturally occurring disturbances dissipate away, and the flow remains laminar. At high Reynolds numbers, the inertial forces are sufficiently large to amplify the disturbances and transition from laminar to turbulent flow occurs.

Fundamentally, turbulence is a continuum phenomenon since the smallest scales

of turbulence are very large compared to the molecular scales. This implies the Navier-Stokes equations are of deterministic nature since it contains all of the physics of turbulent fluid motion [5] but the direct simulation of turbulent flows presents a significant problem. Despite the performance of modern supercomputers, a direct numerical simulation (DNS) of turbulence by the time-dependent Navier-Stokes equations is applicable only to relatively simple flow problems at low Reynolds numbers in the order of 10^4–10^5. The simulation must resolve a wide range of scales from the largest, energy bearing eddies to the smallest, vorticity containing eddies that accomplish the continuous dissipation of mechanical energy into internal energy. An accurate turbulent simulation must capture the entire range of active scales - a range that increases rapidly as Reynolds number increases. Widespread utilization of DNS is prevented by the fact that the number of grid points needed for sufficient spatial resolution scales as Re^2 and the CPU-time as Re^3. Therefore, the effects of turbulence must be accounted for in an approximate matter and a large variety of turbulence models were developed for this purpose. The Reynolds-averaged Navier-Stokes (RANS) equations are outlined followed by a discussion of two turbulence models and a hybrid model of the two.

Reynolds-Averaged Navier-Stokes Equations.

In the late 1800's, Reynolds modified the governing equations by decomposing the flow variables into a mean and fluctuating component to describe the flow field [25]. For example, velocity u is decomposed into a time-averaged component, $\bar{u}_i$, and a fluctuating component, u_i'. Recall the momentum equation in three-dimensional, differential form from Equation 32:

$$\rho\frac{\partial u_i}{\partial t} + \rho u_j\frac{\partial u_i}{\partial x_j} + \frac{\partial p}{\partial x_i} - \frac{\partial \tau_{ij}}{\partial x_j} = 0 \tag{46}$$

where τ_{ij} is the stress tensor described in compact tensor notation, succinctly capturing Equations 14 and 17 as

$$\tau_{ij} = \mu\left(\frac{\partial u_i}{\partial x_j} + \frac{\partial u_j}{\partial x_i}\right) - \left(\frac{2\mu}{3}\right)\frac{\partial u_k}{\partial x_k}\delta_{ij} \tag{47}$$

where δ_{ij} represents a 3×3 identity matrix. After careful treatment of averaged correlated products, the Reynolds-averaged momentum equation is

$$\rho\frac{\partial \bar{u}_i}{\partial t} + \rho\bar{u}_j\frac{\partial \bar{u}_i}{\partial x_j} + \frac{\partial \bar{p}}{\partial x_i} - \frac{\partial}{\partial x_j}\left(\bar{\tau}_{ij} - \tau_{ij}^R\right) = 0 \tag{48}$$

The Reynolds-Averaged equation is formally identical to the Navier-Stokes equations with the exception of the additional stress term, $\tau_{ij}^R = \rho\overline{u_i' u_j'}$, which constitutes the Reynolds stress tensor and represents the transfer of momentum due to turbulent fluctuations. Boussinesq suggested that the apparent turbulent shearing stresses might be related to the rate of mean strain through an apparent scalar turbulent or "eddy" viscosity, μ_t. The Reynolds stress tensor is evaluated as

$$\tau_{ij}^R = 2\mu_t\bar{S}_{ij} - \frac{2}{3}\rho K\delta_{ij} \tag{49}$$

where turbulent kinetic energy is defined as

$$K \equiv \frac{1}{2}\overline{u_k' u_k'} \tag{50}$$

RANS turbulence models use the eddy viscosity or related parameters to close the momentum equation. Heat flux is solved similarly with a turbulent thermal conductivity, k_t. The gradient transport hypothesis states that viscosity and thermal

conductivity are simply the sums of the laminar and turbulent components.

$$\mu = \mu_l + \mu_t \tag{51}$$

$$k = k_l + k_t \tag{52}$$

Spalart-Allmaras Turbulence Model (Negative Form).

The Spalart-Allmaras (S-A) one-equation turbulence model was proposed in 1992 and enjoyed widespread use due to its speed and applicability across a wide variety of flows [33]. The model uses a single PDE to describe the transport of the turbulent kinematic viscosity parameter, $\tilde{\nu}$, or also referred to as the Spalart Allmaras working variable, as it is added to the vector of conserved variables. The parameter is related to the kinematic eddy viscosity ν_t as follows:

$$\tilde{\nu} = \frac{\nu_t}{f_{v1}} \tag{53}$$

where f_{v1} is a non-linear function of the ratio of $\tilde{\nu}$ to laminar kinematic viscosity, ν.

$$f_{v1} = \frac{\chi^3}{\chi^3 + c_{v1}^3}, \quad \chi = \frac{\tilde{\nu}}{\nu} \tag{54}$$

The transport equation is developed by empirical analysis of mean flow field relationships and dimensional assembly of plausible mathematical terms. The development starts with the left-hand side as a material derivative to describe the time rate of change of $\tilde{\nu}$ in a Lagrangian frame of reference. Expanding the material derivative, the convection of $\tilde{\nu}$ is described by

$$\frac{D\tilde{\nu}}{Dt} = \frac{\partial \tilde{\nu}}{\partial t} + u_i \frac{\partial \tilde{\nu}}{\partial x_i} \tag{55}$$

The right-hand side includes terms that account for the production ($\mathcal{P}$), destruction ($\mathcal{D}$), and diffusion of $\tilde{\nu}$. Each term will be outlined in turn and includes modifications made in 2012 [2] to address turbulence model behavior when $\tilde{\nu}$ becomes negative.

The production of eddy viscosity is highly related to the rotation of the flow. This critical and historical observation has been exploited by many preceding turbulence models including the Baldwin-Lomax algebraic model [3]. In a similar fashion, the originally proposed S-A model describes the turbulent viscosity parameter production as

$$\mathcal{P} = \begin{cases} c_{b1}(1 - f_{t2})\tilde{S}\tilde{\nu} & \text{for } \tilde{\nu} \geq 0 \\ c_{b1}(1 - c_{t3})S\tilde{\nu} & \text{for } \tilde{\nu} < 0 \end{cases} \tag{56}$$

where $\tilde{S}$ is the modified vorticity and is related to the magnitude of the mean rotation rate tensor, c_{b1} is a closure coefficient that was calibrated with non-homogeneous free shear flows, and f_{t2} is the trip term. The closure coefficients are tabulated in Table 1. To avoid the case where $\tilde{S} \leq 0$, Spalart offered the following correction for the definition of $\tilde{S}$ [32]

$$\tilde{S} = \begin{cases} S + \bar{S} & \text{for } \bar{S} \geq -c_{v_2}S \\ S + \dfrac{S\left(c_{v_2}^2 S + c_{v_3}\bar{S}\right)}{(c_{v_3} - 2c_{v_2})S - \bar{S}} & \text{for } \bar{S} \leq -c_{v_2}S \end{cases} \tag{57}$$

where c_{v2} and c_{v3} are empirically calibrated closure coefficients, S is the vorticity magnitude, and $\bar{S}$ is the mean vorticity:

$$S = \sqrt{\left(\frac{\partial w}{\partial y} - \frac{\partial v}{\partial z}\right)^2 + \left(\frac{\partial u}{\partial z} - \frac{\partial w}{\partial x}\right)^2 + \left(\frac{\partial v}{\partial x} - \frac{\partial u}{\partial y}\right)^2} \tag{58}$$

$$\bar{S} = \frac{\tilde{\nu} f_{v_2}}{\kappa^2 d^2} \tag{59}$$

where d is the distance to the closest wall and f_{v2} is a coefficient defined as

$$f_{v_2} = 1 - \frac{\chi}{1 + \chi f_{v_1}} \tag{60}$$

The destruction of $\tilde{\nu}$ near a wall is realized at a distance from the wall due to pressure. Dimensional analysis yields the functionality of a wall destruction source term to be related to the square of the ratio of $\tilde{\nu}$ to d:

$$\mathcal{D} = \begin{cases} \left(c_{w1} f_w - \dfrac{c_{b1}}{\kappa^2} f_{t2}\right)\left(\dfrac{\tilde{\nu}}{d}\right)^2 & \text{for } \tilde{\nu} \geq 0 \\ -c_{w1}\left(\dfrac{\tilde{\nu}}{d}\right)^2 & \text{for } \tilde{\nu} < 0 \end{cases} \tag{61}$$

where f_w is the destruction term, a dimensionally derived function of S, d, and $\tilde{\nu}$ that attempts to satisfy the law of the wall within the log layer. It uses a mixing length of $l = \sqrt{\tilde{\nu}/\tilde{S}}$ and normalizes by κd according to the observations of von Karman. The function f_w is defined with the following set of equations

$$\begin{aligned} f_w &= g\left[\frac{1 + c_{w3}^6}{g^6 + c_{w3}^6}\right]^{\frac{1}{6}} \\ g &= r + c_{w2}\left(r^6 - r\right) \\ r &= \min\left(\frac{\tilde{\nu}}{\tilde{S}\kappa^2 d^2},\, r_{\lim}\right) \end{aligned} \tag{62}$$

f_{t2} is the laminar suppression term and is defined as

$$f_{t_2} = c_{t_3} e^{\left(-c_{t_4}\chi^2\right)} \tag{63}$$

The diffusion term arises from the spatial gradients of $\tilde{\nu}$ that exist in the field.

The creators of the model chose to use a standard, non-conservative diffusion operator that can be solved with the first spatial derivatives of $\tilde{\nu}$.

$$\text{diffusion of } \tilde{\nu} = \frac{1}{\sigma}\left[\frac{\partial}{\partial x_j}\left((\nu + f_n\tilde{\nu})\frac{\partial}{\partial x_j}\tilde{\nu}\right) + c_{b2}\left(\frac{\partial}{\partial x_j}\tilde{\nu}\right)^2\right] \tag{64}$$

where f_n is the diffusion coefficient defined as

$$f_n = \begin{cases} 1 & \text{for } \tilde{\nu} \geq 0 \\ \dfrac{c_{n1} + \chi^3}{c_{n1} - \chi^3} & \text{for } \tilde{\nu} < 0 \end{cases} \tag{65}$$

As a final note, the kinematic eddy viscosity ν_t is modified for negative cases:

$$\nu_t = \begin{cases} \tilde{\nu} f_{v1} & \text{for } \tilde{\nu} \geq 0 \\ 0 & \text{for } \tilde{\nu} < 0 \end{cases} \tag{66}$$

These adjustments maintain the original S-A model for $\tilde{\nu} \geq 0$ and use the negative model defined for $\tilde{\nu} < 0$. Combining all major components of eddy viscosity parameter transport, the complete S-A turbulence model in dimensional, differential form is

$$\frac{\partial\tilde{\nu}}{\partial t} + u_j\frac{\partial\tilde{\nu}}{\partial x_j} = \mathcal{P} - \mathcal{D} + \frac{1}{\sigma}\left[\frac{\partial}{\partial x_j}\left((\nu + f_n\tilde{\nu})\frac{\partial}{\partial x_j}\tilde{\nu}\right) + c_{b2}\left(\frac{\partial}{\partial x_j}\tilde{\nu}\right)^2\right] \tag{67}$$

The model is complete with the following set of closure coefficients shown in Table 1 that were calibrated with a set of empirical cases.

Constant	Value
σ	$2/3$
κ	0.41
c_{b1}	0.1355
c_{b2}	0.622
c_{w1}	$c_{b1}/\kappa^2 + (1 + c_{b2})/\sigma$
c_{w2}	0.3
c_{w3}	2
c_{v1}	7.1
c_{v2}	0.7
c_{v3}	0.9
c_{t3}	1.2
c_{t4}	0.5
r_{lim}	10

Table 1. Closure Constants for the Negative SA Turbulence Model

Large Eddy Simulation and Detached Eddy Simulation.

The basis of large eddy simulation (LES) is the observation that the small, turbulent structures are more universal in character than the large eddies in fluid flow. Therefore, the idea is to directly compute the large, energy-carrying eddy structures and model the effects of the small structures, which are not resolved by the numerical scheme. This is accomplished by a spatial filtering operation, which decomposes the flow variables into a filtered (large-scale, resolved) part and a sub-filter (subgrid-scale, unresolved) part. The subgrid-scale models are much simpler than the turbulence models for the RANS equations due to the homogeneous and universal character of the small scales.

LES still remains too costly for complex engineering configurations so Spalart et al. suggested the detached eddy simulation (DES) methodology, which is aimed at the simulation of massively separated flows at high Reynolds number [32, 35]. DES is a hybrid turbulence model that uses RANS to resolve the attached boundary layer and LES to model the detached eddies in regions of separation. Thus, DES combines the strengths of both methods in a single framework. The algorithm determines the mode of operation (RANS or LES) based on the length scale

$$d_{\text{DES}} = \min(d, C_{\text{DES}}\Delta) \tag{68}$$

where d_{DES} is the distance to the wall, C_{DES} is a constant of order one, and $\Delta = \max(\Delta x, \Delta y, \Delta z)$ is the grid spacing measure.

Delayed Detached Eddy Simulation.

Spalart et al. introduced delayed detached eddy simulation (DDES) to avoid an undesired switch to LES within the boundary layer where there is inadequate refinement [34]. The parameter, r, was redefined from Equation 62 to improve robustness in irrotational regions:

$$r_d = \frac{\tilde{\nu}}{\sqrt{U_{i,j}U_{i,j}}\kappa^2 d^2} \tag{69}$$

The parameter, r_d, is used in the function

$$f_d = 1 - \tanh\big([8r_d]^3\big) \tag{70}$$

The new function is applied to the DES length scale to "delay LES function" by defining

$$\tilde{d} = d - f_d \max(0,\, d - C_{DES}\Delta) \tag{71}$$

such that $f_d = 0$ activates RANS mode in the boundary layer and $f_d = 1$ activates LES (Equation 68). These modifications brought significant improvements to attached boundary layer modeling and flow separation detection during simulation [34].

2.4 Bleed Flow Coefficient

Over the years, experiments exploring flow through bleed holes were conducted and a large library of bleed flow data were developed beginning with McLafferty and Ranard [19] and include notable works by Syberg and Hickcox [36], Shaw [29], and Willis [41]. The database built by these efforts cover a range of bleed hole geometries, orientations, and configurations and paved the way for the characterization of bleed configuration data by normalizing flow characteristics by a flow coefficient (Q), which is defined as

$$Q = \frac{\dot{m}_{\text{bleed}}}{\dot{m}_{\text{sonic}}} \tag{72}$$

where $\dot{m}_{\text{bleed}}$ is the mass flow rate through the bleed hole and defined in the general form as

$$\dot{m}_{\text{bleed}} = \rho v A = p_t A M \left(\frac{\gamma}{RT_t}\right)^{\frac{1}{2}} \left(1 + \frac{\gamma - 1}{2} M^2\right)^{\frac{-(\gamma+1)}{2(\gamma-1)}} \tag{73}$$

and $\dot{m}_{\text{sonic}}$ is the ideal mass flow rate given a Mach number at isentropic, compressible gas conditions in the general form

$$\dot{m}_{\text{sonic}} = p_t \Phi A_{\text{region}} \left(\frac{\gamma}{RT_t}\right)^{\frac{1}{2}} \left(\frac{\gamma + 1}{2}\right)^{\frac{-(\gamma+1)}{2(\gamma-1)}} \tag{74}$$

The definition for $\dot{m}_{\text{sonic}}$ in Equation 74 includes the bleed porosity term, Φ, which is defined as

$$\Phi = \frac{A_{\text{region}}}{A_{\text{bleed}}} \tag{75}$$

where A_{bleed} is the cross-sectional area of the bleed holes and A_{region} is the total area

of the region. The total pressure, p_t, and total temperature, T_t at the boundary layer edge above the bleed region were used for the above equations. The flow coefficient Q thus represents the efficiency of the bleed hole in extracting flow compared to the theoretical maximum extracted flow. The theoretical maximum does not change for the given conditions so an increase (or decrease) in Q reflects an increase (or decrease) in $\dot{m}_{\text{bleed}}$ as $\dot{m}_{\text{sonic}}$ remains constant.

The pressures upstream and downstream of the bleed hole are the main factors that affect the flow coefficient, Q, and so the pressure is also normalized as a pressure ratio between the plenum static pressure and the total pressure at the edge of the approaching boundary layer $\frac{p_{\text{plenum}}}{p_{t\delta}}$ where p_{plenum} denotes the plenum static pressure, the subscript t denotes the total property of the variable, and the subscript δ denotes the property of the variable at the edge of the boundary layer. The physics of bleed flow are such that for a given Mach number as the plenum static pressure is reduced (e.g. the pressure ratio), the bleed mass flow rate, $\dot{m}_{\text{bleed}}$, and in turn the flow coefficient, Q, increases until the flow through the hole chokes and asymptotically approaches a maximum value. Figure 2 illustrates the decrease in Q as the Mach number increases, which reflects a decreased bleeding efficiency as the Mach number increases.

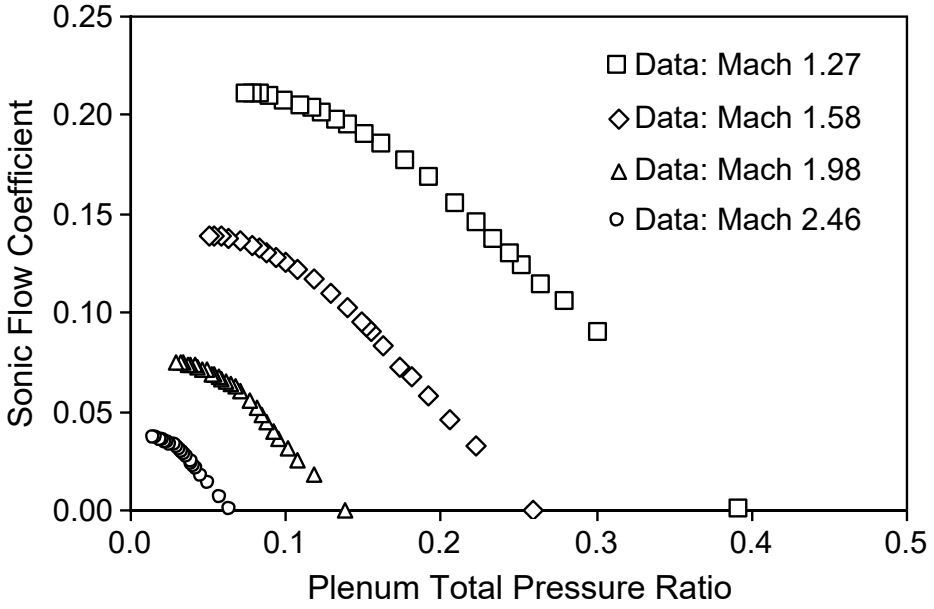

Figure 2. Data from Willis et al. [41] normalized by the total pressure at the boundary layer edge [31]

III. Methodology

3.1 Grid Generation

Overset grids allow communication between multiple grids to act as one, large grid. One advantage of the overset methodology allows users to model complex and sophisticated topologies. Another advantage is the ability to easily add or remove grids from the grid system which allows users to circumvent the time-consuming process of regenerating meshes. The current research uses overset methodology for the advantages described above in addition to the fact that this research builds on previous work done using overset grids.

Chimera Grid Tools.

Chimera Grid Tools (CGT) is a software suite developed at NASA Ames [8] that contains a large collection of tools for building, modifying, and diagnosing overset grids for CFD applications. The CGT software contain a large number of Fortran and Tool Command Language (TCL) programs that are called in batch mode but wrapped into a main graphical user interface (GUI) called OVERGRID [9]. The GUI facilitates the generation of grids for a new flow configuration and once the user becomes familiarized with the tools, the grid generation process can be automated for similar configurations.

The scripting tools in the CGT suite were used to create surface geometry that were extruded into the flow to create the CFD domain. The scripts were also configured to produce the input files necessary for the grid assembly process discussed in the next section. For force and moment calculations over a surface, the Force and Moment Computation (FOMOCO) tool is used to generate the appropriate inputs. The grid file must be a Fortran, double-precision, unformatted PLOT3D file. Grids

were checked to assure that they are right-handed and have no negative volumes.

Pegasus.

PEGASUS 5 is a CFD pre-processing grid assembly code that generates the overset communication files required for OVERFLOW. The code prepares the overset volume grids for the flow solver by computing the domain connectivity database and blanking out grid points so that points contained inside a solid body and excess points between overlaps are not visualized. The code also automatically detects outer and internal boundary conditions and defines the appropriate connectivity [26]. PEGASUS determines the best stencil between two overlapping grids and blanks out the excess, achieving the best overlap communication. PEGASUS 5 was designed to be an automatic process that requires a minimal OVERFLOW input file and the pre-assembled volume grids. The code is compiled using Message-Passing Interface (MPI), allowing it to run in parallel and decrease run time.

3.2 Flow Solver

The mathematical basis for CFD was detailed in Chapter II. The implementation of these calculations is performed through a sophisticated computer program optimized to numerically solve the Navier-Stokes equations. The program this research used was OVERFLOW.

OVERFLOW 2.2 is a three-dimensional, structured, overset, finite-difference, parallelized, Navier-Stokes CFD code developed by NASA [7]. OVERFLOW derives its name from an acronym for "OVERset grid FLOW solver."

OVERFLOW employs several different inviscid flux algorithms, various implicit solution algorithms, a wide variety of boundary conditions, and a number of algebraic, one-equation, and two-equation turbulence models.

A notable feature of OVERFLOW is the diagonal form of the implicit approximate factorization algorithm of Pulliam and Chaussee [24], making OVERFLOW one of the fastest available codes for obtaining steady-state solutions.

OVERFLOW features several convergence acceleration techniques, but only grid sequencing and multigrid were used for this research. Grid sequencing improves convergence by initially running the solution on coarser grids, allowing the solution to set up quickly and for the proper mass flow to quickly develop. In a multigrid algorithm, the solution is updated with contributions from coarser grid levels at each time step, allowing low frequency error waves to convect rapidly out of the computational domain.

The OVERFLOW code was compiled with MPI for parallel computing and with double-precision for accuracy. MPI automatically decomposes the grid system and distributes the work between processors to achieve the best load-balance possible, allowing computations to be performed on larger HPC servers. The double-precision floating point number format represents numerical values with more significant digits, reducing round-off error.

3.3 Bleed Flow Analysis

Mayer and Paynter Model.

Abrahamson et al. [1] and Chyu et al. [10], to name a few, developed bleed boundary conditions for CFD but did not account for the changes in bleed mass flow rates as a shock moves over the bleed region. The bleed boundary conditions assumed that the bleed flow rate was both fixed and independent of the shock position so the mass flow rates were fixed at a certain distribution and did allow for changes in the flow coefficient as local properties changed due to shock movement. Since the flow coefficient of the bleed holes depends significantly on the local flow conditions (upstream

or downstream of the normal shock position), the bleed boundary condition affects the motion of the normal shock in the throat, as noted by Paynter et al. [22].

Mayer and Paynter [18] overcame some of these challenges by creating a bleed boundary condition model that assumes removing the proper mass flow from the flow based on local conditions is more important than imposing a fixed mass flow rate distribution over a bleed region when performing an accurate simulation of normal shock motion. Thus, the bleed boundary condition is a "global" model of the effects of bleed on the inlet and can account for changes in local properties.

The boundary condition imposes a velocity normal to the wall at the surface to achieve the appropriate mass flow. The velocity is determined by the flow coefficient Q necessary at the given local conditions, which is based on the bleed hole porosity, Φ, and the maximum bleed rate, $\dot{m}_{\max}$. The flow properties at the edge of the boundary layer is determined to calculate $\dot{m}_{\max}$ and the value of Q is interpolated from a lookup table of data from Syberg [36] and McLaugherty [19], which is a function of the bleed hole angle, the bleed plenum pressure, and the local flow properties. The use of the Q data for the bleed model requires the CFD code to compute the Mach number, total pressure, and total temperature at the edge of the boundary layer, which is assumed to be the same as the total temperature in the plenum of the wind tunnel facility.

$$Q_{\text{sonic}} = \frac{\dot{m}_{actual}}{\dot{m}_{max}} = f\left(\alpha_{bleed}, M_{local}, \frac{p_{plenum}}{p_{t,local}}\right) \tag{76}$$

where $\dot{m}_{max}$ is the max theoretical flow at the local stagnation pressure and stagnation temperature. The local flow properties are taken at the wall for the inviscid flows or from the grid point that is just beyond the edge of the boundary layer for viscous flows.

The bleed model of Mayer and Paynter had drawbacks for CFD simulations. Determining the edge of the boundary layer above the bleed region is a complex and

expensive task for CFD. Not only is the edge of the boundary layer not well-defined, bleed is desirable in regions of shock wave/boundary-layer interactions and flowfields with extensive boundary layer separation prohibit the accurate definition of such a boundary.

In an effort to overcome these challenges, collaborative efforts between Davis [12] and Slater [31] sought to characterize bleed data with respect to the surface conditions instead of at the edge of the boundary layer. This was accomplished by observing in Figure 2 that the normalization curves for various Mach numbers could be collapsed into a single distribution given the proper reference property.

Both investigators took the approach of normalizing the bleed plenum pressure by the local surface static pressure, but Davis also included a coefficient to account for the slight overpressure of the bleed plenum at zero flow rates. As for the models themselves, Slater assumed for 90° holes that the total pressure in the hole was approximately equal to the local surface static pressure and Davis established a purely empirical scaling based on the extrapolated choked value of the bleed plate.

Davis Model.

The Davis model is included for reference and the scaled empirical correlation takes the form of:

$$Q_{scaled} = \frac{Q}{e + f \cdot M_\delta^2 + g \cdot e^{M_\delta}} \tag{77}$$

where the coefficients are defined in Table 2

Coefficient	Value
e	-6.885241
f	-5.9569877
g	5.9532869

Table 2. Coefficients for the Davis scaled empirical model as a function of Mach number [11].

The pressure ratio $p_{plenum}/p_{t,\delta}$ is scaled by the pressure at the surface, p_B

$$p_{plen,scaled} = \frac{p_{plen}}{p_{t,\delta}} \cdot \frac{p_{t,\delta}}{p_B} \tag{78}$$

which yields a scaled pressure ratio defined as

$$\frac{p_{t,\delta}}{p_B} = 1.059 \cdot \left(1 + \frac{\gamma - 1}{2} \cdot M_e^2\right)^{\frac{\gamma}{\gamma - 1}} \tag{79}$$

Taking the data of Willis et al. [41] and applying the scaling defined above in Equation 77 and Equation 79, an empirical fit is defined

$$Q_{scaled} = a + \frac{b}{1 + \left(\frac{p_{plen,scaled}}{c}\right)^d} \tag{80}$$

where the coefficients are defined in Table 3

Coefficient	Value
a	-0.74177271
b	1.7397157
c	0.91473254
d	3.2074431

Table 3. Coefficients for the Davis scaled empirical model as a function of the plenum pressure ratio [11].

Davis concluded that the scaling method presented by Slater was a better, but imperfect, fit for single-hole data than the scaling method Davis previously proposed based upon a semi-empirical correlation of the data collected by Willis [12].

Slater Model.

Slater's model is not based on a direct curve fit of the scaled data and removes the Mach number at the edge of the boundary layer as a factor by assuming the total pressure in the hole is nearly the same as the surface wall static pressure. This is

a reasonable assumption for holes with large inclination angles as all the freestream total pressure is lost turning the flow through a large angle and as such, the model is based on only 90 degree hole data from Willis et al. [41]. The new scaling defined an alternative reference flow from the total pressure at the edge of the boundary layer to the static pressure at the surface of the bleed region (the same as Davis) and takes the form

$$\dot{m}_{\text{max-B}} = \Phi A_{\text{region}} p_B \left(\frac{\gamma}{RT_B}\right)^{\frac{1}{2}} \left(\frac{\gamma+1}{2}\right)^{\frac{-(\gamma+1)}{2(\gamma-1)}} \tag{81}$$

The total conditions were replaced with the static pressure and temperature at the boundary surface local to the bleed hole, denoted by the subscript B. The flow coefficient (Equation 72) was scaled to a surface flow coefficient by a factor as shown below

$$Q_{\text{B}} = \frac{\dot{m}_{\text{bleed}}}{\dot{m}_{\text{max-B}}} = \frac{\dot{m}_{\text{bleed}}}{\dot{m}_{\text{max}}} \left(\frac{\dot{m}_{\text{max}}}{\dot{m}_{\text{max-B}}}\right) \tag{82}$$

The assumption was made that the surface static pressure is very close to the static pressure at the edge of the boundary layer, allowing for the following equation using isentropic conditions

$$\frac{p_{t\delta}}{p_B} = \left(1 + \frac{\gamma-1}{2} M_\delta^2\right)^{\frac{\gamma}{(\gamma-1)}} \tag{83}$$

and that the total temperature at the edge of the boundary layer is approximately equal to the static temperature at the bleed region boundary as defined below

$$\left(\frac{T_B}{T_{t\delta}}\right)^{\frac{1}{2}} \approx 1 \tag{84}$$

The flow coefficient was scaled through the following operations

$$Q_{\text{sonic-B}} = Q\left(\frac{p_{t,\delta}}{p_B}\right) \tag{85}$$

$$\frac{p_{\text{plenum}}}{p_B} = \frac{p_{\text{plenum}}}{p_{t\delta}} \left(\frac{p_{t\delta}}{p_B} \right) \tag{86}$$

The flow coefficients presented in Figure 2 were scaled using Equation 85 and Equation 86 and the results are shown in Figure 3. The scaled data collapsed along a trend such that the surface sonic flow coefficient only varied with respect to the scaled static pressure ratio (p_{plenum}/p_B), removing Mach number at the boundary-layer edge as a dependent factor.

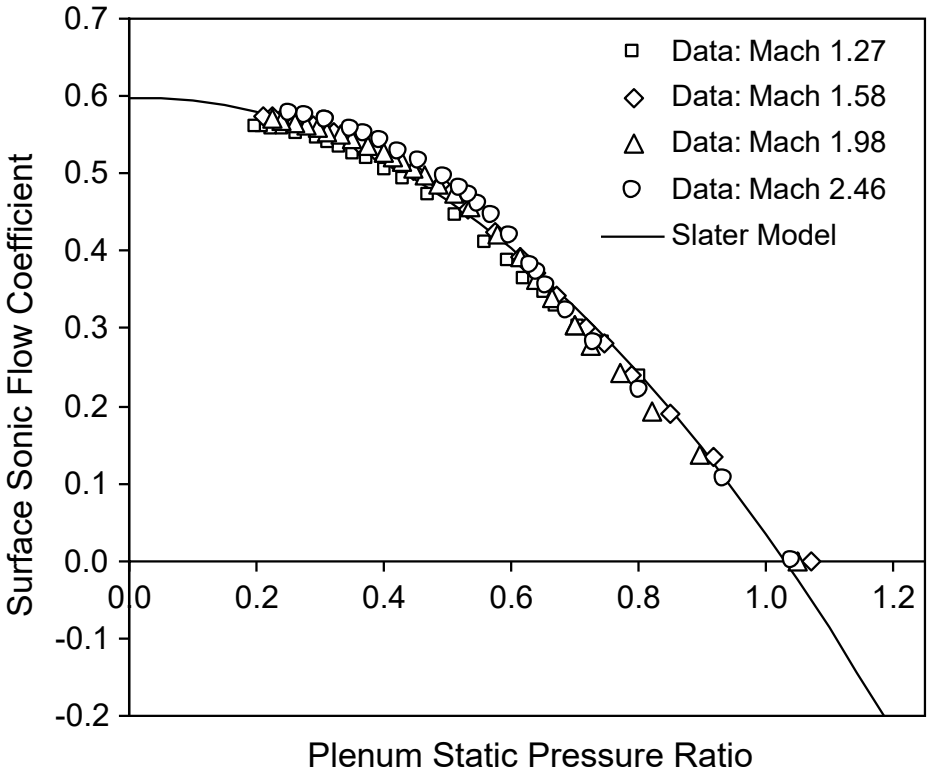

Figure 3. Data from Willis et al. [41] normalized by the bleed surface static pressure [31]

A quadratic curve was fitted to the scaled data in Figure 3 with coefficients defined in Table 4 of the general form

$$Q_{scaled} = -a \cdot (p_{plen,scaled})^2 + b \cdot (p_{plen,scaled}) + c \tag{87}$$

Coefficient	Value
a	0.59361420
b	0.03069346
c	0.59799735

Table 4. Coefficients for the quadratic fit of the Slater model

The Slater scaling (Equation 87) was applied to the sonic flow coefficients data sets collected by Syberg [36] and Mayer et al. [18] to examine whether the scaling worked for other data sets. Figure 4 shows the results of that scaling along with the plot of Equation 87. There is greater variation in the scaled values than shown in Figure 3, but the curve fit of Equation 87 does well in characterizing the data except at Mach 1.0, where the curve fit indicates lower values for the surface flow coefficient. Comparisons between Figures 2, 3, 4a and 4b suggest that the curve fit may not work well for characterizing bleed rates below Mach 1.27 and Mach 2.5 and above. Beyond sonic and higher supersonic Mach numbers, the Slater curve fit (Equation 87) is a reasonable representation of the behavior of the surface flow coefficient as a function of the plenum pressure ratio.

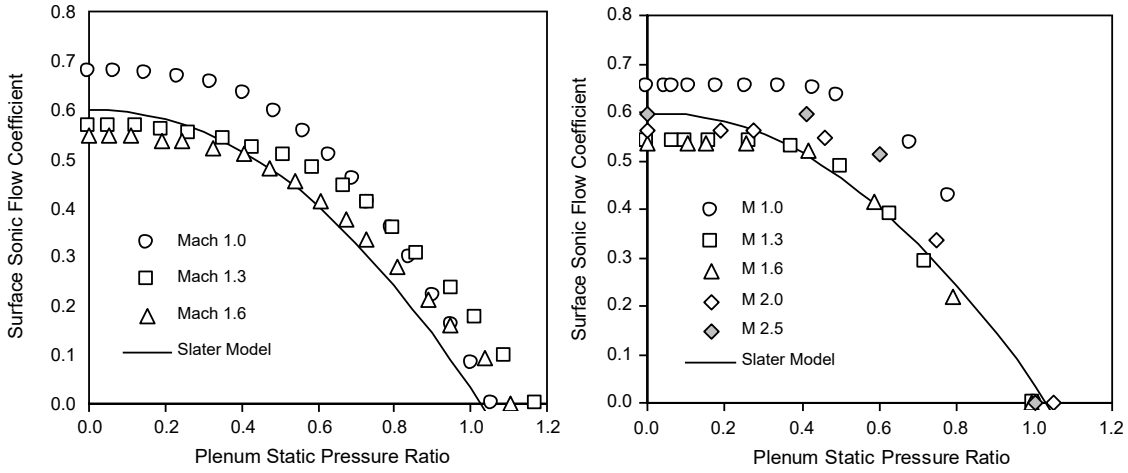

(a) Data from Syberg [36] normalized by the bleed surface static pressure [31]

(b) Data from Mayer [18] normalized by the bleed surface static pressure [31]

Figure 4. The Slater model compared to other experimental data sets

The model is convenient as a boundary condition model since the scaled reference properties at the surface of the bleed region (surface static pressure and temperature) are easily obtained in a CFD simulation. An additional benefit is that rudimentary blowing is implemented if the pressure ratio exceeds 1.03. Negative flow coefficients result in negative bleed flow by Equation 72. While large amounts of blowing are not intended in the design of a supersonic inlet, it is possible to experience blowing behind a shock wave as the high pressure downstream of the shock can exceed the plenum pressure.

A slight modification to Equation 87 was proposed by Dorgan [14] to remove the first-order term so choking was reflected in the model at low plenum pressure ratios. The original Slater model exhibited positive slope at low plenum pressure ratios below 0.026, falsely displaying increasing bleed as the plenum pressure ratio approaches zero. To show the choking effect, the following modification was made to Equation 87 [14]

$$Q_{sonic-B} = -0.57 \cdot \left(\frac{p_{plenum}}{p_B} \right)^2 + 0.6 \tag{88}$$

This alternative curve-fit differs in shape only slightly and not distinguishable if plotted. What this model does not account for are hole angles, hole depth, plate thickness, and effects due to multiple holes.

In summary, Slater's model overcomes the challenges of the Mayer-Paynter bleed model by introducing a different scaling for the flow coefficient. The scaling collapses previous data for various Mach numbers to a single distribution that was fitted with a quadratic polynomial as a function of only the plenum pressure ratio. The flow properties at the edge of the boundary no longer need to be computed and the model allows for changes in bleed flow rates due to local conditions to include blowing. This model is used as an instrumental model to both verify and guide the current research.

Previous Experimental Results.

The validation of the Slater model was performed by Slater [30] using CFD and comparing to 90° single bleed hole experiment [28]. The experiment used a bleed hole drilled into a removable disk, mounted flush with the bottom of the test section of the NASA Glenn Research Center 15 cm by 15 cm wind tunnel. The boundary layer over the plate was the naturally-occurring boundary layer on the bottom surface of the wind tunnel. The flow conditions and approaching boundary layer profile over the bleed region were measured with a translating pitot probe and wall static pressure ports at a reference station located 2.46 inches ahead of the bleed hole center. The reference properties are described in Table 5 below.

Parameter	Value
Mach Number	2.46
Hole Diameter, D [in.]	0.236
Plate Thickness, t [in.]	0.472
Reynolds Number per Foot	5.15E+06
Total Pressure, p_t [psia]	25.0
Boundary Layer Thickness, δ [in.]	0.5079

Table 5. Reference conditions at the boundary layer edge and 2.46 inches ahead of the bleed hole center used in the Slater computational simulation [30]

A cylindrical bleed plenum with a ducted vacuum exhaust was used to decrease the plenum pressure and pull air through the bleed hole. The plenum measured 2.874 inches in diameter with an axial length of 3.50 inches and was concentrically aligned to the bleed hole center. The mass flow rate was measured using a calibrated nozzle. The uncertainty of the experimental data was reported as ±1.5% for total pressures and ±1% percent for values of the flow coefficient, Q.

Previous Computational Results.

The CFD simulation performed by Slater was set up to reproduce the same reference properties as the experiment in Table 5 so that the sonic coefficients were

accurately compared and the Slater model validated with both CFD and experiment. The main consideration in reproducing the reference properties was the location of the inflow boundary condition, which was positioned 38.46 inches upstream of the center of the bleed hole.

The outflow boundary was positioned 5.0 inches downstream of the center of the bleed hole and a first-order extrapolation boundary condition was used for the supersonic outflow. The plenum was modeled as a cylinder with a converging-diverging nozzle directed downward for the outflow for the plenum. The exit for the plenum nozzle was located 6.472 inches below the bottom wall of the tunnel and the static pressure was specified on the subsonic outflow boundary condition, allowing for control of the plenum pressure and thus, the pressure ratio. The walls of the plenum and bleed hole were specified as adiabatic, no-slip boundary conditions.

At each iteration, convergence was evaluated by monitoring both the mass flow rate through the bleed hole and the plenum static pressure. The mass flow rate was measured at the plenum exit where there was no recirculation, ensuring an accurate evaluation of the mass flow. The plenum pressure was obtained by mass-averaging the static pressure on a horizontal plane at the start of the nozzle.

A grid-independence study was conducted at approximately 75% of the maximum bleed rate value by skipping every other grid point on a fine grid to obtain a medium and coarse grid. The S-A and Menter SST turbulence models were applied separately to each set of grids to assess the effects of turbulence modeling. Both turbulence models produced the same result and the medium grid showed little deviation from the fine grid, so the medium grid using the Menter SST turbulence model was evaluated to be grid-independent.

The variation of the flow coefficient is shown Figure 5. The results of the CFD simulations matched well with the data. This strongly suggests that CFD simula-

tions can be used to obtain flow coefficient data, Q, for bleed configurations or flow conditions for which experimental data is not available. The curve fit of Equation 87 is also plotted and compares well to the data and CFD simulation. The curve fit was based on experiments with multiple rows of bleed holes. This suggests that a test or CFD simulation with a single bleed hole can be used to obtain flow coefficient data. Bodner [6] noted the single-hole data compared well to the multiple-hole data of Willis et al. [40] and suggested the hole interactions were not significant for that data set for 90-degree bleed holes.

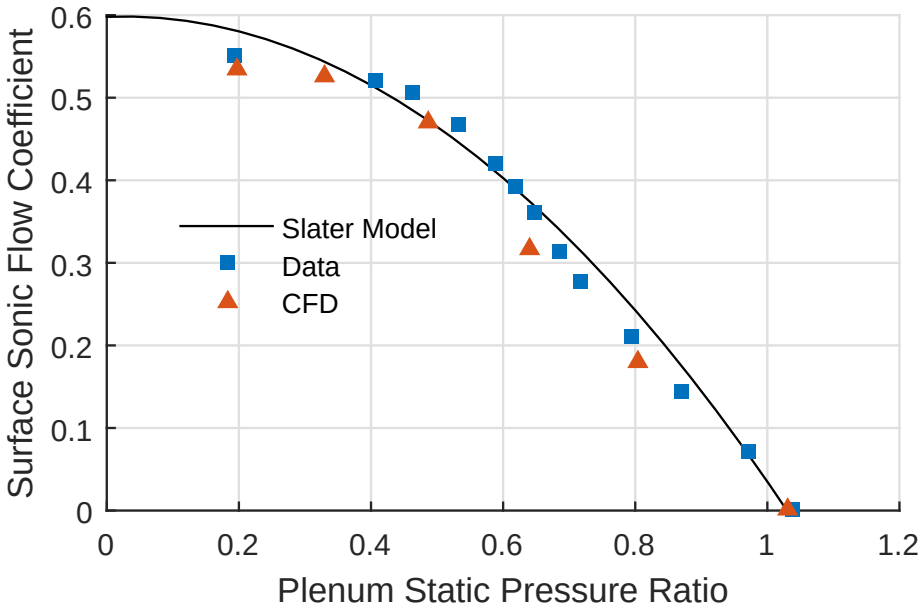

Figure 5. Sonic flow coefficients for bleed flow through a single bleed hole [29].

IV. Results and Analysis

4.1 Three-Dimensional Wind Tunnel Model

This research began with the motivation to aid in shock stabilization designs on a wind tunnel model by exploring bleed hole sizes and patterns on a three-dimensional tunnel model in supersonic flow. The grid system for the model was developed with the following design variables in mind: plate thickness, hole location, hole radius, plenum size (length, width, depth, position), boundary condition size, and the pressure ratios. The large number of design variables were chosen with the intent of an exploratory design phase in mind. The model geometry was composed of a flat surface for boundary layer growth, a bleed hole, a model, and a plenum to pull the air.

A key concern was ensuring that the correct boundary condition was applied inside the plenum so that the flow interaction in and around the bleed flow wasn't inaccurately perturbed by the mechanism of air being pulled out the plenum. A related concern was ensuring the imposed boundary condition would not introduce numerical errors into the flow in the plenum. Since the flow is an internal flow problem in the plenum, ensuring information from the boundary condition did not propagate upstream was another concern. A final concern was applying the correct boundary condition that would model the physical mechanism of massflow being pulled from the plenum.

Two options were proposed in modeling the mechanism of air pull in the plenum: the first used a choked converging-diverging nozzle to prevent information propagation upstream; the second used a specified pressure at the boundary condition to set a plenum pressure. The first option seemed ideal in mitigating the concerns mentioned above but required greater computational effort than the second option so the pressure boundary condition was implemented as part of the initial investigation.

Four grids were generated. The first was the model grid that was embedded with the bleed hole and plenum grids. For simplicity, significant effort went into modeling the bleed hole with as few grids as possible, which was managed with two grids. First, a hollow, cylindrical grid with collars on both ends was used to define the walls of the hole and interface with the plate grid and the plenum grid. A second, rectangular prism grid filled the hollow space in the cylindrical grid. A final plenum grid was placed under the bleed hole and inside the model grid with a specified pressure boundary condition patch centered on the downstream wall. The dimensions are specified in Table 6. The plenum was roughly sized such that the specified pressure boundary condition was deemed far enough not to interact with the flow in and around the bleed hole.

Grid Parameter	**Value**
Hole Depth	0.25”
Hole Radius	0.0465”
Number of Circumferential Points	93
Circumferential Spacing	0.00314”
Suction Patch Length	1.0”
Suction Patch Width	1.0”
Initial Wall Spacing	0.00005”
Maximum Spacing	0.001”
Growth Factor	1.3
Plenum Length	4.0”
Plenum Width	3.0”
Plenum Depth	1.0”

Table 6. Mesh parameters for the three-dimensional wind tunnel model in freestream flow

The initial mesh generation required careful grid topology consideration so that both orphan points and the overall number of cells were minimized. No first-level orphan points were accepted since that is a significant overset error and a small number of second-level fringe points were allowed in special situations. During the hole-cutting process, the grids were given specific parameters to instruct PEGASUS

to cut the proper holes. This amounted to tedious book-keeping, which made errors frequent during mesh generation and hole-cutting. Two examples of failed hole-cutting are shown in Figure 6.

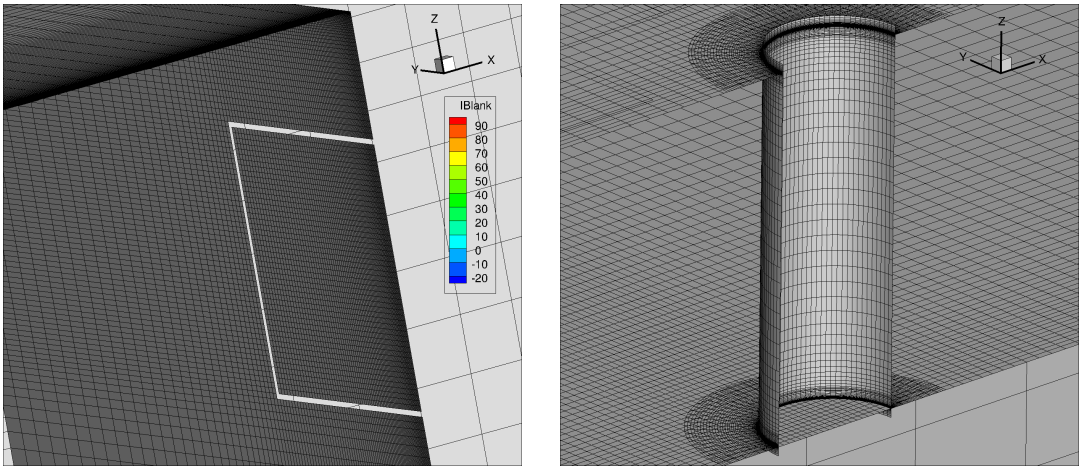

Figure 6. Errors in the mesh during the hole-cutting process

The simulation was performed in freestream for 20,000 iterations to ensure the residuals dropped 6 orders of magnitude or greater. The multigrid approach was used on the first 9,000 iterations to accelerate solution convergence. The flow parameters set are shown in Table 7. One simulation was performed with the specified pressure on the plenum outflow boundary at 0.30 times the freestream pressure and the other simulation was performed the with the specified pressure at 0.15 times the freestream pressure.

Flow Parameter	**Value**
Mach Number	1.5
Temperature	386.0°R
Reynolds Number per Foot	0.25 Million
Turbulence Model	Spalart-Allmaras
Inviscid Flux Scheme	HLLC Upwind
Implicit Solver	SSOR Algorithm

Table 7. Flow simulation parameters for the tunnel model in freestream air.

Flow features within the hole are shown in Figure 7 for both simulations. Figure 7a

shows the flow turning and accelerating supersonically into the bleed hole and out into the plenum at both pressure ratios, similarly to a freestream jet flow. Figure 7b shows the shock structure outlined by contours of density gradient magnitude, confirming the similarity to freestream jet flow. No evidence of sharp flow turning from the freestream into the bleed hole is seen in either figures, contradicting previous literature that shows a significant change in the flow to redirect the flow around the sharp corner and through the bleed hole. Figure 7c shows contours of pressure, revealing the pressure above the bleed hole is significantly higher than the freestream pressure. The bleed hole perturbs the incoming boundary layer, triggering a shock upstream that causes a pressure recovery and a reduction in flow speed, allowing the flow to turn through the bleed hole subsonically. The pressure recovery creates a higher pressure differential on either sides of the bleed hole than initially intended that forces the flow to quickly accelerate to supersonic speeds and allows for the freestream jet flow to set up through the bleed hole.

Two more simulations were run at different plenum pressures and the sonic flow coefficients were plotted with a quadratic fit in Figure 8. The modified sonic flow equations (Equation 87) used to plot the results assumed the hole was in freestream flow, therefore, the freestream pressure was used as the pressure at the edge of the boundary layer approaching the bleed hole. Since the incoming boundary layer for this simulation interacted with two shocks, the freestream pressure cannot be used as the pressure at the edge of the boundary layer as evidenced by Figure 7c, which show the boundary layer pressure to be at least 1.6 times the freestream pressure. Since the assumptions of the modified sonic flow equations were not met, 4 different methods for determining a suitable boundary layer edge pressure were used in Figure 8.

A surface contour of non-dimensional pressure just above the model surface is shown in Figure 9. The legend uses a red and blue diverging color bar such that white

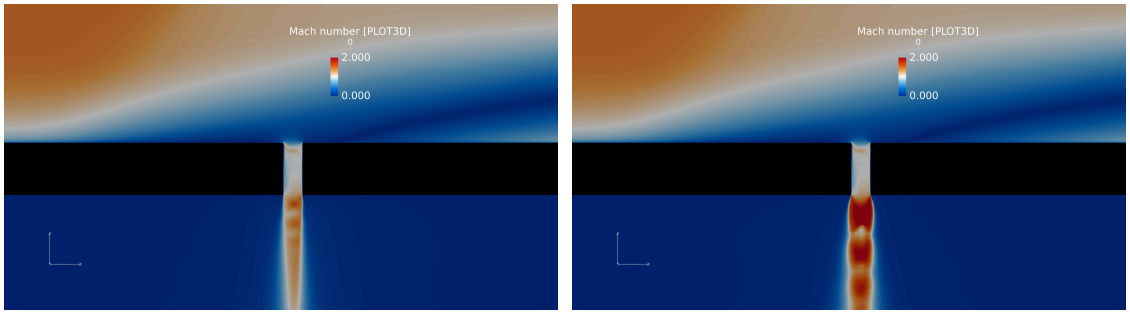

(a) Contours of Mach number for pressure ratios of approximately 0.50 (left) and 0.25 (right).

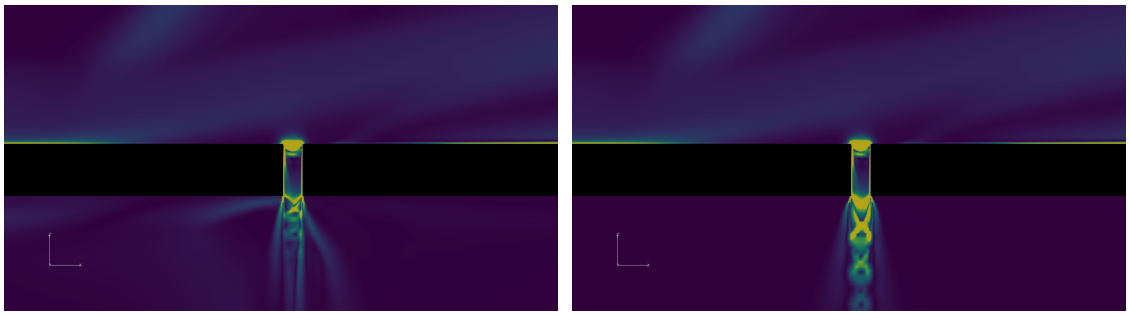

(b) Contours of density gradient magnitude for pressure ratios of approximately 0.50 (left) and 0.25 (right).

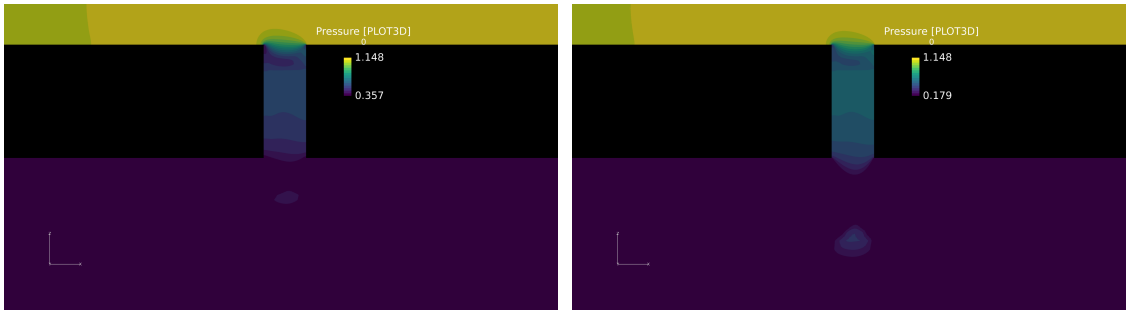

(c) Contours of nondimensionalized static pressure for pressure ratios of approximately 0.50 and 0.25, respectively.

Figure 7. Visualizations of bleed flow within the three-dimensional wind tunnel model simulation

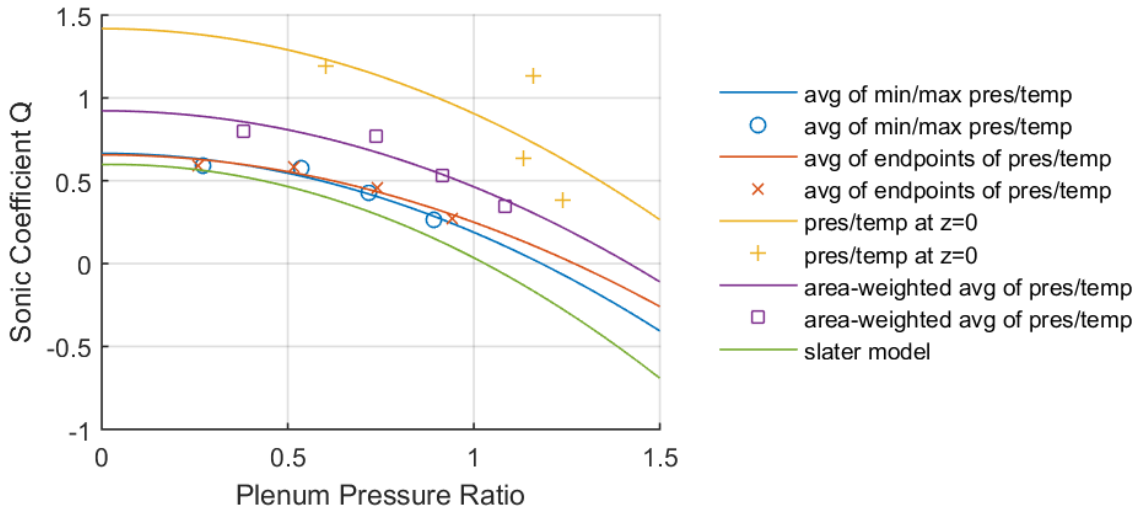

Figure 8. Quadratic fit of the massflow through the wind tunnel model bleed hole at various pressure ratios and compared to the Slater model.

areas represent freestream pressure, red represents pressure greater than freestream, and blue represents pressure less than freestream. From Figure 9, the shock off the leading edge of the model causes a pressure rise along the surface of the model so that the local pressure near the bleed hole is slightly higher than that of freestream, confirming the the failure to meet the assumptions of the modified sonic flow equations and the results from Figure 7.

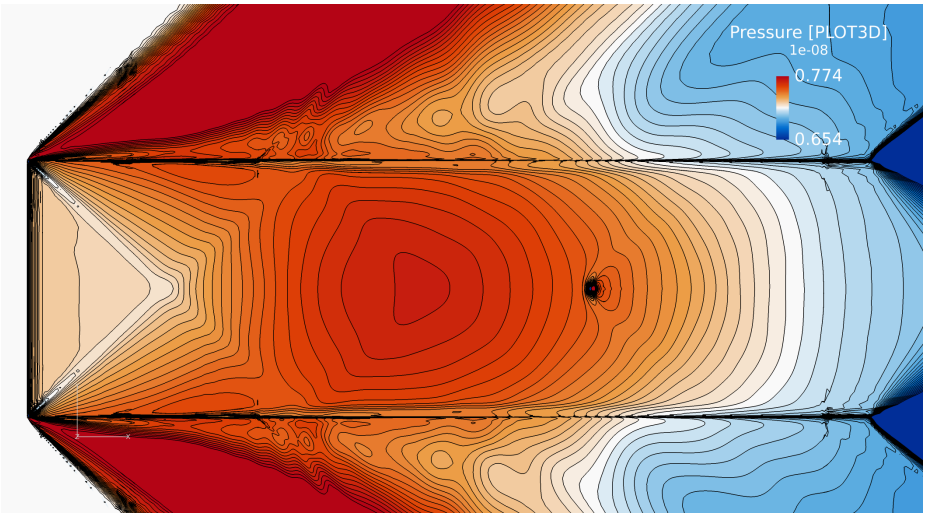

Figure 9. Pressure contour of the wind tunnel model along the surface.

Scaling the massflow in Figure 8 proved to be too difficult so the raw massflow measurements were examined in further detail in Table 8. To verify the simulation was producing a physical solution, the massflow entering the plenum through the bleed hole and the massflow exiting the plenum through the boundary patch were recorded and large differences of up to 18.6% between the two massflows emerged.

Nominal Plenum Pressure Ratio	**Massflow In [Nondim]**	**Massflow Out [Nondim]**	**Percent Difference**
1.5	0.00173	0.00173	0.00%
1.05	0.00030	0.00025	18.33%
0.5	0.00017	0.00015	18.59%
0.25	0.00015	0.00017	8.52%

Table 8. Differences in the massflow in and out of the plenum, where nominal pressure ratio is the ratio between the plenum pressure and the freestream pressure.

Due to the discrepancies in the data, the complexity of the simulation, and the large number of design variables, the Slater model (Equation 87) was used to verify that the flow physics were accurately captured. A two-dimensional simulation of a flat plate in freestream flow was performed for simplicity.

4.2 Two-Dimensional Plenum Outflow Verification

The simulation was set up to replicate the computational efforts of Slater [30] with the exception that the current work was performed in two dimensions, whereas Slater's efforts were performed in three dimensions. Reducing the number of dimensions allowed the problem to be simplified and the simulations to be run faster. This setup was verified against both Slater's model and the experimental data of Willis et al. [40] by performing a grid resolution study to ensure the correct grid-independent massflow was obtained. A specified pressure boundary condition patch was applied on the aft side of the plenum wall to set the plenum pressure; however, a concern that an inappropriate patch size would affect the flow behavior in and around the bleed

hole led to a patch sizing study in conjunction with the grid resolution study.

Grid Resolution and Patch Sizing Study.

The study was first set up so that the incoming boundary layer profile matched the experimental installation and the boundary layer parameters: boundary layer thickness, momentum thickness, bleed hole diameter, bleed hole depth, and pressure ratios as shown in Table 9. To match the experiment, the computational mesh was divided into 3 main components: the plate grid, the hole grid, and the plenum grid as seen in Figure 10. The 3 grids were connected via point-to-point face matching, which does not require any interpolation between grids and eliminates overset errors, as small as they may be.

Flow Parameter	Value
Mach Number	2.46
Total Pressure	25.0 psia
Reynolds Number per Foot	5.15 million
Boundary Layer Thickness	0.5079 inches

Table 9. Boundary layer parameters from experiment [6].

To achieve the parameters in Table 9 within the simulation, the initial conditions and the plate length were set to produce the same boundary layer thickness and momentum thickness as the experiment at Mach 2.46 and a Reynolds number of 0.429 million.

The plate grid was set to a length of 43.46 inches and a height of 5.91 inches. The no-slip boundary condition was applied on the surface of the plate and the grid was extruded from the viscous wall using an initial wall spacing of 2.40×10^{-4} inches and a growth factor of 1.2. This was the wall spacing required to achieve a y^+ value of 1. The mesh was extruded at the specified growth factor until the cells reach an aspect ratio of 1, minimizing skew and maintaining uniformity in the regions of interest. The inflow was specified as supersonic inflow and the top and aft boundaries were set to

supersonic outflow. The bleed hole was set to a depth of 0.57 inches and a radius of 0.12 inches. Viscous wall boundary conditions were specified on the sides of the bleed holes, which were extruded from the wall using an initial wall spacing of 2.40×10^{-4} inches and a growth factor of 1.2.

In looking to measure the massflow through the bleed hole accurately, the experimental study drew air downward through the bottom of the plenum to minimize flow recirculation. The plenum for the current computational setup diverges from the experiment and instead drew the airflow through the aft wall of the plenum to resemble flow out of a suction pipe. The current plenum was modeled after the experimental design on which this simulation was based.

The plenum grid dimensions were 6.0 inches in length and 6.0 inches in height. A slip-wall boundary condition was applied on the top side of the plenum where the bleed hole was located and viscous wall boundary conditions were applied on the other three sides. The mesh was extruded from the viscous walls using an initial wall spacing of 2.40×10^{-3} inches, a factor of 10 larger than the bleed hole and plate grids, but used the same growth factor of 1.2. The outflow specified pressure boundary condition was applied over a limited range on the center of the aft plenum wall to model the suction pipes drawing air out of the plenum. The mesh topology is shown in Figure 10 and the grid dimensions are described in Table 10

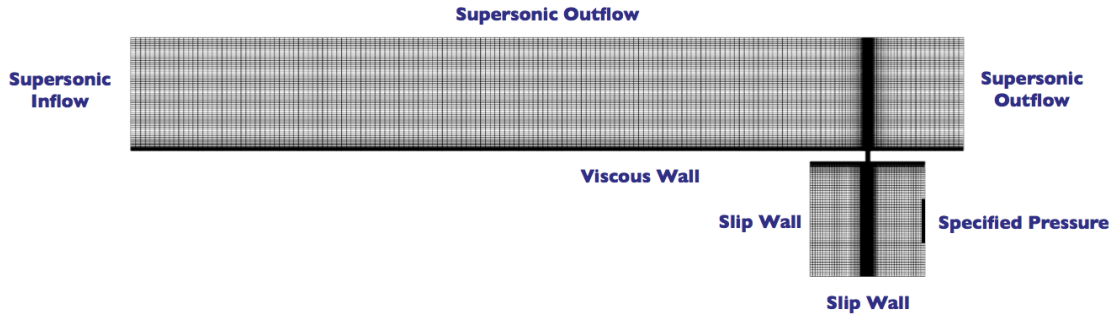

Figure 10. Grid spacing in the plenum with the patch sizing overlaid.

Parameter	Value
Tunnel Length	43.46 inches
Tunnel Height	5.91 inches
Tunnel and Hole Initial Wall Spacing	2.40×10^{-4} inches
Hole Depth	0.57 inches
Hole Radius	0.12 inches
Plenum Length	6 inches
Plenum Height	6 inches
Plenum Initial Wall Spacing	2.40×10^{-3} inches

Table 10. Mesh parameters and physical dimensions.

The grid resolution study was performed by varying the grid spacing between points as shown in Table 11. Every other grid point was removed to obtain the subsequent medium and coarse grids as visualized in Figure 11.

Grid	Number of Cells	Hole Spacing	Plenum Spacing	Tunnel Spacing
Coarse	63,123 cells	0.100 inches	0.250 inches	0.350 inches
Medium	73,332 cells	0.050 inches	0.125 inches	0.250 inches
Fine	103,203 cells	0.025 inches	0.075 inches	0.150 inches

Table 11. Mesh dimensions for the grid refinement study.

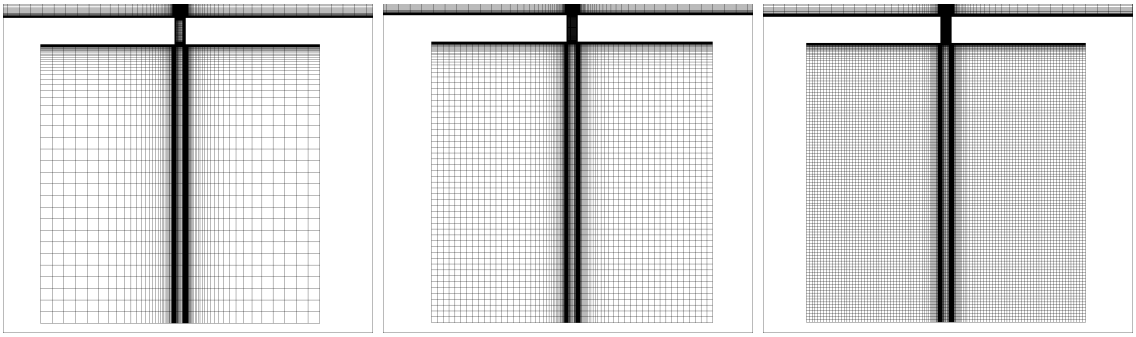

(a) Coarse mesh. **(b) Medium mesh.** **(c) Fine mesh.**

Figure 11. Mesh visualization of the three mesh refinement levels in the plenum.

The patch size was varied to examine its effect on flow recirculation in the plenum. The computational model replicated the wind tunnel model by applying a pressure boundary condition "patch" on a limited region of the plenum. The planned diameter of the suction tubing was used as the medium size patch and the dimensions were

doubled and halved to obtain the small and large sized patches, respectively. Patch sizes of 0.75, 1.50, and 3.00 inches were examined against each of the grid refinement levels. This resulted in 9 cases between the three refinement levels and patch sizes.

The simulations were performed using OVERFLOW with steady-state Reynolds-Averaged Navier-Stokes (RANS). A 3rd order Harten-Lax-van Leer-Contact (HLLC) upwind scheme was chosen as the inviscid flux algorithm, Implicit Symmetric Successive Over-Relaxation (SSOR) was chosen as the implicit solver, and Spalart-Allmaras (S-A) was selected as the turbulence model. The simulation parameters are summarized in Table 12.

Flow Parameter	**Value**
Mach Number	2.46
Temperature	386.0 °R
Reynolds Number per Foot	0.43 Million
Turbulence Model	Spalart-Allmaras
Inviscid Flux Scheme	HLLC Upwind
Implicit Solver	SSOR Algorithm

Table 12. Flow simulation parameters for the tunnel model in freestream air.

The simulations were run for 60,000 iterations to ensure the residuals dropped below 10^{-5} or 5 orders of magnitude. The incoming boundary layer was verified to match the parameters described in Table 9 and visualized with contours of Mach number in Figure 12.

The residuals are shown for the small patch at various grid resolutions in Figure 13, the medium patch at various grid resolutions in Figure 14, and the large patch at various grid resolutions in Figure 15. For the small patch, the residuals dropped further as the grid refinement increased with the highest residual dropping from 5 orders of magnitude to 7 orders of magnitude, suggesting that increased grid resolution results in a steady-state solution. Similar comparisons can be made for the medium patch but not so for the large patch. The large patch shows the largest decrease

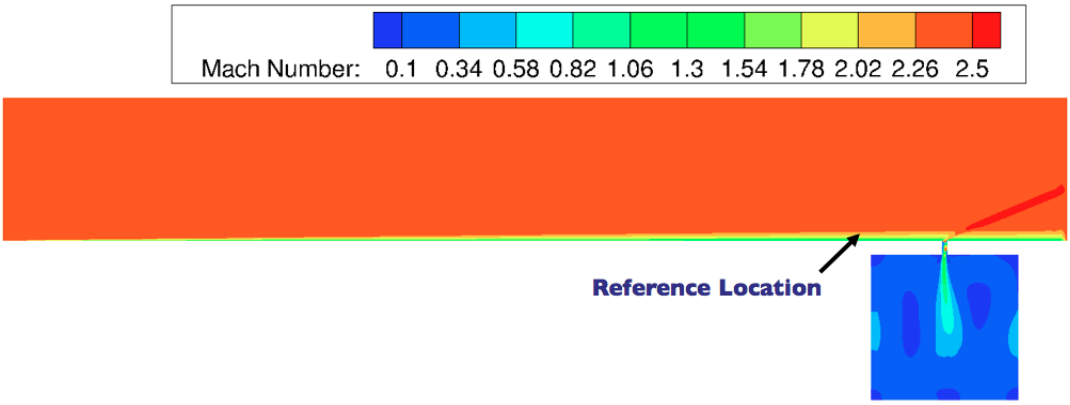

Figure 12. Verification of the computational simulation with experimental parameters.

in the residuals for any of the coarse meshes but shows the smallest decrease in the residuals for any of the fine meshes. The residuals with the large patch also exhibit some pseudo-steady oscillatory behavior, but could be the result of a time-resolution issue or the result of a physical phenomenon in the flow, such as recirculation.

The contours of u-velocity are overlaid with mesh visualization and streamlines to show the flow behavior with respect to both patch size and grid resolution in Figures 16-18. In the small and medium patches, the flow completely exits through the pressure boundary condition patch and recirculation occurs above the patch. In the large patch, the flow both enters and exits the plenum at the boundary condition patch. The streamline visualization show a recirculation bubble sitting right on the patch, causing the air to flow both in and out of the plenum.

The massflow was tracked every 200 iterations and at 5 different locations to verify massflow was conserved in and out of the plenum. The massflow was recorded in 3 locations within the bleed hole and in 2 locations at the plenum exit.

The massflow history for the small patch is shown in Figure 19, the medium patch in Figure 20, and the large patch in Figure 21. Upon observing the massflow at the 5 different locations, the expectation was the massflow would be approximately equal due to conservation of mass. However, the massflow rates recorded do not match well

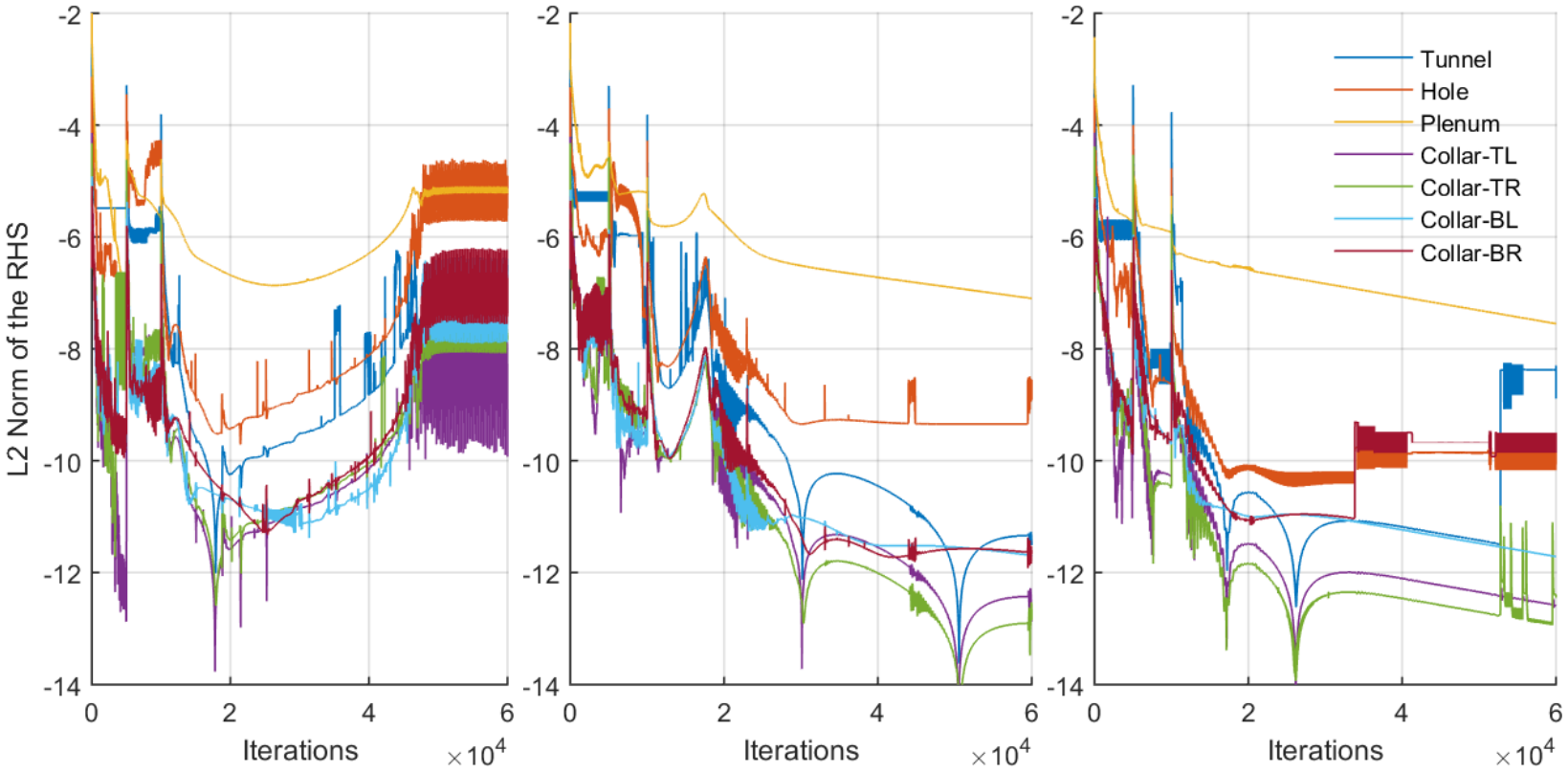

(a) Coarse grid refinement. (b) Medium grid refinement. (c) Fine grid refinement.

Figure 13. Residual history of the small specified pressure patch for various grid refinement levels.

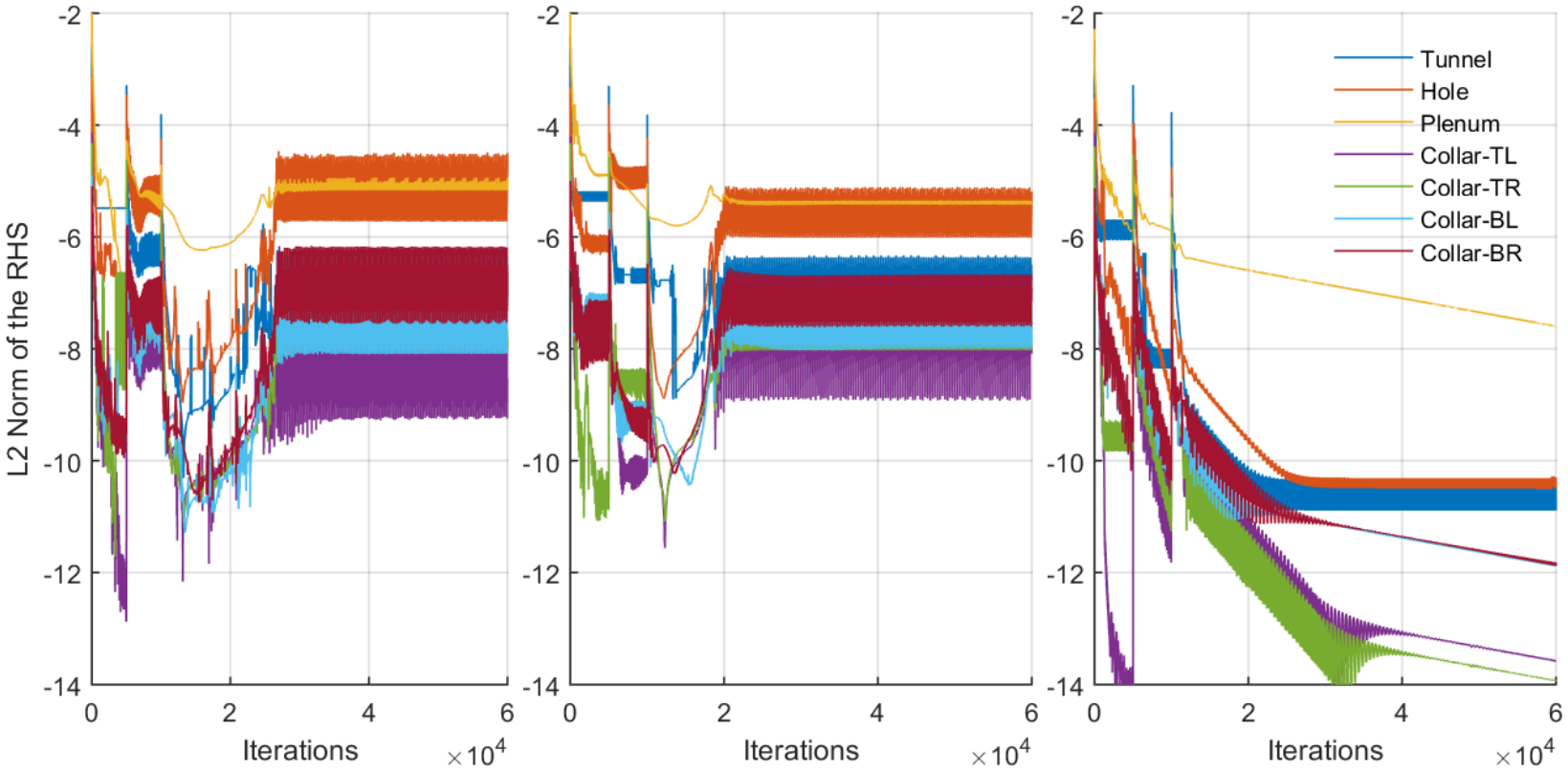

(a) Coarse grid refinement. (b) Medium grid refinement. (c) Fine grid refinement.

Figure 14. Residual history of the medium specified pressure patch for various grid refinement levels.

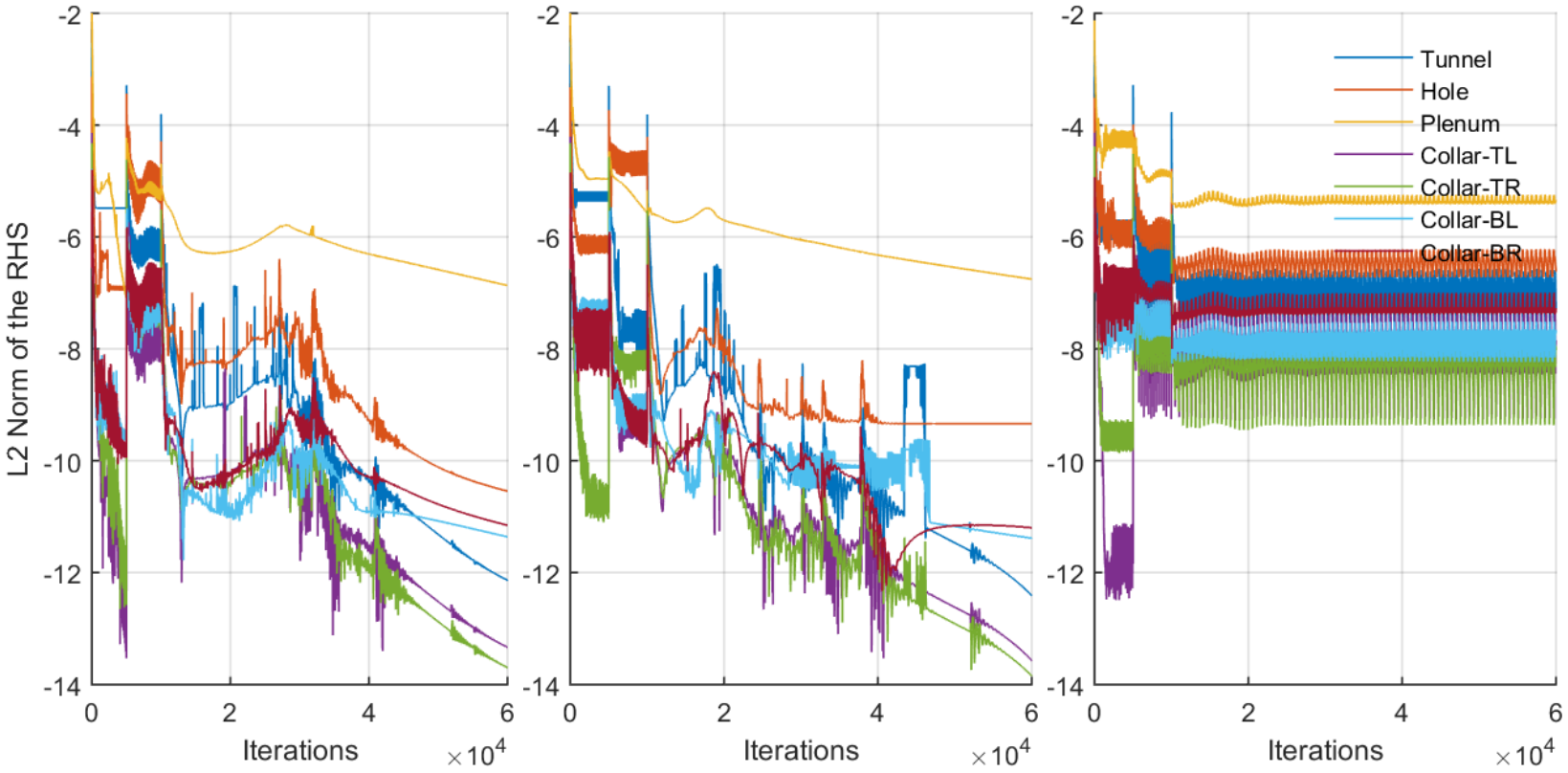

(a) Coarse grid refinement. (b) Medium grid refinement. (c) Fine grid refinement.

Figure 15. Residual history of the large specified pressure patch for various grid refinement levels.

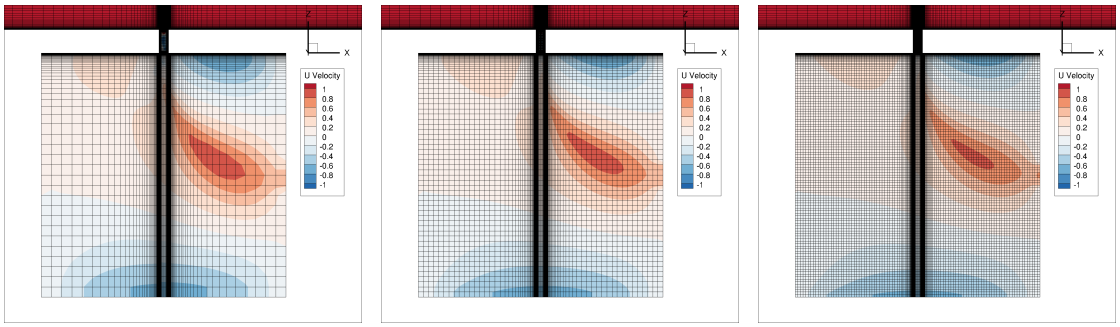

(a) Mesh visualizations for the coarse, medium, and large grids, respectively.

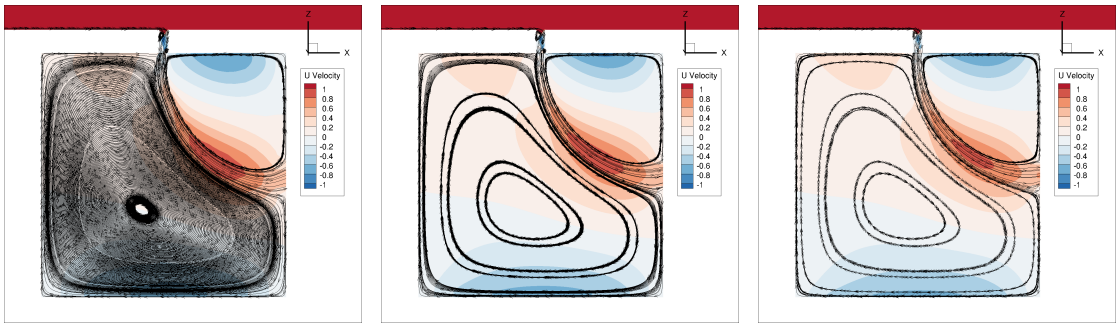

(b) Streamlines for the coarse, medium, and fine grids, respectively.

Figure 16. Contours of u-velocity and streamlines for the small patch.

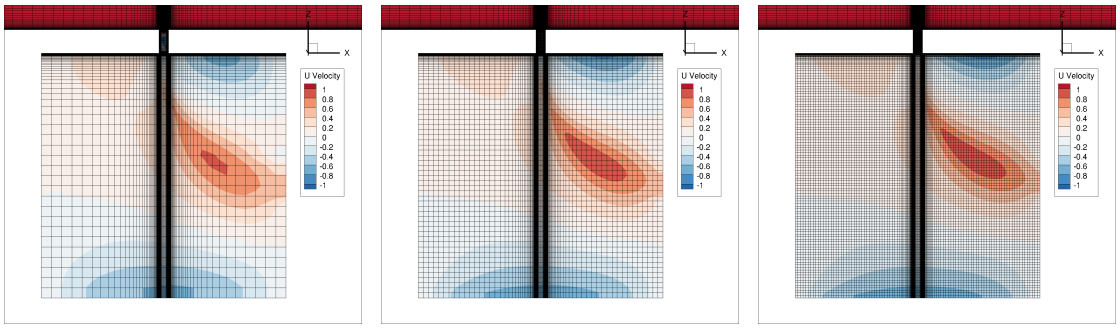

(a) Mesh visualizations for the coarse, medium, and fine grids, respectively.

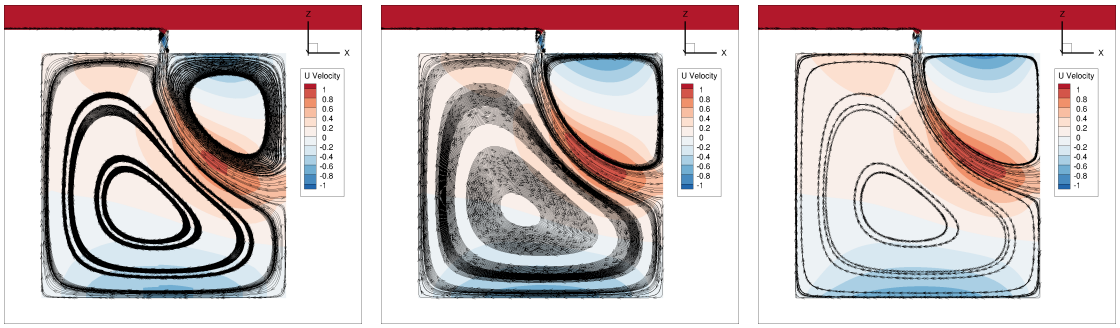

(b) Streamline visualizations for the coarse, medium, and fine grids.

Figure 17. Contours of u-velocity and streamlines for the medium patch.

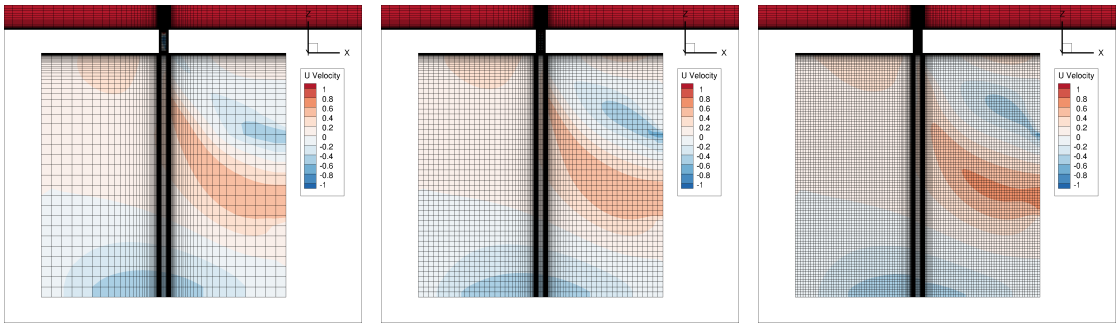

(a) Mesh visualizations for the coarse, medium, and fine grids, respectively.

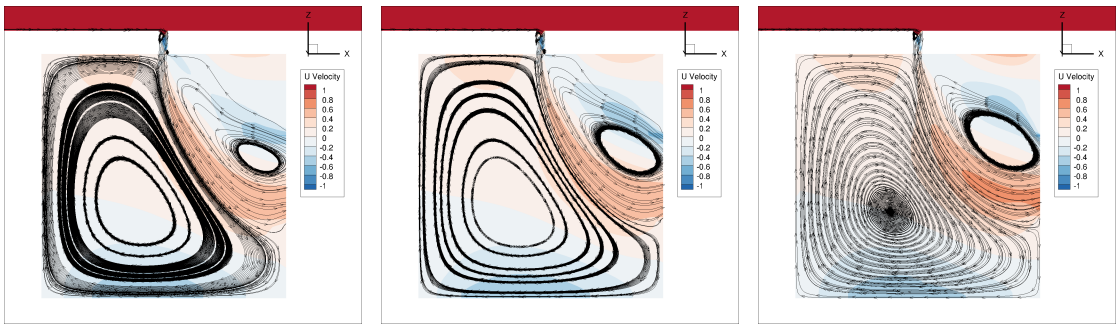

(b) Streamlines for the coarse, medium, and fine grids, respectively.

Figure 18. Contours of u-velocity and streamlines for the large patch.

with other measurements throughout the flow for many cases. The OVERFLOW source code was examined, various ways of applying the boundary condition were explored, and other boundary conditions were applied but the massflow results remain unchanged.

On closer observation, the massflow difference is exhibited more strongly between the plenum outflow measurements than the plenum inflow measurements. When comparing the inflow measurements to the mean incoming massflow rate, the difference is at worst 0.4% and at best 0.1% for the small patch as seen in Table 13. When comparing the outflow measurements to the mean outgoing massflow rate, this difference is at best 9.7% and at worst 14.8% for the small patch as seen in Table 14. This difference of the measurement against the mean is referred to as the spread or the accuracy of the measurement.

Of the 9 cases, 4 exhibited oscillatory behavior in the massflow: coarse grid and

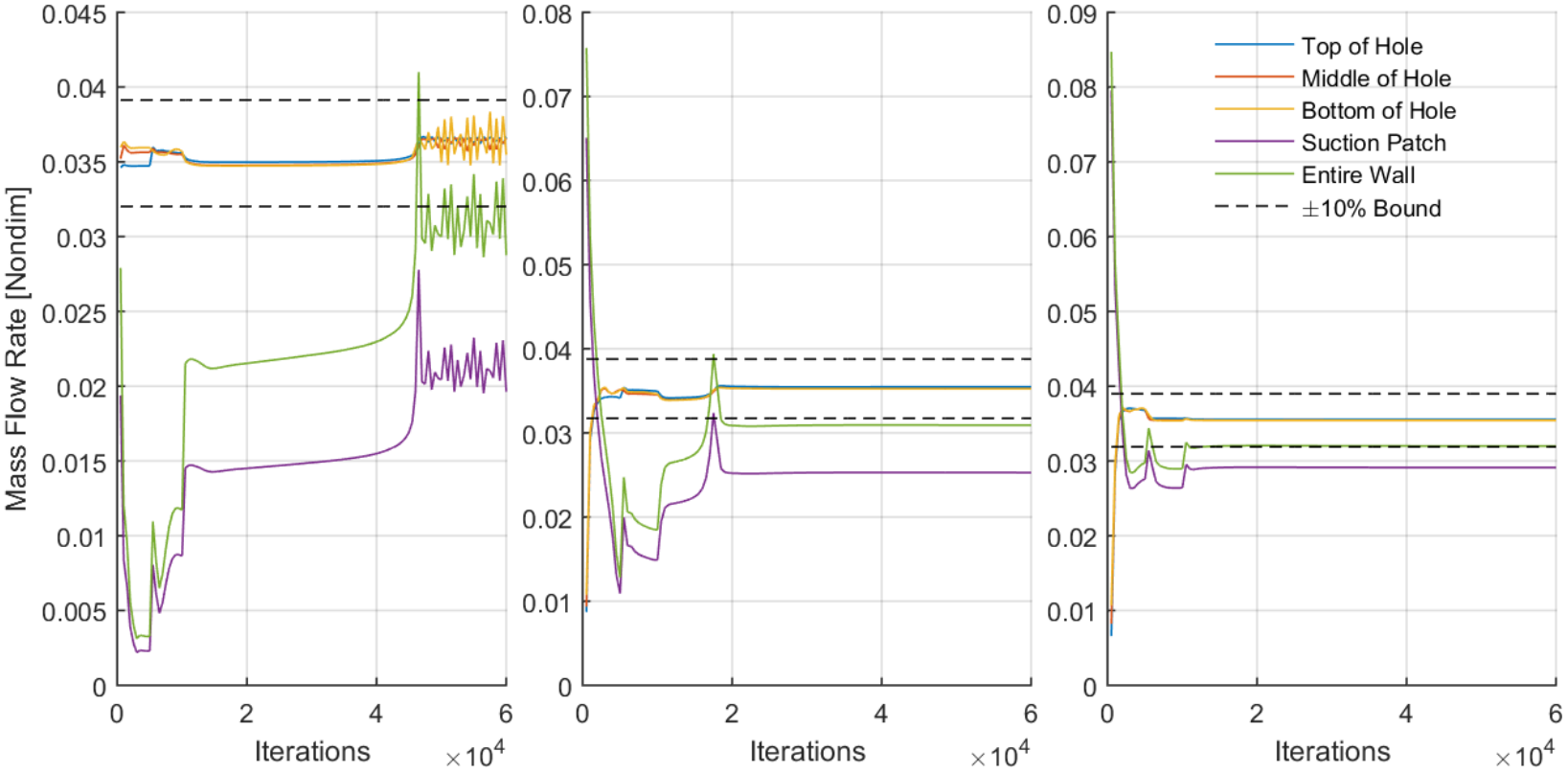

(a) Coarse grid refinement. (b) Medium grid refinement. (c) Fine grid refinement.

Figure 19. Massflow behavior with the small specified pressure patch at various points in the plenum for various grid refinement levels.

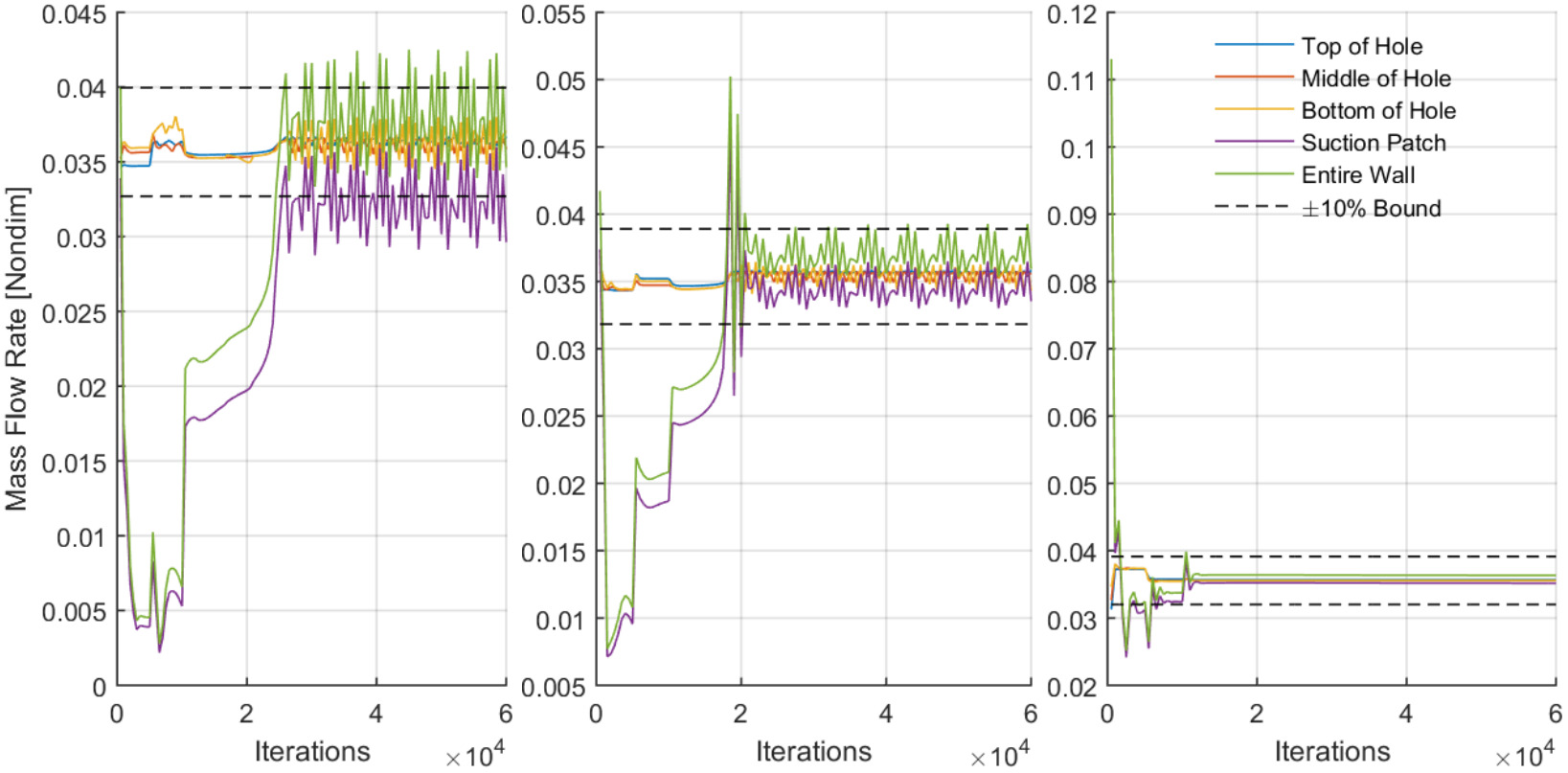

(a) Coarse grid refinement. (b) Medium grid refinement. (c) Fine grid refinement.

Figure 20. Massflow behavior with the medium specified pressure patch at various points in the plenum for various grid refinement levels.

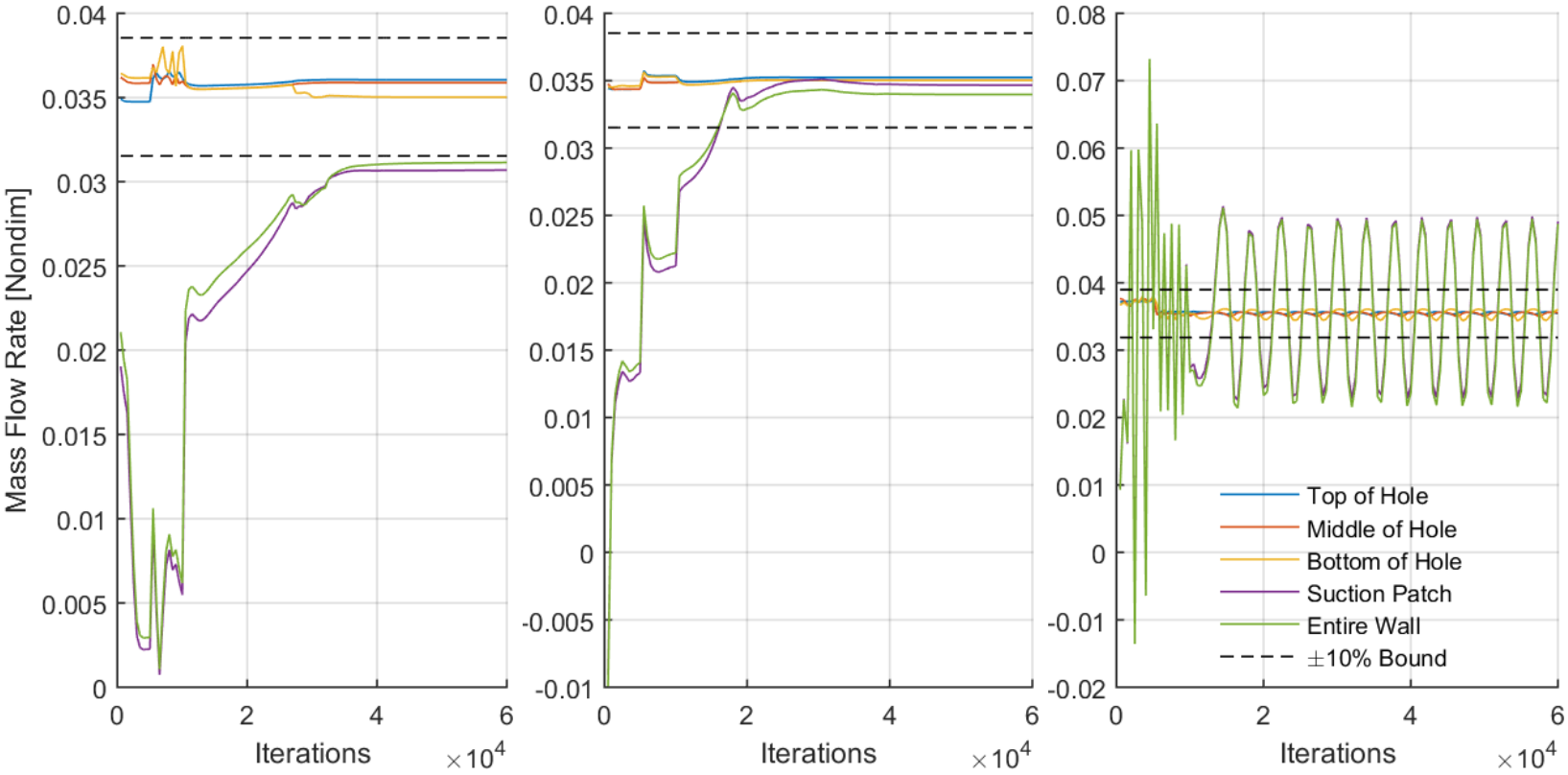

(a) Coarse grid refinement. (b) Medium grid refinement. (c) Fine grid refinement.

Figure 21. Massflow behavior with the large specified pressure patch at various points in the plenum for various grid refinement levels.

	Small Patch	Medium Patch	Large Patch
Coarse Grid	0.4%	2.5%	1.2%
Medium Grid	0.4%	0.2%	1.2%
Fine Grid	0.1%	0.3%	0.0%

Table 13. Percent difference of the steady-state inflow massflow rate coefficients in the plenum with the overall mean.

	Small Patch	Medium Patch	Large Patch
Coarse Grid	14.8%	3.4%	11.1%
Medium Grid	12.3%	4.6%	3.0%
Fine Grid	9.7%	2.2%	0.0%

Table 14. Percent difference of the steady-state outflow massflow rate coefficients in the plenum with the overall mean.

small patch, coarse grid and medium patch, medium grid and medium patch, and fine grid and large patch. The oscillatory behavior and the accuracy of the massflow do not appear to have any correlation. In fact, the large patch cases demonstrate extremely accurate results, especially at the fine grid resolution even though the massflow rates oscillate $\pm 8\%$ at the outflow. Though the massflow varies between two extremes, the average value correlates very well. The oscillatory behavior is not believed to be from the recirculation bubble on the boundary patch since the large patch on the coarse and medium grids do not exhibit the oscillatory behavior whereas the fine grid does. In addition, the visualizations from Figure 18 show recirculation on the boundary for all large patch cases.

A closer look at the flow structure within the bleed hole is shown in Figure 22 using streamlines, contours of Mach number, and contours of density gradient magnitude. The incoming flow encounters the 90-degree turn as it approaches the bleed hole. The flow is not physically capable of turning the full 90-degrees due to the large momentum of the flow. Isentropic relations dictate a maximum turn angle the flow can experience, creating a free shear layer separating the incoming supersonic flow and a recirculation bubble on the upstream side of the bleed hole. The aft side of the

bleed hole forces the incoming supersonic flow to form an impact shock that allowed the flow to become subsonic, turn, and expand downward into the bleed hole. The pressure recovers behind the impact shock, creating a larger pressure gradient at that point in the flow and the plenum pressure. This forces the flow through the bleed hole and causes the flow to accelerate through the bleed hole. Supersonic regions in the bleed hole develop that form shocks when interacting with the recirculation bubble creating a shock structure similar to a shock train in jet flow. This shock train exhibits steady and stationless behavior when the massflow history is steady and exhibits an unsteady, circular behavior when the massflow history is unsteady.

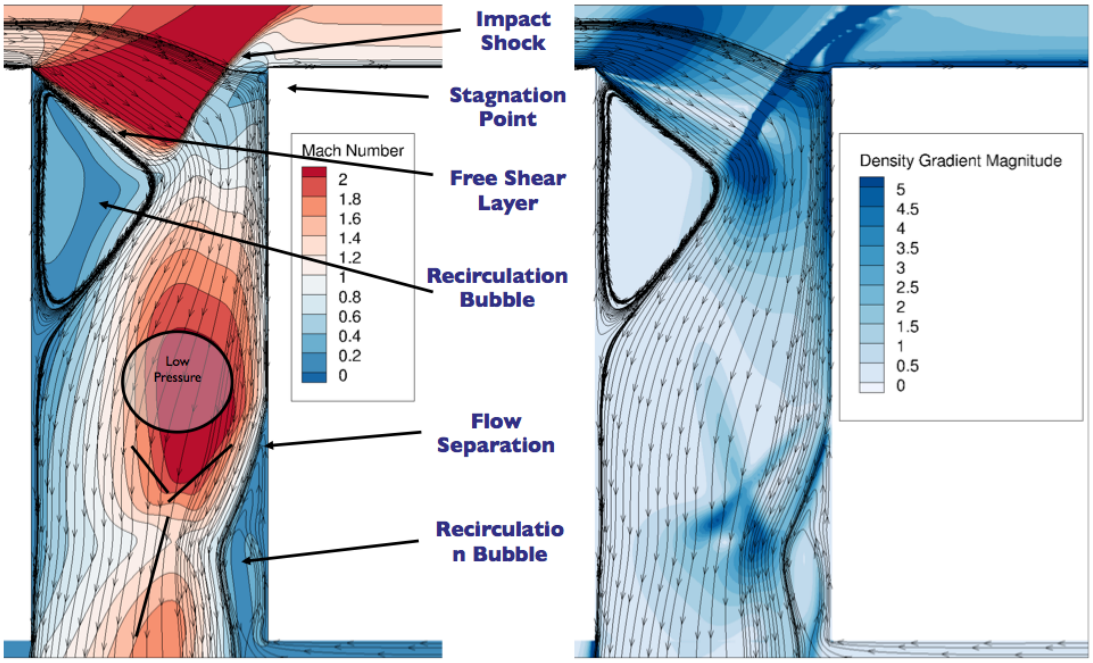

Figure 22. Key features of the flow structure within the bleed hole.

The results from Figures 19-21 and Tables 13 and 14 are color-coordinated and summarized in Table 15, where red-colored cells represent a difference greater than 10% between plenum outflow and plenum inflow, yellow-colored cells represent a difference of 10% or less between plenum outflow and plenum inflow, and green-colored cells represent a difference of less than 3% between plenum outflow and plenum inflow.

The qualitative steady-state or oscillatory behaviors observed in Figures 19-21 are used to describe each of the cases as either or unsteady in Table 15.

Mass Flow Coefficient Behavior		Patch		
		Small	**Medium**	**Large**
Grid	**Coarse**	Unsteady	Unsteady	Steady
	Medium	Steady	Unsteady	Steady
	Fine	Steady	Steady	Unsteady

Green – 3% mass flow difference and under
Yellow – 10% mass flow difference and under
Red – Over 10% mass flow difference

Table 15. The qualitative oscillatory behavior and accuracy of massflow rates as a function of mesh refinement and patch sizing summarized.

The results of the grid resolution study and the patch size study in Figures 16-18 show that using a pressure boundary condition produced recirculation on the boundary for the large patch. This recirculation phenomenon on the boundary is not believed to be physical but more importantly, is undesirable since boundary conditions were not designed for flow interaction. Table 15 shows that the medium patch at the fine grid resolution performed the best result in producing both the most accurate solution and the most steady solution. The medium patch, fine grid resolution case is recommended for accurate and steady measurements of massflow through the bleed hole. The accuracy of the boundary condition flow physics is explored further by comparing results with physical ducting.

Specified Pressure Boundary Condition Comparison with Physical Ducting.

In internal flows, boundary conditions are usually set so that information propagates in one direction, either in or out of the boundary. Boundaries that have flow that both enter and exit the computational domain raise concerns since the flow conditions are fixed on that boundary and exert a constraining force on the flow properties that do not necessarily reflect the physics of the flow.

The boundary condition was placed on the aft wall of the plenum to provide a realistic flow path based on both the wind tunnel model design and from the simulations with small, medium, and large patches. The previous results showed some recirculation on the boundary patch in Figures 16-18 so a physical duct was modeled to investigate how realistic recirculation to occur directly on the boundary condition.

The small, medium, and large patches were extended 3 inches and the boundary condition placed where the duct terminated. This was to model the physical suction piping that would exist in drawing out the flow. The same flow conditions were applied to the simulation and the same specified plenum pressures were applied to the boundary condition at the outflow face of the piping. The duct walls were run with both inviscid and viscous walls for the small (Figure 23), medium (Figure 25), and large (Figure 27) ducts. The cases were all run at a pressure ratio of 0.25 using the fine mesh resolution.

Recalling from Table 14, the small patch was not accurate, having at best a 9.7% outflow difference, unsteady flow with the coarse mesh, but steady flow with the medium and fine mesh. Figure 16 showed that none of the three grid refinement levels showed any recirculation on the boundary condition patch. Adding the duct corroborated the results from Figure 16 as the flow did not set up any recirculation near the duct inflow, as seen in Figure 23. There were more similarities between the

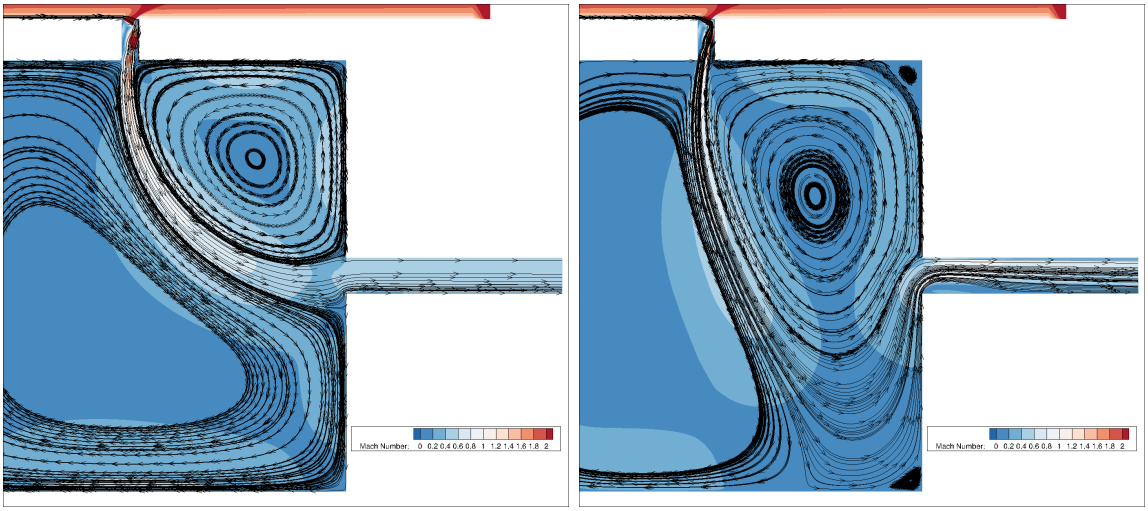

(a) Inviscid plenum wall results. **(b) Viscous plenum wall results.**

Figure 23. Contours of Mach number and streamlines of both slip and no-slip plenum walls using the small-width duct.

patch and the inviscid run in Figure 23a due to the same wall boundary conditions suggesting a viscous boundary condition allowed for damping and the pair of counter-rotating recirculation bubbles forced the flow further downward, which in turn meant the flow had to correct further upward to reach the duct. A recirculation bubble formed just inside the mouth of the duct, but the net effect was unchanged in that the flow is directed in one direction at the duct inlet, the same as the patch results.

A similar conclusion is reached when examining the massflow history results from Figure 24. Figure 24a shows an outflow difference of approximately 3% for the inviscid walls and Figure 24b shows an outflow difference of less than 1% for the viscous walls.

Recalling once more from Table 14, the medium patch had overall more accurate results than the small patch with an outflow difference of 4.6% at worst and 2.2% at best, however, both the coarse and medium mesh refinements showed unsteady flow behavior. Figure 17 showed that none of the three grid refinement levels showed any recirculation on the boundary condition patch. Adding the duct corroborated the results from Figure 17 as the flow did not set up any recirculation near the duct

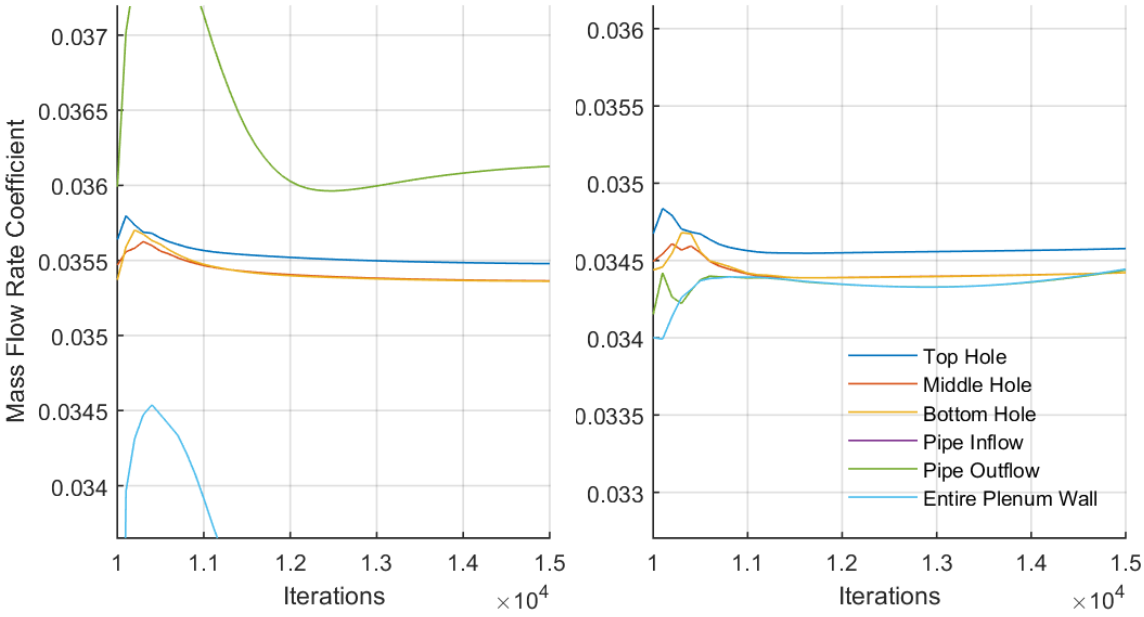

(a) Inviscid plenum wall results. (b) Viscous plenum wall results.

Figure 24. Massflow behavior of the small-width duct at a pressure ratio of 0.25.

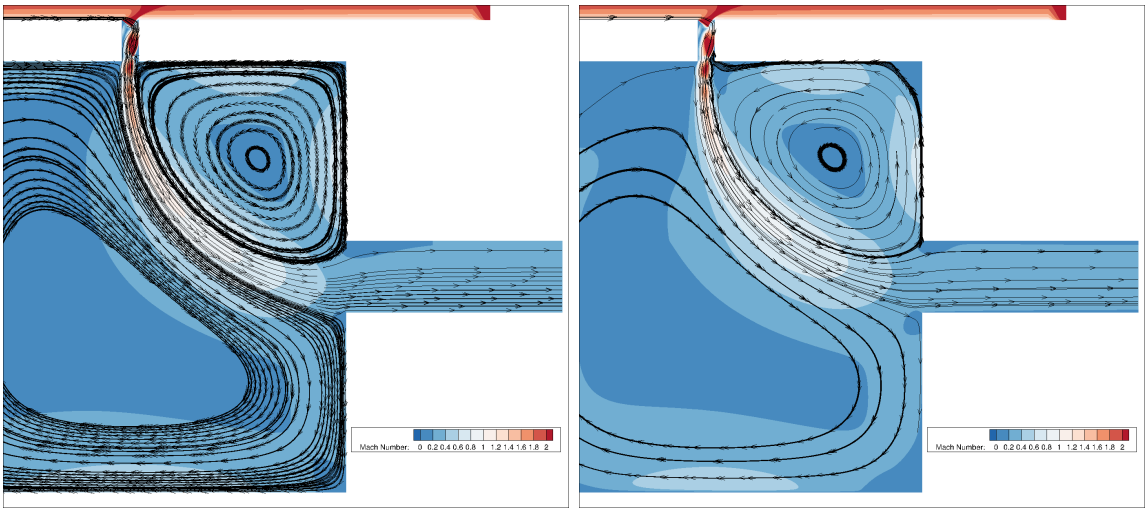

(a) Inviscid plenum wall results. (b) Viscous plenum wall results.

Figure 25. Contours of Mach number and streamlines of both slip and no-slip plenum walls using the medium-width duct.

inflow, as seen in Figure 25. There were more similarities between the patch and the inviscid run in Figure 23a than the patch and the viscous run due to the same inviscid wall boundary conditions. The viscous case developed a pair of counter-rotating recirculation bubbles again, just like the small duct case. Also unlike the small duct case, a recirculation bubble did not form just inside the duct inlet, and again, the net effect was unchanged in that the flow is directed in one direction at the duct inlet, the same as the patch results.

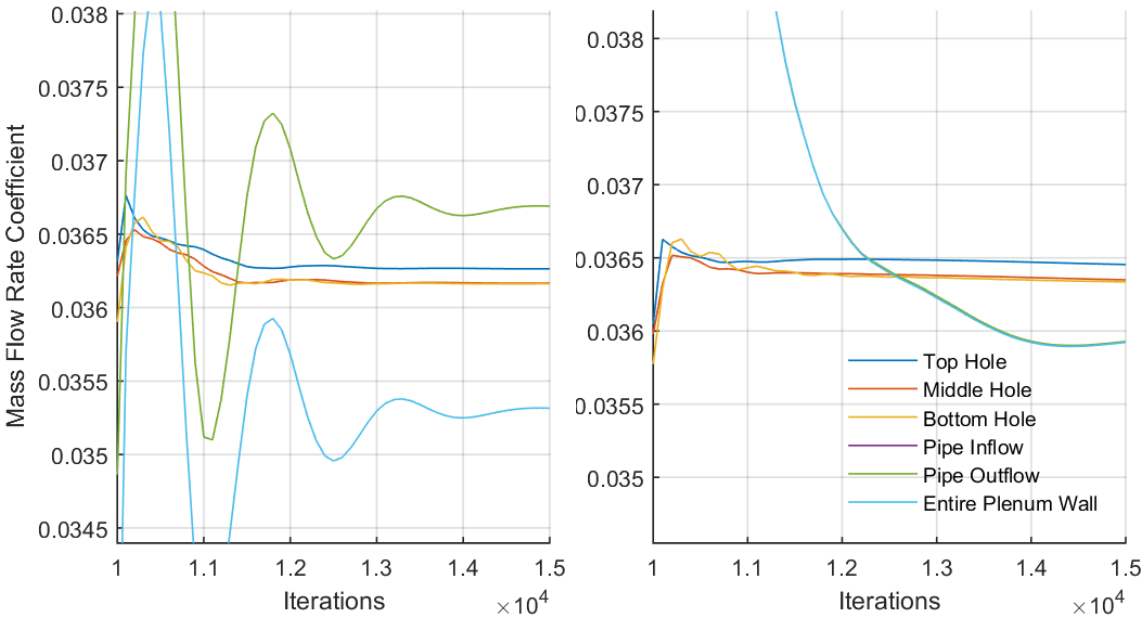

(a) Inviscid plenum wall results. **(b) Viscous plenum wall results.**

Figure 26. Massflow behavior of the medium-width duct at a pressure ratio of 0.25.

Upon examination of the massflow history results in Figure 26, the massflow exiting the duct had a difference of 4% and 3% for the inviscid and viscous cases, respectively. The oscillations seen in Figure 26a between 5,000 and 10,000 iterations were due to the startup iterations to set up the flow. These results line up well with the inviscid patch results.

Referring back to Table 14, the large patch exhibited the best overall accuracy with an outflow difference of 11.1% at worst and 0.0% at best. The large patch,

however, produced an interesting result in that the massflow behavior was unsteady at the best accuracy with the fine mesh refinement, suggesting that the unsteady behavior might have contributed to the high degree of accuracy in the physics of the solution. Figure 18 showed a recirculation bubble on the boundary condition for all mesh refinement levels and the ducting results in Figure 27 show that a recirculation bubble on the boundary could be a physical phenomenon. The other behavior that wasn't seen in the previous ducting sizes was that both the inviscid and viscous walls showed a pair of recirculation bubbles in the top right corner of the plenum, suggesting that with the large duct size, the flow velocities are slow enough to overcome the damping of the viscous walls. Figure 27 shows that the recirculation bubble on the patch boundary condition could be a physical flow feature, though there is still outflow on the specified pressure boundary condition at the end of the duct. Extending the duct further until the flow only goes out of the computational domain could bring more confidence to the solution, but the current simulation was acceptable due to the fact that the recirculation bubbles did not sit on the boundary condition but lay upstream of the duct inflow.

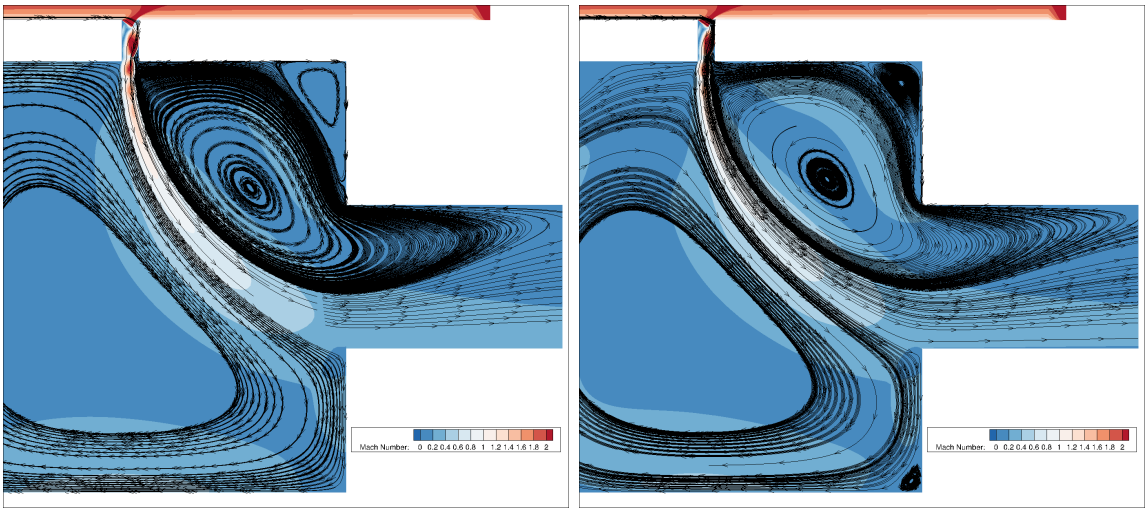

(a) Inviscid plenum wall results. **(b) Viscous plenum wall results.**

Figure 27. Contours of Mach number and streamlines of both slip and no-slip plenum walls using the large-width duct.

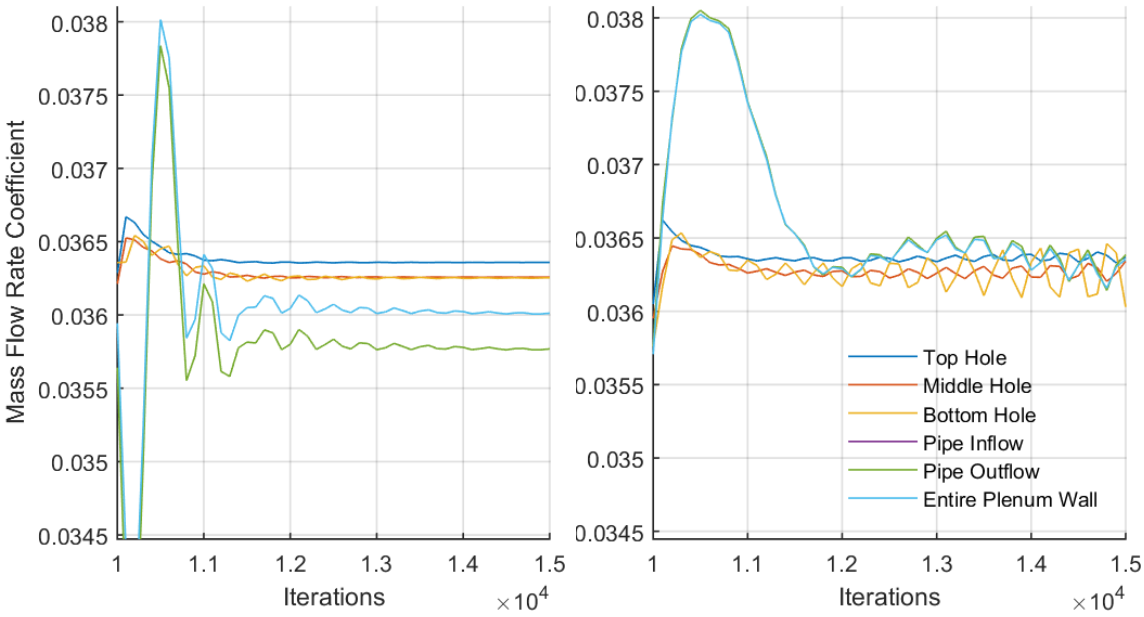

(a) Inviscid plenum wall results. **(b) Viscous plenum wall results.**

Figure 28. Massflow behavior of the large-width duct at a pressure ratio of 0.25.

Figure 28 shows the massflow history results of the large duct for both the inviscid and viscid walls. The inviscid walls produced an outflow percent difference of 3%, which was greater than the large patch case. The viscous walls exhibited the best accuracy at 0%. These results seemed to suggest that the accuracy exhibited by the large patch and the large duct might not be due to the recirculation bubble, but rather due to the larger area the large patch and duct provided. The recirculation suggests that the areas were actually too large, which was why some flow entered the domain to restrict the "effective" area. The Mach numbers from both Figures 18 and 27 suggest the overall flow velocity was lower compared to the other cases.

To see if the massflow from using the large duct fell within reason compared to Slater's correlation, the simulations were run at plenum pressure ratios of 0.50, 0.75, and 1.00 using the inviscid wall. The four pressure ratios are shown in Figure 29.

The simulations that used both the patch boundary condition and duct show that recirculation in the plenum is inevitable. For a wind tunnel model, this is realistic

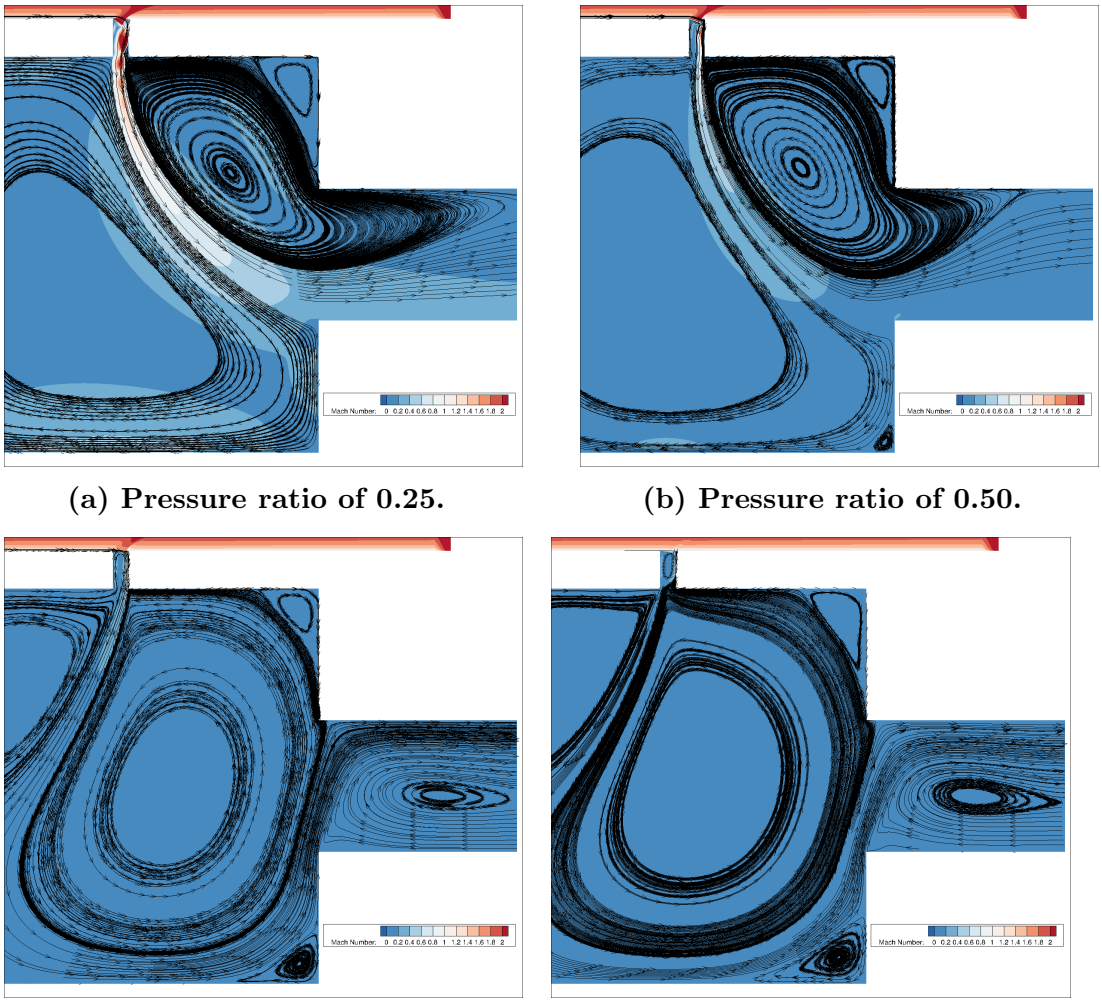

(a) Pressure ratio of 0.25.

(b) Pressure ratio of 0.50.

(c) Pressure ratio of 0.75.

(d) Pressure ratio of 1.00.

Figure 29. Contours of Mach number and streamlines of the large-width inviscid duct for various plenum pressure ratios.

and for cases with multiple holes, the recirculation will affect the flow interaction between holes. The recirculation seems to play a large role in the flow structure within the plenum but because both steady and unsteady behaviors have produced accurate results, removing the effect of recirculation was explored.

Removing Boundary Condition Effects with Complete Suction.

The fine grid from the grid resolution and patch sizing study was used and the specified pressure boundary was applied on the two adjacent and one opposing sides. The flow parameters were maintained the same as previously, setting up the complete suction case with boundary condition on all sides with the slip walls maintained on the top wall with the bleed hole. The streamlines and Mach number contours for a plenum pressure ratio of 0.25 is shown in Figure 30.

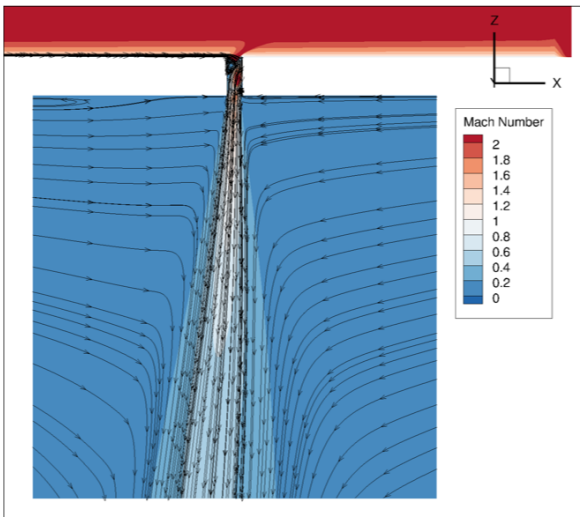

Figure 30. Streamlines and Mach number contours for the complete plenum suction simulation.

The pressure at the plenum exit was varied to obtain 4 different pressure ratios and plotted against Slater's empirical relationship of experimental data Equation 87 as shown in Figure 31. The trends are similar but the data points do not lie on top of Slater's curve. This is most likely due to the fact that this simulation was performed in

two dimensions, which would not accurately predict massflow of a three-dimensional hole.

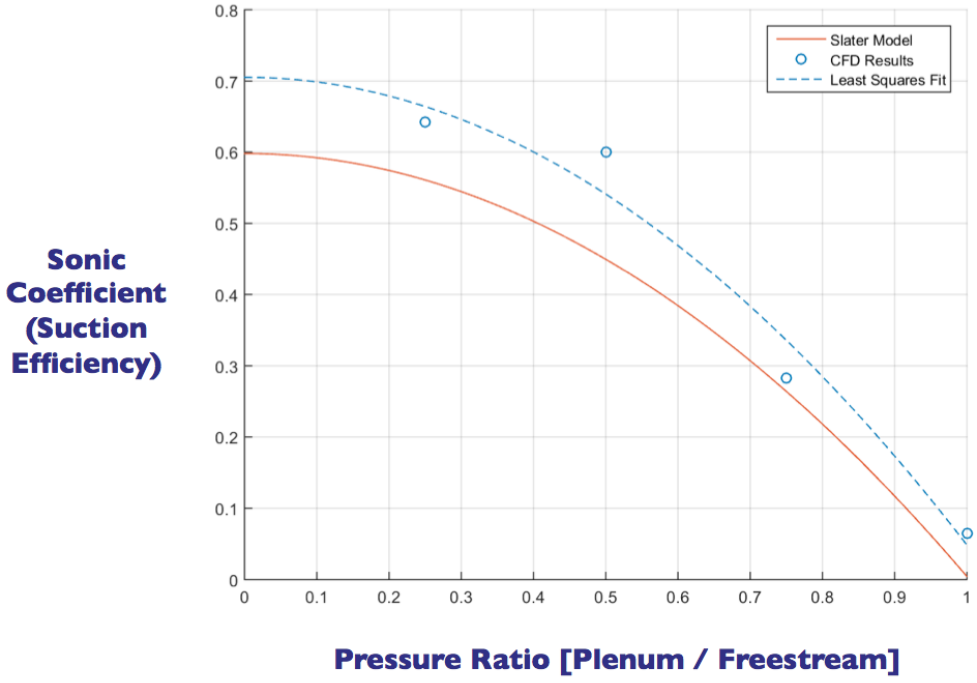

Figure 31. Sonic coefficient plot of the two-dimensional simulation using complete suction compared to the Slater model.

The massflow rate through the hole entering the plenum for different configurations were compared with each other in Table 16. The massflows are all very consistent with one another and the case with the fine grid with large patch agree well with the fine grid with complete suction. This is a good indicator that even though the fine grid with large patch has an oscillating recirculation bubble resting on the boundary condition, this configuration produces the data closest to the fine grid with complete suction configuration and thus the best configuration at removing plenum effect. The same is shown for massflow exiting the plenum in Table 17.

The results are summarized in Table 18. The complete suction simulations are all steady since drawing flow in all directions prevent a recirculation bubble from forming and the accuracy is very good, even for coarser meshes.

	Small Patch	Medium Patch	Large Patch	Complete Suction
Coarse Grid	0.4%	2.5%	1.2%	0.8%
Medium Grid	0.4%	0.2%	1.2%	1.5%
Fine Grid	0.1%	0.3%	0.0%	0.0%

Table 16. Percent difference of the steady-state inflow massflow rate coefficients in the plenum with the overall mean compared with complete suction.

	Small Patch	Medium Patch	Large Patch	Complete Suction
Coarse Grid	14.8%	3.4%	11.1%	2.0%
Medium Grid	12.3%	4.6%	3.0%	1.8%
Fine Grid	9.7%	2.2%	0.0%	1.5%

Table 17. Percent difference of the steady-state outflow massflow rate coefficients in the plenum with the overall mean compared with complete suction.

Mass Flow Coefficient Behavior		Patch			Complete
		Small	**Medium**	**Large**	
Grid	**Coarse**	Unsteady	Unsteady	Steady	Steady
	Medium	Steady	Unsteady	Steady	Steady
	Fine	Steady	Steady	Unsteady	Steady

Green – 3% mass flow difference and under
Yellow – 10% mass flow difference and under
Red – Over 10% mass flow difference

Table 18. The qualitative oscillatory behavior and accuracy of massflow rates as a function of mesh refinement and patch sizing with the results from complete suction summarized.

4.3 Shock Unsteadiness Characterization

In order to determine potential mitigation strategies for unsteady shocks, the unsteady shock was first characterized. The forward-facing step was chosen as a canonical model that would introduce enough disturbance to the flow to create SWBLI and in turn, an unsteady shock. The aim was to find the correct flow solver and mesh parameters that would produce the unsteady shock. Then, pressure measurements over time were used to produce a Fast-Fourier Transform (FFT) and the frequency content of the signal was analyzed.

Determining the Correct Mesh Topology and Flow Parameters.

To properly model the forward-facing step, the tunnel was assembled with a 4 grid system. The first grid captured the boundary layer off the tunnel floor to the top of the tunnel and extended from the tunnel inflow boundary condition to the front edge of the forward-facing step. The second grid overlapped with the first grid to add a viscous mesh to the forward-facing step. The third grid had a viscous mesh that added overlap with the first two grids and defined the topology of the top of the forward-facing step. A fourth grid was added in an approximate position to provide refinement upstream of the forward-facing step so that the shock disturbance was amply refined.

The tunnel initial wall spacing was set at 0.00024 inches and the final coarse spacing was set at 0.25 inches. A growth factor of 1.2 was used. The tunnel extended 5.91 inches from the tunnel floor and was 3.0 inches in width. The forward-facing step was placed 13 inches downstream of the inflow boundary condition. The refined regions used a constant spacing of 0.25 in all three coordinate directions. The step was 1 inch high and extended 5 inches from the upstream edge to the outflow boundary condition. The parameters are summarized in Table 19.

Grid Parameter	Value
Tunnel Height	5.91 inches
Tunnel Width	3.0 inches
Tunnel Length	16.0 inches
Initial Wall Spacing	0.00024 inches
Refined Spacing	0.05 inches
Coarse Spacing	0.25 inches
Growth Factor	1.2
Step Height	0.5 inches
Step Length	3.0 inches
Step Position	13.0 inches

Table 19. Mesh dimensions for the four grid system modeling the forward-facing step.

The overset grid system was run at Mach 1.5, a temperature of 385 degrees Rankine, a Reynolds number of 2.5 million per foot, and with the SA turbulence model. The conditions are shown in Table 20.

Flow Parameter	Value
Mach Number	1.5
Temperature	385.0 °R
Reynolds Number per Foot	2.5 million
Turbulence Model	SA

Table 20. Flow parameters for the forward-facing step.

The inflow was set to supersonic inflow, the wall surfaces were set to viscous adiabatic wall with pressure extrapolation, span-wise periodic, the outflow was set to supersonic extrapolation, and the top of the tunnel was set to adiabatic slip-wall. The result is shown in Figure 32.

The solution was run for 10,000 iterations to ensure the residuals were reduced by at least 5 orders of magnitude. From the mesh visualization in Figure 32, the fourth grid that was meant to provide refinement at the shock was not properly placed as the shock clearly originates further upstream from the refinement region. The flow visualization over time illustrated a very stable shock.

The forward-facing step was suspected to be too small to cause a large enough

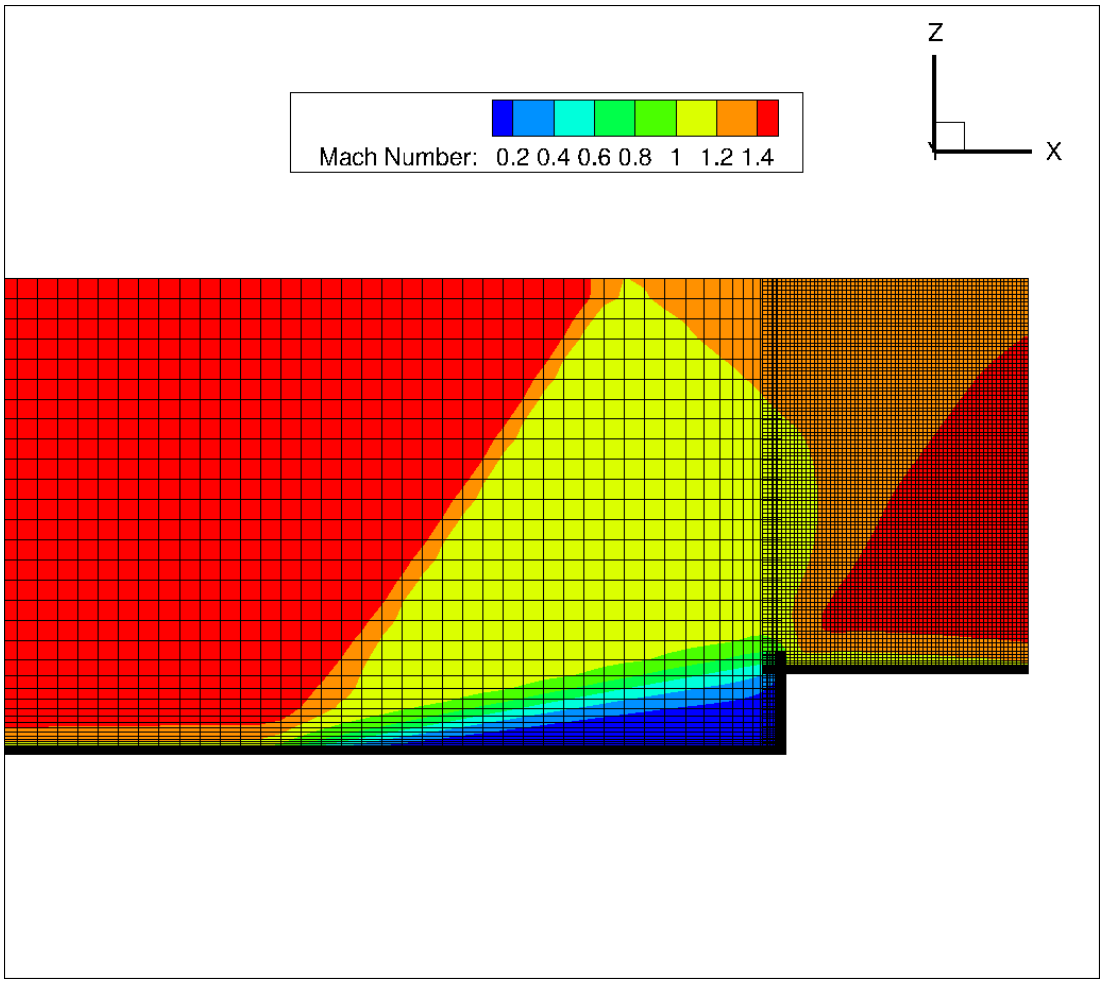

Figure 32. Mach number contour using the SA turbulence model.

disturbance with the RANS model. It would be advantageous to demonstrate shock oscillation with a RANS model primarily for its cheap computing cost, so the step height was increased from 0.5 inches to 1.0 inches. The shock also reflects off the top boundary and interacted with the expansion wave around the forward-facing step. The tunnel height was increased to decrease the interaction between the two waves and the top boundary condition was switched from slip-wall to supersonic outflow. The new grid topology was created and run using the same flow solver settings and is illustrated in Figure 33.

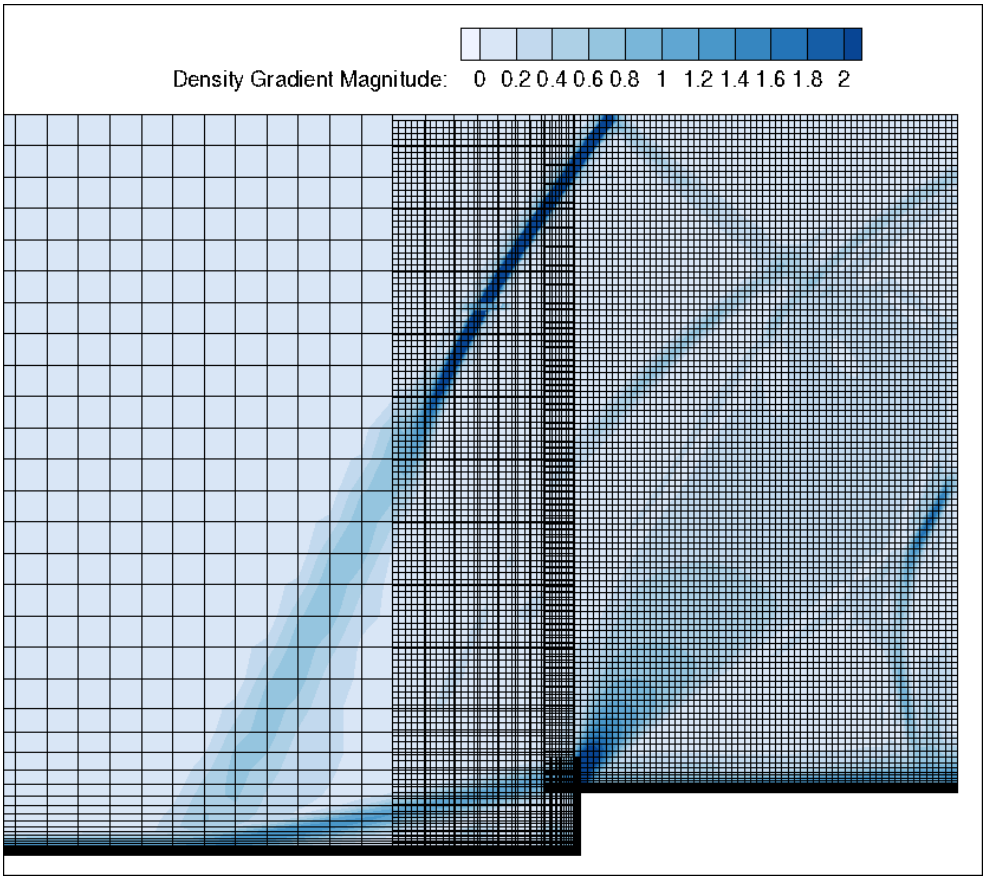

Figure 33. Inadequately resolved shock structure using DES.

The shock was not adequately refined so the refinement mesh was expanded 12 step heights further upstream as shown in Figure 34 and was run using DES, but the solution did not reach a converged state most likely due to the lack of three-

dimensional turbulence relief.

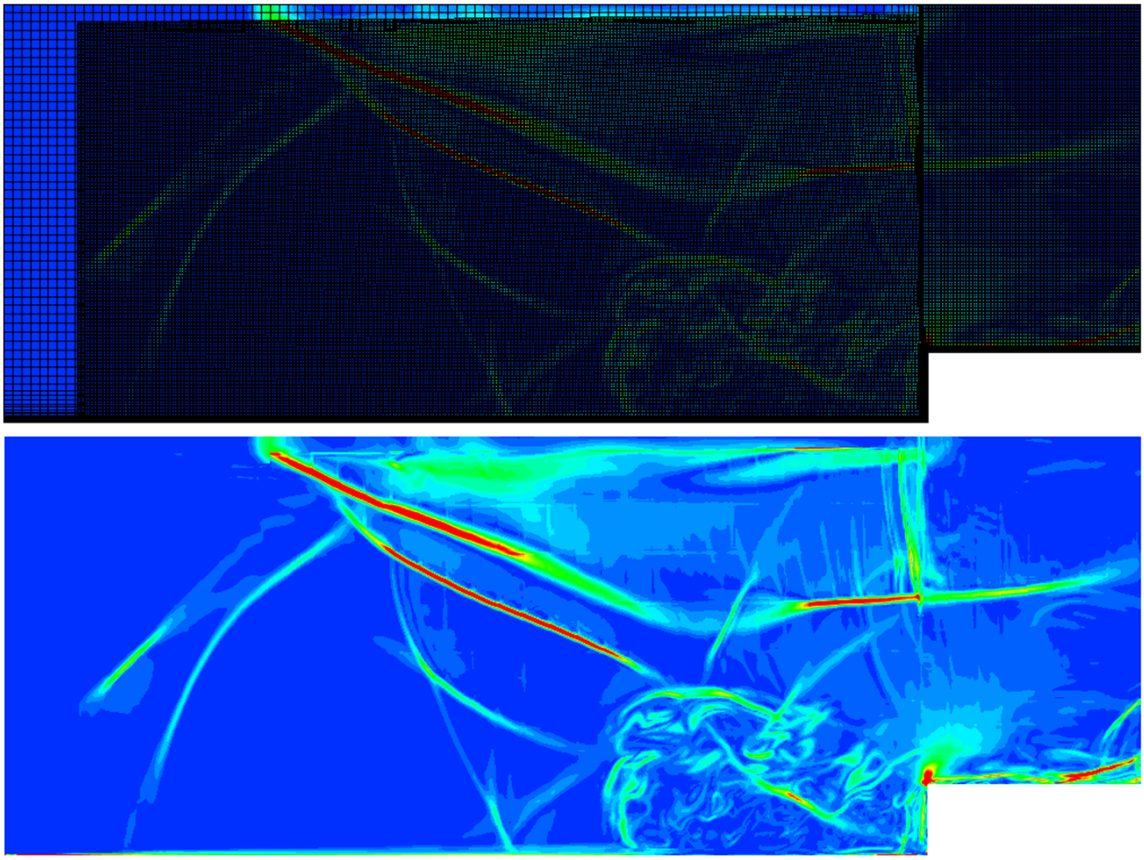

Figure 34. Non-physical simulation using DES due to lack of span-wise three-dimensional turbulence relief.

Analysis of Shock Unsteadiness.

A new, 7-grid system was developed that would minimize overset interpolation error by enforcing point-to-point matching to the maximum extent. The refinement areas were also reduced to only the necessary regions to decrease the number of cells. Three "background" grids defined the tunnel upstream and downstream of the step and the stream-facing portion of the step. Two more grids defined the leading and vertical edges of the step. Three point-to-point matched "refinement" grids provided a refined region that adequately resolved the shock.

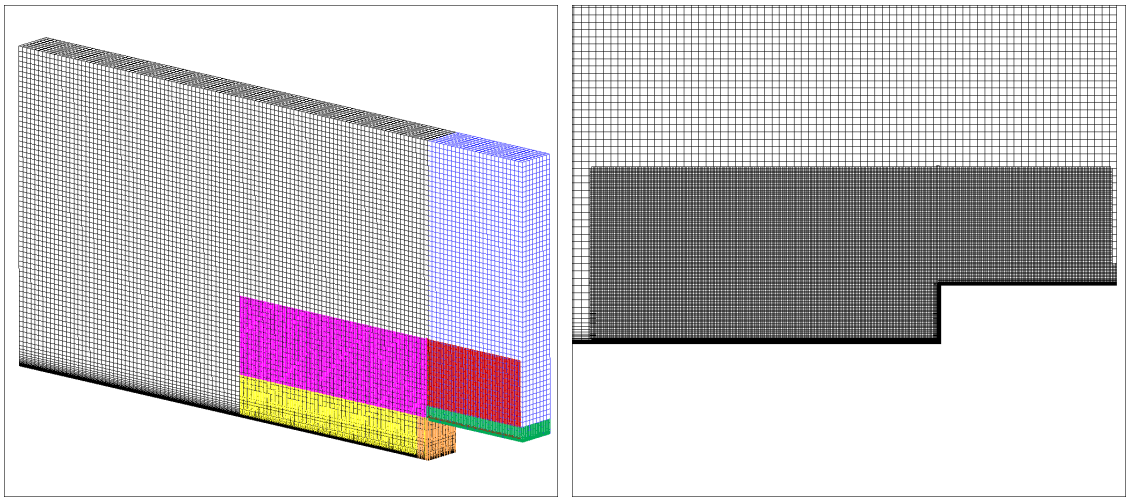

Figure 35. Grid refinement system around the forward-facing step.

The mesh was initialized with 5,000 iterations using the RANS SA turbulence model. Then DES was turned on for another 20,000 iterations to produce the solution shown in Figure 36.

The shock oscillations were observed, verifying that these solutions were viable candidates for shock characterization. Five points, 1 inch apart around the base of the shock were chosen to record time-varying pressure measurements every 50 iterations at the tunnel centerplane of $y = 0$. The solver input file was configured to output slices of the solution at the tunnel centerline and a Fortran code was written to extract the pressure measurements at the desired location.

The time history was collected long enough to provide adequate resolution in the frequency domain as shown in Figure 38. The frequency content showed approximately 5 major peaks at 20, 42, 108, 154, and 190 Hz. The higher frequencies could be higher modes of the lower frequencies, indicating a common source for the signals at different frequencies.

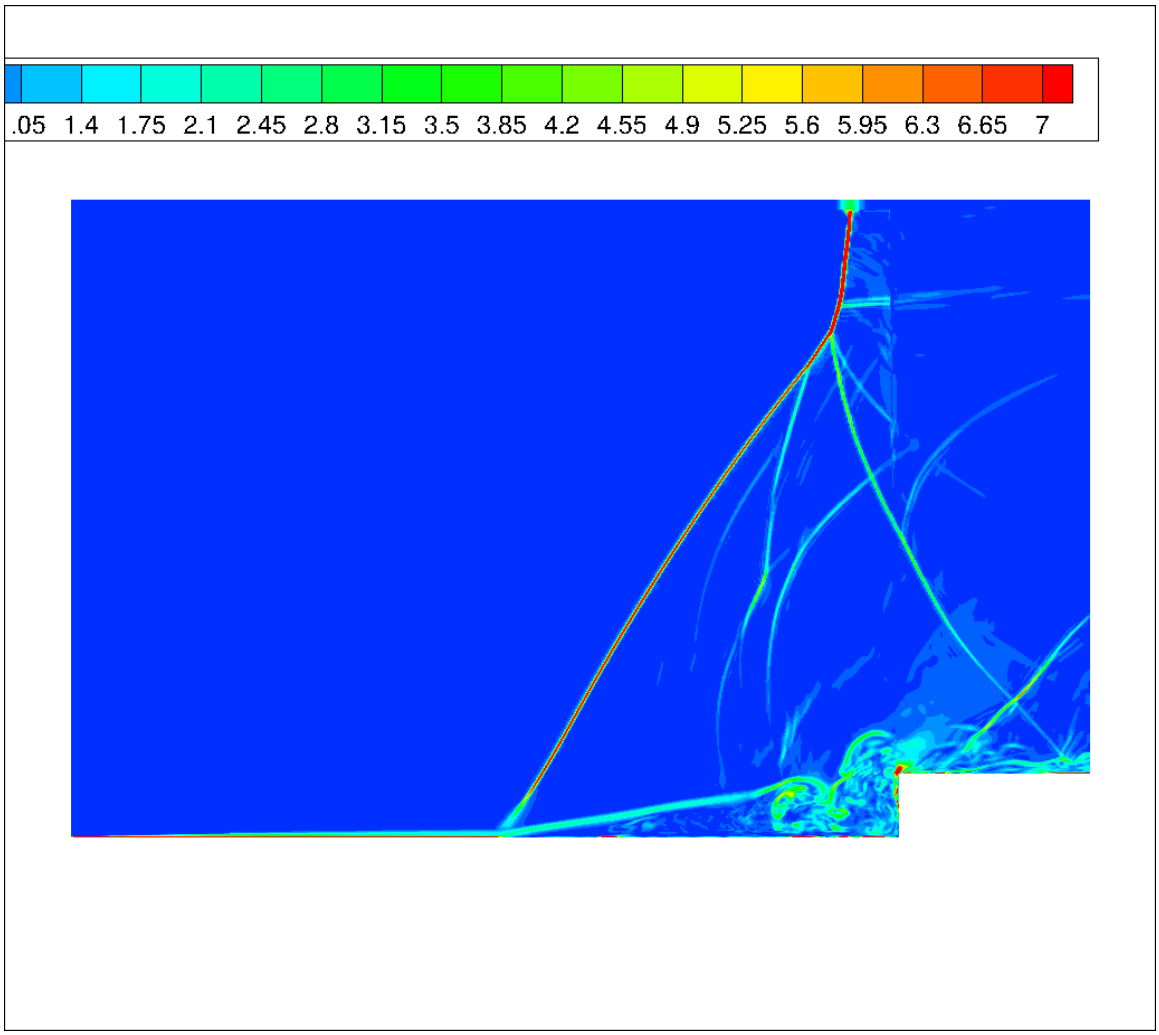

Figure 36. Simulation of an adequately resolved DES shock structure.

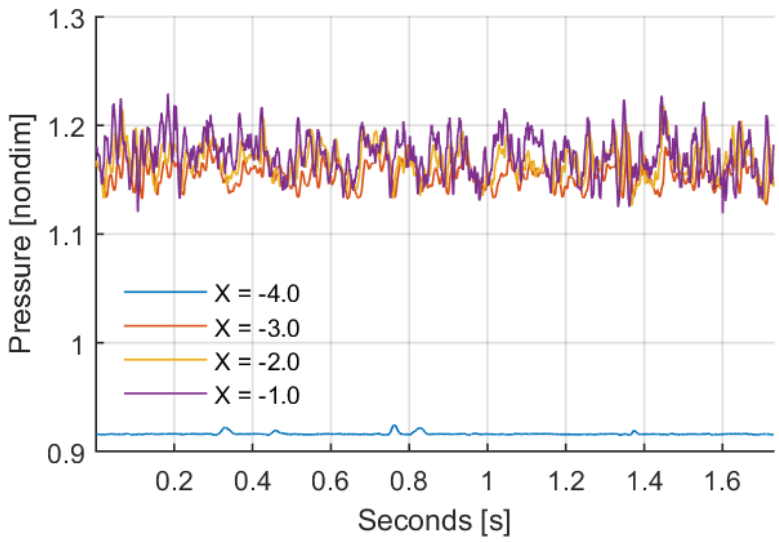

Figure 37. Time history of pressure at locations 1 inch apart 0.5 inches above the surface.

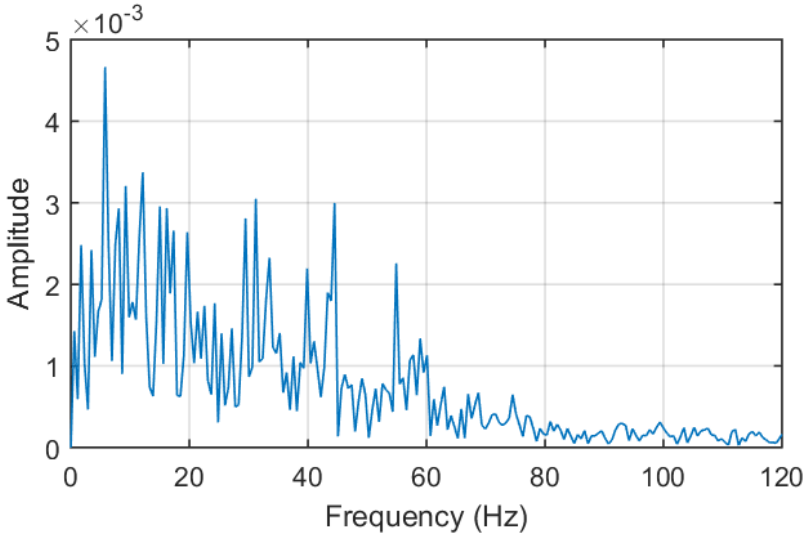

Figure 38. FFT displaying frequency content of the pressure time history.

V. Conclusion

The objective of this research was to use CFD to demonstrate the effect of bleed holes on shock unsteadiness. This research built on the canonical configuration of a forward-facing step for shock unsteadiness mitigation.

The results demonstrate that the mechanism in which air is pulled from the plenum must be considered to obtain higher quality data that is consistent with mass conservation. Appropriately sizing the flow out of the plenum can diminish the plenum effect so that other flow effects can be isolated and studied in greater depth. Initially, a massflow discrepency of 14.8% was measured but a successful grid-independent solution was successfully reached that reduced the discrepency to 0%. Comparisons to experimental data using complete suction show the computational data is accurate to within 0.05%. The flow physics of using plenum boundary conditions were verified with ducting models with an accuracy of 2%. The two-dimensional simulation matched empirical, three-dimensional trends, but a higher-fidelity, three-dimensional computational model is needed to improve accuracy. An unsteady shock was successfully produced using a forward-facing step and was characterized to have peak frequencies at 5.8, 12.1, 31.2, 44.5, and 54.9 hertz. The higher frequencies are hypothesized to be higher modes and therefore the result of a common phenomenon.

In conclusion, this work developed flow and grid methodologies for flow analysis and shock characterization including FFT analysis and best practices for accurate massflow measurements. Insight into bleed flow physics was developed, paving the way for powerful shock mitigation tools.

Future work will involve implementing bleed holes in the forward-facing step problem and analyzing the frequency content of the pressure time histories. Reduction in frequency peaks would indicate a decrease in shock strength and leftward shifts in frequency would indicate increase in shock stability. The goal will be to demonstrate

successful shock mitigation and show the dependence with bleed hole design factors such as diameter, depth, and number of holes.

Appendix

A. Source Code

1.1 MATLAB Slater Calculations

```
clear; clc

cfd_data = [0.06426610978520282, 0;
0.01234706612824018, 0.033328964613368275;
0.020639722925144748, 0.032726081258191334;
0.030300589308001013, 0.029370904325032757;
0.03995199360644611, 0.019672346002621237;
0.05008252345189351, 0.011179554390563555];

efd_data = [0.012059673783939639, 0.03431230564964155;
0.036603710755445454, 0.026207981542455107;
0.044666540641628574, 0.01732076575657504;
0.04942177224024738, 0.013153210701277056;
0.054141503427901666, 0.0090231261087112;
0.06044960025569479, 0.004426562696064985;
0.06465393794749408, 0;
0.04269634998138862, 0.01948885976408912;
0.04040359308970683, 0.022424639580602892;
0.038616588519754635, 0.0244167758846658;
0.03319403216170311, 0.029134993446920047;
0.028692895147592882, 0.031572739187418083;
0.025352740250925116, 0.032332896461336844];

mach = 2.46;
gamma = 1.4;
factor = (1+(gamma-1)*mach^2/2)^(gamma/(gamma-1));

plen_ratio_unscaled = 0:0.0025:0.07;
plen_ratio_scaled = plen_ratio_unscaled*factor;
slater_model_scaled = -0.59361420*plen_ratio_scaled.^2 + ...
    0.03069346*plen_ratio_scaled + 0.59799735;
slater_model_unscaled = slater_model_scaled/factor;

slater_model_mod = -0.57*plen_ratio_scaled.^2 + 0.59799735;

figure(1); clf; hold on
plot(plen_ratio_scaled,slater_model_scaled,'k')
scatter(efd_data(:,1)*factor,efd_data(:,2)*factor,'square','filled...
    ')
```

```
scatter(cfd_data(:,1)*factor,cfd_data(:,2)*factor,'^','filled')

grid on
lgd = legend('Slater Model','Data','CFD','Location','Best');
lgd.Box = 'off';
xlim([0,1.2])
ylim([0,0.6])
ylabel('Surface Sonic Flow Coefficient')
xlabel('Plenum Static Pressure Ratio')

x0=10;
y0=10;
width=300;
height=200;
set(gcf,'units','points','position',[x0,y0,width,height])
```

1.2 TCL Code

```
#!/usr/bin/bash

# ================================ Initialize parameters.

if { [info exists env(SCRIPTLIB)] } {
   lappend auto_path $env(SCRIPTLIB)
} else {
   puts stderr "\n ERROR: use 'setenv SCRIPTLIB' to define the ...
      location of"
   puts stderr "        the Tcl library routines from Chimera Grid...
       Tools.\n"
   exit 1
}

if { [info exists env(CGTBINDIR)] } {
   InitExecs
} else {
   puts stderr "\n ERROR: use 'setenv CGTBINDIR' to define the ...
      location of"
   puts stderr "        the Chimera Grid Tools executables.\n"
   exit 1
}

# ================================ directories

set Par(rootdir) [pwd]
set Par(crvdir) $Par(rootdir)/curves
set Par(srfdir) $Par(rootdir)/surfaces
set Par(voldir) $Par(rootdir)/volumes
set Par(inpdir) $Par(rootdir)/inputs
set Par(xdir)   $Par(rootdir)/X_DIR

# ================================ constants
set pi 3.14159265359
```

```
set rad_deg [expr {$pi/180.}]

# ...
   ------------------------------------------------------------------------...

# ------------------------------------------------------ function ...
   definitions
# ...
   ------------------------------------------------------------------------...


# Obtain a temporary folder name
proc Get_Temp {} {
  set rootdir [pwd]
  set tempdir temp.[pid].[incr ::globalCounter]
  set workdir [file join $rootdir temp_folder $tempdir]
#  puts $tempdir
#  puts $workdir
  #puts $workdir
#  after 5000
  exec mkdir -p $workdir

  cd $workdir
  return $workdir
}

# ------------------------------------------------------ ...
   ExtrudeSurface
proc ExtrudeSurface { ifile ofile crv_path } {
  # ofile is plot3d multigrid file
  # ifile must be plot3d multigrid file

  set tmpdir Extrude_Surf
  exec mkdir -p $tmpdir


  # get the number of points to extrude
  set npSpan [GetTotalNp $crv_path]

  # initialize the sliceFiles list which will contain all the surf...
      grid names to
  # concatenate into volume grid
  set sliceFiles [list $ifile]

  # get 1st point from span file
  set xyz1 [GetXyz $crv_path 1 1 1 1]

  # copy and translate ifile to every point on the span file
  for {set j 2} {$j <= $npSpan} {incr j} {
    # get delta xyz to move this plane
    set xyz2 [GetXyz $crv_path $j 1 1 1]
    set dx [expr {[lindex $xyz2 0] - [lindex $xyz1 0]}]
```

```
      set dy [expr {[lindex $xyz2 1] - [lindex $xyz1 1]}]
      set dz [expr {[lindex $xyz2 2] - [lindex $xyz1 2]}]

      GedTranslate $ifile $tmpdir/ifile.$j $dx $dy $dz
      lappend sliceFiles $tmpdir/ifile.$j
    }

    ConcatGridsn $sliceFiles $ofile l 0

    exec rm -rf $tmpdir

}

# ------------------------------------------------ ...
   MakeGeomCurve
proc MakeGeomCurve {iws fws gf_guess x1 y1 z1 x2 y2 z2 ofile} {
  # does not strictly enforce gf

  set debug 0
  set output 1
  set dir Geom_Curve
  exec mkdir -p $dir

  set span [Dist $x1 $y1 $z1 $x2 $y2 $z2]
  set max_diff 10.

  if {$debug == 1} {puts "span: $span iws: $iws fws: $fws ...
     gf_guess: $gf_guess"
    puts "span, a, np, gf, fws"}

  set aa [expr {floor($span*0.9999/$fws)}]

  for {set i 0} {$i <= $aa} {incr i} {
    set a [expr {$span-$i*$fws}]

    set somelist [FindNPGF $iws $fws $a $gf_guess]
    set np [lindex $somelist 0]
    set gf [lindex $somelist 1]
    set ffws [expr {$iws*pow($gf,$np-2)}]

    if {$debug == 1} {puts "$span, $a, $np, $gf, $ffws"}

    if {abs($ffws - $fws) < $max_diff} {
      set max_diff [expr {abs($ffws - $fws)}]
      set ideal_np $np
      set ideal_gf $gf
      set ideal_fws $ffws
      set ideal_L $a
      set ideal_seg $i
    }

  }
```

```
128   if {$debug == 1} {
        puts "ideal np:  $ideal_np"
        puts "ideal gf:  $ideal_gf"
        puts "ideal fws: $ideal_fws"
        puts "ideal L:   $ideal_L"
133     puts "ideal seg: $ideal_seg" }

      # L is length of growing region
      # seg is number of segments in constant region

138   if {$output == 1} {
        puts "\nMakeGeomCurve: "
        puts "  growth factor specified:  $gf_guess"
        puts "  using a growth factor of: $ideal_gf"
        puts "  final wall spacing spec:  $fws"
143     if {$ideal_seg == 0} {
          puts "  using a final spacing of: $ideal_fws\n"
        } else {
          puts "  using a final spacing of: $fws\n"
        }
148   }

      set theta_x [expr {asin(($x2-$x1)/$span)}]
      set theta_y [expr {asin(($y2-$y1)/$span)}]
      set theta_z [expr {asin(($z2-$z1)/$span)}]
153
      if {$debug == 1} {puts "\n start growing"}

      set sum 0.
      set grids [list ]
158
      set x_1 $x1
      set y_1 $y1
      set z_1 $z1

163   if {$ideal_seg == 0} {
        set ideal_np [expr {$ideal_np -1}]
      }

      # make the growing portion a
168   for {set i 1} {$i < $ideal_np} {incr i} {
        set growing [expr {pow($ideal_gf,$i-1)}]
        set spacing [expr {$growing*$iws}]
        set sum [expr {$sum + $spacing}]

173

        set x_2 [expr {$spacing*sin($theta_x)+$x_1 }]
        set y_2 [expr {$spacing*sin($theta_y)+$y_1}]
        set z_2 [expr {$spacing*sin($theta_z)+$z_1}]

178     if {$debug == 1} {puts "$x_1, $y_1, $z_1 | $x_2, $y_2, $z_2"}
```

```
      CreateLinexyz $dir/a$i.crv $x_1 $y_1 $z_1 $x_2 $y_2 $z_2
      lappend grids $dir/a$i.crv

      set x_1 $x_2
      set y_1 $y_2
      set z_1 $z_2
    }


    if {$ideal_seg == 0.} {

      if {$debug == 1} {puts "\n no constant region... ending"}
      CreateLinexyz $dir/a$i.crv $x_1 $y_1 $z_1 $x2 $y2 $z2
      lappend grids $dir/a$i.crv
      if {$debug == 1} {puts "$x_1, $y_1, $z_1 | $x2, $y2, $z2"}

    } else {
      if {$debug == 1} {puts "\n start constant"}
      set seg_diff [expr {($span-$ideal_L)/$ideal_seg}]

      for {set i 1} {$i < $ideal_seg} {incr i} {
        set x_2 [expr {$seg_diff*sin($theta_x)+$x_1}]
        set y_2 [expr {$seg_diff*sin($theta_y)+$y_1}]
        set z_2 [expr {$seg_diff*sin($theta_z)+$z_1}]

        if {$debug == 1} {puts "$x_1, $y_1, $z_1 | $x_2, $y_2, $z_2"...
           }
        CreateLinexyz $dir/b$i.crv $x_1 $y_1 $z_1 $x_2 $y_2 $z_2
        lappend grids $dir/b$i.crv

        set x_1 $x_2
        set y_1 $y_2
        set z_1 $z_2
      }

      #puts "i: $i"
      if {$debug == 1} {puts "$x_1, $y_1, $z_1 | $x2, $y2, $z2"}
      CreateLinexyz $dir/b$i.crv $x_1 $y_1 $z_1 $x2 $y2 $z2
      lappend grids $dir/b$i.crv

    }
    # make the constant spacing portion b

    ConcatGridsn $grids $ofile j 1

    exec rm -rf $dir
  }


  # ------------------------------------------------------------------...
     FindGF
# uses:    FindL
```

```
  # used by: FindNPGF
  proc FindGF {iws fws np L} {

  # set to 1 if i want to print all messages
    set debug 0

    set tol 0.00000000000001
    set gf1 0.
    set gf2 1.5

    set l1 [expr {[FindL $iws $gf1 $np] - $L}]
    set l2 [expr {[FindL $iws $gf2 $np] - $L}]

    if {$debug == 1} {puts "l1: $l1 l2: $l2"}

    while { $l2 < 0 } {
      set gf2 [expr {$gf2*2.}]
      set l2 [expr {[FindL $iws $gf2 $np] - $L}]
      if {$debug == 1} {puts "changing gf2: $gf2 and l2: $l2"}
    }

    if {$debug == 1} {puts ""}

    set count 0.

    set gf1_orig $gf1
    set gf2_orig $gf2

    while { abs($gf1 - $gf2) >= $tol} {

      set l1 [expr {[FindL $iws $gf1 $np] - $L}]
      set l2 [expr {[FindL $iws $gf2 $np] - $L}]

      set gf [expr {($gf2-$gf1)/2.+$gf1}]

      # L
      set l [expr {[FindL $iws $gf $np] - $L}]

      if {$debug == 1} {puts "$l1 $l2 | $gf1 $gf2 | $l $gf"}

      if {$l < 0.} {
        set gf1 $gf
      } elseif {$l > 0.} {
        set gf2 $gf
      } else {
        return $gf
      }

      set count [expr {$count + 1.}]
      if {$count == 70} {
        set gf1 $gf1_orig
        set gf2 $gf2_orig
```

```
        set tol [expr {$tol*10.}]
        set count 0.
283     if {$debug == 1} {puts "resetting tolerance"}
      }

    }

288 if {$debug == 1} {puts ""
    puts "gf: $gf"
    puts [FindL $iws $gf $np]}

    return $gf
293 }


  # ------------------------------------------------------------------...
      FindL
  # private function
298 # uses:    none
  # used by: FindGF
  proc FindL {iws gf np} {
    set sum 0.
    for {set i 1} {$i < $np} {incr i} {
303   set sum [expr {$sum + pow($gf,double($i)-1.)}]
    }
    set fws [expr {pow($gf,double($i)-1.)*$iws}]
    return [expr {$sum*$iws}]
  }
308
  # ------------------------------------------------------------------...
      FindNPGF
  # private function
  # uses:    FindGF
  # used by: MakeGeomCurve
313 proc FindNPGF {iws fws L gf_guess} {
    # given L, fws, iws, solve for np and gf closest to gf_guess
    # increase np until sign changes. pick the closest values

    # set to 1 if i want to print all messages
318 set debug 0

    if {$debug == 1} {puts "iws: $iws fws: $fws L: $L gf_guess: ...
       $gf_guess\n"}

    set gf [expr {$gf_guess + 1.}]
323 set gf2 $gf
    set np 3

    while {($gf-$gf_guess) > 0.} {
      set gf1 $gf2
328
```

```
      set gf2 [FindGF $iws $fws $np $L]
      set gf $gf2

333   set np [expr {$np+1}]
      #puts "gf1: $gf1 gf2: $gf2"
      if {$debug == 1} {puts "function: [expr {($gf-$gf_guess)}] np:...
          $np gf: $gf2\n"}

    }
338

    # compare gf2 and gf1, choose gf closest to gf_guess
    if {abs($gf1-$gf_guess) > abs($gf2-$gf_guess)} {
      #return $gf2
343   if {$debug == 1} {puts "gf: $gf2"}
      set gf $gf2
      set np [expr {$np-1}]
    } else {
      #return $gf1
348   if {$debug == 1} {puts "gf: $gf1"}
      set gf $gf1
      set np [expr {$np-2}]
    }

353 if {$debug == 1} {puts "final length: [FindL $iws $gf $np] np: ...
      $np"}

    return [list $np $gf]

  }
358
  # ============================================================ ...
     global functions

  # not as robust, prone to errors, but good for rough estimates
  # inputs iws, fws, and gf
363 # outputs length

  proc FindLEN1 {iws fws gf} {

    set np [expr {int(round((log($fws)-log($iws)) / log($gf)+1.)) + ...
       1}]
368 set sum 0.
    for {set i 0} {$i < $np-1} {incr i} {set sum [expr {$sum + ...
       $gf**double($i)}]
      #puts $sum
    }

373 return [expr {$sum * $iws}]
  }

  # input iws, gf, and number of points
```

```
   # outputs fws, the next spacing past fws, and total length of ...
      given np
378
   proc FindLEN2 {iws gf np} {
     set sum 0.
     for {set i 1} {$i < $np} {incr i} {
       set sum [expr {$sum + pow($gf,double($i)-1.)}]
383
     }
     set fws1 [expr {pow($gf,double($i)-2.)*$iws}]
     set fws2 [expr {pow($gf,double($i)-1.)*$iws}]
     set return_args [list $fws1 $fws2 [expr {$sum*$iws}]]
388 }

   proc MakeUnifCurve {spacing x1 y1 z1 x2 y2 z2 ofile} {

     set dir Unif_Curve
393  exec mkdir -p $dir

     set distance [Dist $x1 $y1 $z1 $x2 $y2 $z2]
     set np [expr {round($distance/$spacing)+1}]

398  CreateLinexyz $dir/temp.crv $x1 $y1 $z1 $x2 $y2 $z2
     SrapRedist $dir/temp.crv $ofile 0 j 1 1 0 [list 1 -1 $np ...
        $spacing $spacing]


     exec rm -rf $dir
403


   }

   #!/usr/bin/tclsh

 3 source module.tcl

   # ================================= Initialize parameters.

   if { [info exists env(SCRIPTLIB)] } {
 8   lappend auto_path $env(SCRIPTLIB)
   } else {
     puts stderr "\n ERROR: use 'setenv SCRIPTLIB' to define the ...
        location of"
     puts stderr "        the Tcl library routines from Chimera Grid...
         Tools.\n"
     exit 1
13 }

   if { [info exists env(CGTBINDIR)] } {
     InitExecs
   } else {
18   puts stderr "\n ERROR: use 'setenv CGTBINDIR' to define the ...
        location of"
```

```
    puts stderr "        the Chimera Grid Tools executables.\n"
    exit 1
}

# ================================== constants
set pi 3.14159265359
set rad_deg [expr {$pi/180.}]

# ================================== backward compatability

set Grid(tunnel_with_step) yes

# ================================== hole
set Par(hole_iws) 0.00024
set Par(hole_fws) 0.05
set Par(hole_gf)  1.2

set Par(hole_center_x) 0.
set Par(hole_center_y) 0.
set Par(hole_center_z) 0.

set Par(hole_inner_radius) 0.118
set Par(hole_depth) 0.572

#set Par(hole_inclination) 90.
#set Par(hyptan_gf) 1.15

# ================================== tunnel
# x,y minimums

# grid planes must lie in the xz plane oriented to use jk planes

# 1 for exists, 0 for not exists
set Par(hole_exists) 0

# downstream/upstream from the hole
set Par(tunnel_upstream_length) 10tunnel_downstream_length)}]
set Par(tunnel_height) 8
set Par(tunnel_width) 0.625

set Par(tunnel_x1) [expr {$Par(hole_center_x) - $Par(...
    tunnel_upstream_length)}]
set Par(tunnel_z1) 0

# growth factor
set Par(tunnel_gf) 1.2

# initial and final wall spacing (y-direction)
set Par(tunnel_iws) $Par(hole_iws)

# coarse  0.1
# medium  0.05
```

```
   # fine    0.025
   set Par(tunnel_fws) 0.05

73 # (x-direction)
   # number of cells to pad, higher increases spacing accuracy but ...
      decreases exec speed
   set Par(tunnel_horizontal_buffer) 0

   # the coarse spacing resolution
78 set Par(tunnel_spacing) .125
   set Par(concat_tol) 0.0

   # overlap the internal tunnel grids by this much
   set Par(tunnel_overlap) 5
83
   # ---------- calculations

   set len1 [FindLEN1 $Par(tunnel_iws) $Par(tunnel_spacing) $Par(...
      tunnel_gf)]
   set len2 [expr {$Par(tunnel_overlap) * $Par(tunnel_spacing)}]
88 set len3 [FindLEN1 $Par(tunnel_iws) $Par(tunnel_fws) $Par(...
      tunnel_gf)]


   # ================================== backward facing step

93 # distance from hole center to backward facing step
   set Par(step_downstream_distance) 3.
   set Par(step_height) 1.
   set Par(step_length) 3.

98 set Par(shock_location) [expr {$Par(hole_center_x) + $Par(...
      step_height)*12}]

   # ================================== refinement

   # x1, x2, y1, y2, z1, z2
103 # x, y, z, length, width, height
   # x, y, z must be in negative position, length, width, height is ...
      positive coordinate axes

   set refine(quantity) 1

108 # - - - - - - - refinement region 1
   set x_loc [expr {$Par(hole_center_x) + $Par(...
      step_downstream_distance)}]
   set x [expr {$x_loc - $Par(step_height)*8}]
   set y [expr {-$Par(tunnel_width)/2.}]
   set z [expr {$Par(hole_center_z) + $Par(tunnel_fws)*2}]
113
   set xlen [expr {$Par(step_height)*4 - $Par(tunnel_fws)*2}]
   set ylen $Par(tunnel_width)
```

```
    set zlen [expr {$Par(step_height)*3 - $Par(tunnel_fws)*2 + $Par(...
       tunnel_fws)*2 + $Par(tunnel_fws)*$Par(tunnel_overlap)}]
    #set zlen [expr {$Par(step_height) - $Par(tunnel_fws)*2 + $Par(...
       tunnel_fws)*2 + $Par(tunnel_fws)*3}]
118 #set zlen [expr {$Par(step_height) - $Par(tunnel_fws)*2 + $Par(...
       tunnel_fws)*2}]

    set refine(1) [list $x $y $z $xlen $ylen $zlen]

    # - - - - - - - - refinement region 2
123 set x_loc [expr {$Par(hole_center_x) + $Par(...
       step_downstream_distance)}]
    set x [expr {$x_loc - $Par(step_height)*8}]
    set y [expr {-$Par(tunnel_width)/2.}]
    set z [expr {$Par(hole_center_z) + $Par(step_height) + $Par(...
       tunnel_fws)*2}]

128 #set xlen [expr {$Par(step_height)*6 - $Par(tunnel_fws)*2}]
    #set xlen [expr {$Par(step_height)*6 - $Par(tunnel_fws)*2 + $Par(...
       tunnel_fws)*3}]
    set xlen [expr {$Par(step_height)*4 - $Par(tunnel_fws)*2 + $Par(...
       tunnel_fws)*$Par(tunnel_overlap)}]
    set ylen $Par(tunnel_width)
    set zlen [expr {$Par(step_height)*2}]
133
    set refine(2) [list $x $y $z $xlen $ylen $zlen]

    # - - - - - - - - refinement region 3
    set x_loc [expr {$Par(hole_center_x) + $Par(...
       step_downstream_distance)}]
138 set x [expr {$x_loc - $Par(tunnel_fws)*2}]
    set y [expr {-$Par(tunnel_width)/2.}]
    set z [expr {$Par(hole_center_z) + $Par(step_height) + $Par(...
       tunnel_fws)*2}]

    set xlen [expr {$Par(step_height)*3}]
143 set ylen $Par(tunnel_width)
    set zlen [expr {$Par(step_height)*2}]

    set refine(3) [list $x $y $z $xlen $ylen $zlen]

148 # ================================== boundary conditions

    set bound(tunnel_wall)  5
    set bound(tunnel_left)  32
    set bound(tunnel_top)   32
153 set bound(tunnel_right) 32
    set bound(tunnel_sides) 18
    set bound(point_matching) 20

    # ================================== clean up
158
```

```
exec mkdir -p $Par(crvdir)
exec mkdir -p $Par(srfdir)
exec mkdir -p $Par(voldir)
exec mkdir -p $Par(xdir)

#!/usr/bin/tclsh

#source module.tcl
source params.tcl

# ...
    ================================================================================...
     begin main

# setup
set root_name tunnel_1
set tmpdir [Get_Temp]

# Grid system
#
#  left edge of tunnel
#     midway between left edge and center
#        center of hole
#   - - - - - - - - - - -+ -+- - - - - - -
#  |  !  !                    !  !           4 !
#  |  !  !                    !  !             !
#  |  !  !                    !  !             !
#  |  !  !                    !- !- -+- - - - -!
#  |  !  !                    !- !- -+- - - - -!
#  |  !  !                    !_ !_ _!_______3_!
#  |  !  !                    !  !   |
#  |  !  !                    !  !   |
#  |  !  !             1      !  !  2|
#  |__!__!____________________!__!___|

# coordinate system:
#
#   z  y
#   |/_x

# tunnel 1
#
#    3 left side
#    |
#    9 top of step
#    |
#    |    front side
#    |   4 - - - - - - - - - - - o
#    |  /                       /
#    | 3 hole center           /
#    |/                       /
#    1 - - 5 - - 6 - - 7 - - 8 start of step
```

```
#          padding
#                hole center       bottom side
#                      padding
#
#

# ...
    ================================================================================...
     left side

set x [expr {$Par(hole_center_x) - $Par(tunnel_upstream_length)}]
set y [expr {$Par(hole_center_y) - $Par(tunnel_width)/2.}]
set z $Par(hole_center_z)

# segment 1-9
set z1 $Par(hole_center_z)
set z2 [expr {$Par(hole_center_z) + $Par(step_height)}]
MakeGeomCurve $Par(tunnel_iws) $Par(tunnel_spacing) $Par(tunnel_gf...
   ) $x $y $z1 $x $y $z2 $Par(crvdir)/tunnel_1_19.crv

# segment 9-3
set z1 $z2
set z2 [expr {$Par(hole_center_z) + $Par(tunnel_height)}]
MakeUnifCurve $Par(tunnel_spacing) $x $y $z1 $x $y $z2 $Par(crvdir...
   )/tunnel_1_93.crv

set grids [list $Par(crvdir)/tunnel_1_19.crv $Par(crvdir)/...
   tunnel_1_93.crv]
AutoConcatGrids $grids $Par(crvdir)/tunnel_1_left.crv 1 0.

foreach a $grids { exec rm $a }

# ...
    ================================================================================...
     bottom side

set np [expr {floor($Par(tunnel_upstream_length)/$Par(...
   tunnel_spacing)) - round($Par(tunnel_horizontal_buffer))}]
set len [expr {$np * $Par(tunnel_spacing)}]

# segment 6-5
set x2 $x
set x1 $Par(hole_center_x)
MakeUnifCurve $Par(tunnel_spacing) $x1 $y $z $x2 $y $z $Par(crvdir...
   )/tunnel_1_65.crv

set grids [list $Par(crvdir)/tunnel_1_65.crv $Par(crvdir)/...
   tunnel_1_68.crv]

AutoConcatGrids $grids $Par(crvdir)/tunnel_1_bot.crv 1 0.

foreach a $grids { exec rm $a }
```

```
# ...
    ========================================================================...
     generate surface

# combine curves
set grids [list $Par(crvdir)/tunnel_1_bot.crv $Par(crvdir)/...
    tunnel_1_left.crv]
CombineGrids $grids $Par(crvdir)/tunnel_1_botleft.crv

# generate surface
GenTFIGrids [list $Par(crvdir)/tunnel_1_botleft.crv] $Par(srfdir)/...
    tunnel_1.bak [list 1 2]

P3Ds2m $Par(srfdir)/tunnel_1.bak $Par(srfdir)/tunnel_1.srf
exec rm $Par(srfdir)/tunnel_1.bak $Par(crvdir)/...
    tunnel_1_botleft.crv

# ...
    ========================================================================...
     generate volume

ExtrudeSurface $Par(srfdir)/tunnel_1.srf $Par(voldir)/$root_name.m...
     $Par(crvdir)/tunnel_front_spacing.crv

ReverseInd $Par(voldir)/$root_name.m $Par(xdir)/$root_name.x revj
SwapInd $Par(xdir)/$root_name.x $Par(voldir)/$root_name.m swapkl
P3Dm2s $Par(voldir)/$root_name.m $Par(xdir)/$root_name.x

# ...
    ========================================================================...
     generate input file

set dim [GetDim $Par(xdir)/$root_name.x]

# must be same name as .x file
set id [open $Par(inpdir)/$root_name.txt w]

set z [expr {$Par(hole_center_z) + $Par(step_height)}]

set ind [GetJkl $Par(xdir)/$root_name.x $x $y $z 1]

set a $bound(tunnel_wall)
set b $bound(tunnel_left)
set c $bound(tunnel_top)
set d $bound(tunnel_right)
set e $bound(tunnel_sides)
set f [lindex $ind 2]
#set g $bound(point_matching)

puts $id "PHANTOM = .FALSE."
puts $id [format "IBTYP = %3i, %3i, %3i, %3i, %3i, %3i," $b  $e  ...
```

```
    $e  $a  $c  $a ]
puts $id [format "IBDIR = %3i, %3i, %3i, %3i, %3i, %3i,"  1   2  ...
    -2   3  -3  -1 ]
puts $id [format "JBCS  = %3i, %3i, %3i, %3i, %3i, %3i,"  1   1   ...
    1   1   1  -1 ]
puts $id [format "JBCE  = %3i, %3i, %3i, %3i, %3i, %3i,"  1  -1  ...
    -1  -1  -1  -1 ]
puts $id [format "KBCS  = %3i, %3i, %3i, %3i, %3i, %3i,"  1   1  ...
    -1   1   1   1 ]
puts $id [format "KBCE  = %3i, %3i, %3i, %3i, %3i, %3i," -1   1  ...
    -1  -1  -1  -1 ]
puts $id [format "LBCS  = %3i, %3i, %3i, %3i, %3i, %3i,"  1   1   ...
    1   1  -1   1 ]
puts $id [format "LBCE  = %3i, %3i, %3i, %3i, %3i, %3i," -1  -1  ...
    -1   1  -1  $f ]
puts $id "NP = [lindex $dim 4]"

close $id

# ...
    ================================================================================...
     clean-up

exec rm -rf $tmpdir
```

1.3 Fortran Code

```
program slice_read

! Convert a 32-bit qslice file to ASCII file

implicit none
character(128) :: xfile, ofile, qfile, ifile

! grid variables
real*4, dimension(:,:,:), allocatable :: x, y, z, iblank
!integer, dimension(:), allocatable:: nj, nk, nl
integer :: nj, nk, nl

! q variables
real*4, dimension(:,:,:,:), allocatable :: q
real*4, dimension(:), allocatable :: rgas
real*4 :: refmach, alpha, rey, time, gaminf, beta, tinf, igam, ...
    htinf, ht1, ht2
real*4 :: fsmach, tvref, dtvref, gaminf_m_1
integer, dimension(:), allocatable:: qnj, qnk, qnl

! real*8, dimension(:,:,:,:), allocatable :: qdp
!integer, dimension(:,:,:), allocatable :: iblank
!integer :: igrid, istep, nj, nk, nl, nq, nqc
integer :: nq, nqc
integer :: ngrid, ig
```

```
   logical :: flag
28 real*4 :: tol
   integer :: xvar, zvar, num_qfiles
   real*4, dimension(:), allocatable :: xval, zval
   !real*8 :: tvref, dtvref

33 !real*4, dimension(:,:,:), allocatable :: xsp, ysp, zsp
   !real*4, dimension(:,:,:,:), allocatable :: qsp
   !real*4 :: tvrefsp, dtvrefsp

   integer :: i,j,k,l,m,n
38
   !integer, allocatable :: istep, nj, nk, nl
   !logical :: single_grid, overflow, more

   ! ================================================================
43
   print*, ''
   print*, ' *** Program: SLICE_READ ***'
   print*, ' *** Filter and convert 32-bit split-m outputs ASCII file...
       *** '
   print*, ''
48
   !ifile = 'slice_read.inp'
   !xfile = 'xslice.in'
   !qfile = 'viz/qslice.100000'

53 tol = 0.001
   ofile = 'data_f.txt'

   !print*, ' Using input file: ', ifile
   !print*, ' Reading in file: ', xfile
58
   read(*,*) xvar
   allocate( xval(xvar) )
   do i = 1,xvar
     read(*,*) xval(i)
63 enddo

   read(*,*) zvar
   allocate( zval(zvar) )
   do i = 1,zvar
68   read(*,*) zval(i)
   enddo


   read(*,*) xfile
73 print*, ' Using grid file: ', xfile
   open(1, file=xfile, status='old', form='unformatted', action='read...
      ')
```

```
   ! assume ngrid is 1, more than that and can't handle
   read(1) ngrid
   !allocate( nj(ngrid), nk(ngrid), nl(ngrid) )
78 read(1) nj, nk, nl
   print*, nj
   allocate( x(nj,nk,nl), y(nj,nk,nl), z(nj,nk,nl), iblank(nj,nk,nl) ...
      )
   read(1) x, y, z, iblank
   close(1)
83
   nqc = 7
   allocate( qnj(ngrid), qnk(ngrid), qnl(ngrid), rgas(max(2,nqc)) )
   allocate( q(nj,nk,nl,nq) )

88 read(*,*) num_qfiles
   print*, ''
   print*, ' Number of grids: ', ngrid
   print*, ' Number of q files: ', num_qfiles
   print*, ''
93
   !print*, xnj, xnk, xnl

   ig = 1
   gaminf_m_1 = gaminf - 1.0
98
   open(10, file=ofile, status='old', form='formatted', action='write...
      ')

   do m=1,2
     read(*,*) qfile
103  print*, ' Reading q file: ', qfile
     open(2, file=qfile, status='old', form='unformatted', action='...
        read')

     ! read in the q file and allocate q variables
     read(2) ngrid
108  read(2) (qnj(ig),qnk(ig),qnl(ig),ig=1,ngrid), nq, nqc

     read(2) refmach, alpha, rey, time, gaminf, beta, tinf, igam, ...
        htinf, ht1, ht2, (rgas(i),i=1,max(2,nqc)), fsmach, tvref, ...
        dtvref
     read(2) q

113  !flag = .True.
     !print*, nj
     do j = 1,nj
       do k = 1,nk
         do l = 1,nl
118
           flag = .True.
           do n = 1,xvar
             !print*, abs(x(j,k,l) - xval(n))
```

```
            if (abs(x(j,k,l) - xval(n)) > tol) then
              flag = .False.
            end if
          enddo

          do n = 1,zvar
            write(10,*) abs(z(j,k,l) - zval(n))
            !print*, abs(z(j,k,l) - zval(n))
            if (abs(z(j,k,l) - zval(n)) > tol) then
              flag = .False.
            end if
          enddo

          if (flag) then
            print*, x(j,k,l), z(j,k,l), gaminf_m_1*q(j,k,l,5)
          end if

        enddo
      enddo
    enddo

!   print*, ''
    print*, '  ref mach: ',refmach
!   print*, 'alpha: ', alpha
!   print*, 'beta: ', beta
    !print*, '  nqc: ', nq
    print*, '  time: ', time
    print*, ''

    !deallocate( x, y, z, iblank )

    close(2)

  enddo

  close(10)

  deallocate( x )
  deallocate( q )
  deallocate( qnj, qnk, qnl )
  !deallocate( nj, nk, nl, qnj, qnk, qnl )



  end
```

Bibliography

1. K. W. Abrahamson and D. L. Brower. An Empirical Boundary Condition for Numerical Simulation of Porous Plate Bleed Flows. In *26th Aerospace Sciences Meeting*, San Diego, CA, 1988.

2. Steven R. Allmaras, Forrester T. Johnson, and Philippe R. Spalart. Modifications and Clarifications for the Implementation of the Spalart-Allmaras Turbulence Model. In *7th International Conference on Computational Fluid Dynamics*, number ICCFD7-1902, pages 1–11, 2012.

3. B. S. Baldwin and Harvard Lomax. Thin Layer Approximation and Algebraic Model for Separated Turbulent Flows. In *16th AIAA Aerospace Sciences Meeting*, 1978.

4. John J. Bertin and Russell M. Cummings. *Aerodynamics for Engineers*. Pearson, 6th edition, 2013.

5. Jiri Blazek. *Computational Fluid Dynamics: Principles and Applications*. Butterworth Heinemann, Oxford, 3rd edition, 2005.

6. J. P. Bodner, I. Greber, David O. Davis, and W. R. Hingst. Experimental Investigation of a Single Bleed Hole on a Supersonic Turbulent Boundary-Layer. In *32nd Joint Propulsion Conference and Exhibit*, 1996.

7. Pieter G. Buning. CFD Approaches for Simulation of Wing-Body Stage Separation. In *22nd AIAA Applied Aerodynamics Conference and Exhibit*, 2004.

8. William M. Chan. The OVERGRID Interface for Computational Simulations on Overset Grids. In *32nd AIAA Fluid Dynamics Conference and Exhibit*, 2002.

9. William M. Chan, Stuart E. Rogers, Shishir A. Pandya, David L. Kao, Pieter G. Buning, Robert L. Meakin, David A. Boger, and Steven M. Nash. Chimera Grid Tools User's Manual, 2010.

10. W. J. Chyu, G. W. Howe, and T. I-P Shih. Bleed Boundary Conditions for Numerically Simulated Mixed-Compression Supersonic Inlet Flow. *Journal of Propulsion and Power*, 8(4):862–868, 1992.

11. David O. Davis and Mark Schoenenberger. Bleed Hole Flow Phenomena Studied. *Mechanical Engineering*, pages 15–17, 1997.

12. David O. Davis, Manan A. Vyas, and John W. Slater. Research on Supersonic Inlet Bleed. In *50th AIAA Aerospace Sciences Meeting including the New Horizons Forum and Aerospace Exposition*, Nashville, Tennessee, January 2012. American Institute of Aeronautics and Astronautics.

13. David S. Dolling. Fifty Years of Shock-Wave/Boundary-Layer Interaction Research: What Next? *AIAA Journal*, 39(8):1517–1531, 2001.

14. Andrew Dorgan. Private Communications with Dr. John Slater, 2011.

15. Datta V. Gaitonde. Progress in Shock Wave/Boundary Layer Interactions. *43rd AIAA Fluid Dynamics Conference*, 2013.

16. Michael S. Holden. A Review of Aerothermal Problems Associated with Hypersonic Flight. In *24th AIAA Aerospace Sciences Meeting*, 1986.

17. D. D. Knight and G. Degrez. Shock Wave Boundary Layer Interactions in High Mach Number Flows: A Critical Survey of Current Numerical Prediction Capabilities. *AGARD Advisory Report*, 2:1.1–1.35, 1998.

18. David W. Mayer and Gerald C. Paynter. Boundary Conditions for Unsteady Supersonic Inlet Analyses. *AIAA Journal*, 32(6):1200–1206, 1994.

19. G. McLafferty and E. Ranard. Pressure Losses and Flow Coefficients of Slanted Perforations Discharging from Within a Simulated Supersonic Inlet. Technical report, United Aircraft Corp., East Hartford, Conn., 1958.

20. NASA. NASA SBIR 2008 Phase 1 Solicitation, 2008.

21. NASA. NASA SBIR 2014 Phase I Solicitation, 2015.

22. Gerald C. Paynter, David W. Mayer, and Elling Tjonneland. Flow Stability Issues in Supersonic Inlet Flow Analyses. In *31st Aerospace Sciences Meeting*, Reno, Nevada, 1993.

23. S. Piponniau, Jean-Paul Dussauge, Jean-François Debiève, and Pierre Dupont. A Simple Model for Low-Frequency Unsteadiness in Shock-Induced Separation. *Journal of Fluid Mechanics*, 629:87, 2009.

24. T. H. Pulliam and D. S. Chaussee. A Diagonalized Form of an Implicit Approximate Factorization Algorithm. *Journal of Computational Physics*, 39, 1981.

25. O. Reynolds. On the Sub-Mechanics of the Universe: Papers on Mechanical and Physical Subjects. *Cambridge University Press*, 3, 1903.

26. Stuart E. Rogers, Norman E. Suhs, William E. Dietz, Steven M. Nash, and Jeffrey T. Onufer. PEGASUS User's Guide, 2016.

27. John D. Schmisseur. Hypersonics Into the 21st Century: A Perspective on AFOSR-Sponsored Research in Aerothermodynamics. In *43rd AIAA Fluid Dynamics Conference*, 2013.

28. R. J. Shaw, J. C. Dutton, and A. L. Addy. Time-Series Analyses of Wall Pressure Fluctuations in Plume-Induced Separated Flowfields. *AIAA Journal*, 36(10), 1998.

29. Robert J. Shaw, Joseph F. Wasserbauer, and Harvey E. Neumann. Boundary-Layer Bleed System Study for a Full-Scale, Mixed-Compression Inlet with 45 Percent Internal Contraction. Technical report, NASA TM X-3358, 1976.

30. John W. Slater. Improvements in Modeling 90-degree Bleed Holes for Supersonic Inlets. In *47th AIAA Aerospace Sciences Meeting including The New Horizons Forum and Aerospace Exposition*, Reston, Virigina, January 2009. American Institute of Aeronautics and Astronautics.

31. John W. Slater. Improvements in Modeling 90-degree Bleed Holes for Supersonic Inlets. *Journal of Propulsion and Power*, 28(4):773–781, July 2012.

32. Philippe R. Spalart. Trends in Turbulence Treatments. In *AIAA Fluids*, Denver, 2000.

33. Philippe R. Spalart and Steven R. Allmaras. A One-Equation Turbulence Model for Aerodynamic Flows. In *30th AIAA Aerospace Sciences Meeting and Exhibit*, 1992.

34. Philippe R. Spalart, S. Deck, M. L. Shur, K. D. Squires, M. K. Strelets, and A. Travin. A New Version of Detached Eddy Simulation, Resistant to Ambiguous Grid Densities. *Theoretical and Computational Fluid Dynamics*, 20:181–295, 2006.

35. Philippe R. Spalart, W-H. Jou, M. K. Strelets, and Steven R. Allmaras. Comments on the Feasibility of LES for Wings and on a Hybrid RANS/LES Approach. In *1st AFOSR International Conference on DNS/LES*, 1997.

36. J Syberg and T. E. Hickcox. Design of a Bleed System for a Mach 3.5 Inlet. Technical report, 1973.

37. John C. Tannehill, Dale A. Anderson, and Richard H. Pletcher. *Computational Fluid mechanics and Heat Transfer*. CRC Press/Taylor & Francis Group, Boca Raton, 3rd edition, 1997.

38. Jiyuan Tu, Guan Heng Yeoh, and Chaoqun Liu. *Computational Fluid Dynamics: A Practical Approach*. Butterworth-Heinemann, 2nd edition, 2012.

39. Frank M. White. *Fluid Mechanics*. McGraw-Hill Education, 4th edition, 1998.

40. B. P. Willis and David O. Davis. Boundary Layer Development Downstream of a Bleed Mass Flow Removal Region. In *32nd Joint Propulsion Conference and Exhibit*, Reston, Virigina, July 1996. American Institute of Aeronautics and Astronautics.

41. B. P. Willis, David O. Davis, and W. R. Hingst. Flow Coefficient Behavior for Boundary Layer Bleed Holes and Slots. In *33rd Aerospace Sciences Meeting and Exhibit*, Reno, Nevada, January 1995. American Institute of Aeronautics and Astronautics.

42. G.-C. Zha, D. D. Knight, Donald Smith, and Martin Haas. Numerical Simulation of High Speed Civil Transport Inlet Operability with Angle of Attack. *AIAA Journal*, 36(7):1223–1229, 1998.

Vita

First Lieutenant Dayle L. Chang graduated from Bellaire High School in Houston, Texas and attended the University of Texas at Austin. In December 2013, he graduated with a Bachelor of Science degree in Aerospace Engineering and commissioned through AFROTC Detachment 825.

His first assignment came in May 2014 as an aerospace research engineer in the Design and Analysis Branch, Aerospace Systems Directorate, Air Force Research Laboratory at Wright-Patterson AFB. In June 2016, he was assigned to the Aerodynamic Validation Branch where he served as a project engineer conducting wind tunnel testing. Through both assignments, he was enrolled as a part-time student at the Graduate School of Engineering and Management, Air Force Institute of Technology.

Upon graduation, he will be assigned to the DoD Human Spaceflight Payloads office as a program office engineer under the Advanced Systems and Development Directorate, Space and Missiles Center at NASA Johnson Space Center in Houston, Texas.

REPORT DOCUMENTATION PAGE

Form Approved
OMB No. 0704-0188

1. REPORT DATE *(DD-MM-YYYY)*	2. REPORT TYPE	3. DATES COVERED *(From - To)*
28 Mar 2018	Master's Thesis	March 2015 - March 2018

4. TITLE AND SUBTITLE
Computational Investigation Using Bleed as a Method of Shock Stabilization

5a. CONTRACT NUMBER

5b. GRANT NUMBER

5c. PROGRAM ELEMENT NUMBER

6. AUTHOR(S)
Chang, Dayle L, 1LT

5d. PROJECT NUMBER

5e. TASK NUMBER

5f. WORK UNIT NUMBER

7. PERFORMING ORGANIZATION NAME(S) AND ADDRESS(ES)
Air Force Institute of Technology
Graduate School of Engineering and Management (AFIT/EN)
2950 Hobson Way
Wright-Patterson AFB OH 45433-7765

8. PERFORMING ORGANIZATION REPORT NUMBER
AFIT-ENY-MS-18-M-247

9. SPONSORING/MONITORING AGENCY NAME(S) AND ADDRESS(ES)
Air Force Research Laboratory
Dr. Michael Stanek, Technical Advisor
2145 5th Street, Bldg 24C
Wright-Patterson AFB, OH 45433
michael.stanek@us.af.mil / (937) 656-8767

10. SPONSOR/MONITOR'S ACRONYM(S)
AFRL/RQVI

11. SPONSOR/MONITOR'S REPORT NUMBER(S)

12. DISTRIBUTION/AVAILABILITY STATEMENT
Distribution Statement A. Approved for Public Release; Distribution Unlimited

13. SUPPLEMENTARY NOTES
This work is declared a work of the U.S. Government and is not subject to copyright protection in the United States.

14. ABSTRACT

Shock-wave/boundary layer interactions (SWBLI) produce undesirable dynamic loads and separated unsteady flows, adversely impacting the performance and structural integrity of supersonic vehicles. Computational fluid dynamics (CFD) is a successful tool in experimental planning and shows promise as a critical tool in understanding and mitigating negative effects of SWBLI. The goal of this research is to demonstrate the effect of bleed holes on shock stability using the OVERFLOW CFD solver to inform the planning of an Air Force Research Laboratory (AFRL) SWBLI wind tunnel experiment. First, a two-dimensional, flat plate, single-hole configuration was developed. Massflow discrepancies of 14.8% were initially observed but reduced to 0% by analyzing the internal flow interaction with the boundary condition. Shock unsteadiness is then characterized using a canonical forward-facing step over a flat plate, which showed peaks at 5.8, 12.1, 31.2, 44.5, and 54.9 hertz. Though the final step of simulating bleed on the baseline forward-facing step was not achieved, promising time and frequency domain analysis techniques were demonstrated.

15. SUBJECT TERMS
Shock-wave/boundary layer interaction, bleed holes, computational fluid dynamics, shock stabilization

16. SECURITY CLASSIFICATION OF:			17. LIMITATION OF ABSTRACT	18. NUMBER OF PAGES	19a. NAME OF RESPONSIBLE PERSON
a. REPORT	b. ABSTRACT	c. THIS PAGE			Maj Darrell S. Crowe, AFIT/ENY
U	U	U	UU	133	19b. TELEPHONE NUMBER *(Include area code)* (937) 255-3636 x4204 darrell.crowe@afit.edu